LASER COOLING AND SYMPATHETIC COOLING IN A LINEAR QUADRUPOLE RF TRAP

A Dissertation

by

VLADIMIR LEONIDOVICH RYJKOV

Submitted to the Office of Graduate Studies of
Texas A&M University
in partial fulfillment of the requirements for the degree of

DOCTOR OF PHILOSOPHY

December 2003

Major Subject: Physics

LASER COOLING AND SYMPATHETIC COOLING

IN A LINEAR QUADRUPOLE RF TRAP

A Dissertation

by

VLADIMIR LEONIDOVICH RYJKOV

Submitted to Texas A&M University
in partial fulfillment of the requirements
for the degree of

DOCTOR OF PHILOSOPHY

Approved as to style and content by:

Hans A. Schuessler (Chair of Committee)	
David A. Church (Member)	George W. Kattawar (Member)
Philip R. Hemmer (Member)	Edward S. Fry (Head of Department)

December 2003

Major Subject: Physics

ABSTRACT

Laser Cooling and Sympathetic Cooling

in a Linear Quadrupole RF Trap. (December 2003)

Vladimir Leonidovich Ryjkov, B.S. in Physics, Moscow State University

Chair of Advisory Committee: Dr. Hans A. Schuessler

An investigation of the sympathetic cooling method for the studies of large ultra-cold molecular ions in a quadrupole ion trap has been conducted.

Molecular dynamics simulations are performed to study the rf heating mechanisms in the ion trap. The dependence of rf heating rates on the ion temperature, trapping parameters, and the number of ions is obtained. New rf heating mechanism affecting ultra-cold ion clouds exposed to laser radiation is described.

The saturation spectroscopy setup of the hyperfine spectra of the molecular iodine has been built to provide an accurate frequency reference for the laser wavelength. This reference is used to obtain the fluorescence lineshapes of the laser cooled Mg^+ ions under different trapping conditions. The ion temperatures are deduced from the measurements, and the influence of the rf heating rates on the fluorescence lineshapes is also discussed.

Cooling of the heavy ($m = 720$a.u.) fullerene ions to under 10K by the means of the sympathetic cooling by the Mg^+ ions($m = 24$a.u.) is demonstrated.

The single-photon imaging system has been developed and used to obtain the images of the Mg^+ ion crystal structures at mK temperatures.

To my wife, Xianzhen Zhao and my daughter Yekaterina Ling-Shan Ryjkova.

ACKNOWLEDGMENTS

I would like to thank my advisor and the committee chair, Dr. Hans A. Schuessler, for his guidance throughout all of the stages of the research. The members of my Ph.D. committee, Dr. David A. Church, Dr. Philip R. Hemmer, and Dr. George W. Kattawar have my thanks for all their time and help.

The Department of Physics, Texas A&M University also has my thanks for the financial assistantship in the past few years. I also acknowledge Welch foundation and Texas Higher Education Board for the financial support at different stages of this project.

Most importantly, I would like to thank Xianzhen Zhao, my wife. She has not only been a wonderful supportive spouse, but a great colleague. Together we have developed most of the experimental setup, and she continued to participate in the research after the graduation whenever time allowed. Her input and the help with this dissertation were invaluable.

I would also like to express my appreciation to all of the wonderful people who have worked in this lab over the years. Daniel Buzatu, Jens Lassen, Vladimir Lioubimov, Sergei Jerebtsov, Dr. Alexander Kolomenski, Dr. Mihai Dinca, Dr. Xinghua Li, it has been a pleasure to share the lab with you.

Many thanks to people working or having worked in the machine shop and the electronic shop for the work they have done for this research as well as the valuable advice.

Chris Jaska from Spectra Physics has my special thanks. Not only I was able to learn a fair bit about the lasers from him, his help was crucial and his assistance forthcoming whenever he was called.

TABLE OF CONTENTS

CHAPTER Page

LIST OF TABLES

LIST OF FIGURES

FIGURE Page

FIGURE Page

CHAPTER I

INTRODUCTION

Since the invention of the radiofrequency(rf) ion trap [1, 2, 3] it has evolved into a very important tool in fundamental and applied research[4, 5]. The storage ring[6] and linear[7] trap configurations were added to the original hyperbolic geometry, and the size has been reduced to a tiny size designed to trap just one ion[8]. Nevertheless the most important feature of an ion trap remains the same: the ability to isolate and store charged particles such as ions. In an rf trap the ions are driven together by an alternating rf field, yet at the same time the forces of Coulomb repulsion keep them apart. As a result, a sparse cloud of ions is floating in vacuum isolated from the environment and each other. This arrangement makes the ion trap an excellent device for studies of isolated charged particles.

An important step in the ion trap research was the use of laser cooling. An atomic ion, when exposed to laser radiation of properly chosen frequency, will lose its kinetic energy. Consequently, a cloud of atomic ions stored in the trap, when subjected to such laser radiation, will cool down, with a possibility of its temperature reaching the millikelvin range. In this cool down process the ion cloud changes its structure from a gaseous chaotic cloud to an ordered ion crystal, also called Wigner crystal[9, 10].

While molecular ions can be stored in the trap just as easily as atomic ions, laser radiation is not directly usable for cooling them. This is due to the large number of internal degrees of freedom that a molecule has. However there exists a mechanism that allows for the cooling of molecular ions inside the trap. In this cooling method,

---

The journal used for style and format is Physical Review A.

called sympathetic cooling, different ion species are simultaneously stored in the ion trap and one of them is laser cooled. Through thermal contact with the laser cooled ions the rest of the ions will lose energy as well and cool down. This phenomenon of sympathetic cooling is gaining a lot of interest and has been observed with different atomic isotopes[11], ions of different atoms[12], and simple molecular ions[13].

In this dissertation I describe my investigations, both theoretical and experimental, into the application of the sympathetic laser cooling to very large molecules. The fullerene molecule C_{60} which has a mass of 720a.u. was used as a test in these studies.

The experimental apparatus has been developed. It was used in the first stage of this research[14]. It consists of the vacuum chamber with the quadrupole ion trap, the laser and optical system, and related electronics and the data acquisition systems. To achieve the goals set forth for this research the apparatus was modified. The sub-Doppler iodine saturation spectroscopy system was developed to obtain accurate frequency measurements and stabilization. The photon imager system was interfaced with a PC and the image acquisition software was written to obtain images of the cooled ions. Some electronics, as well as the experimental control and data acquisition software were redesigned. With this apparatus the studies of the laser cooling of the Mg^+ ions and the sympathetic cooling of the fullerene ions by Mg^+ ions were conducted.

On the theoretical side, an effort is made to advance the understanding of the cooling and heating mechanisms affecting ion clouds in linear quadrupole rf traps. The laser cooling and rf heating mechanisms are described theoretically. The connection is made to plasma thermodynamics. The framework for computer simulations of large ion clouds has been established. The simulations of the ion clouds were conducted to obtain insight into the rf heating and the sympathetic cooling mechanisms.

CHAPTER II

EXPERIMENTAL SETUP

The block diagram of the experimental apparatus is shown in Fig. 1. The apparatus consists of two major parts: the vacuum system containing the ion trap, and the laser and optical systems. The functioning of both groups is controlled and synchronized by a computer. This chapter gives an outline of the parameters and the operation of these systems. The initial apparatus was developed together with Xianzhen Zhao and a more detailed description of the design and experimental procedures is available in her dissertation[14]. The modifications made to the apparatus for the purposes of this research are described here and in the following chapters.

A. VACUUM SETUP AND THE ION TRAP

The purpose of the vacuum setup is to load and store various types of ions in the quadrupole rf ion trap. The center of this part of the apparatus is the ion trap which is placed in the ultra-high vacuum chamber. The background pressure in the chamber during the experiments is around 2×10^{-10}mbar. During the loading of the trap, helium gas is admitted into the chamber to cool the ions. The buffer gas cooling improves loading efficiency of the ions and drastically reduces the thermal fragmentation of the molecular ions (fullerenes). The block diagram of the vacuum system is shown in Fig. 2.

1. Ion trap

The ion trap consists of four parallel cylindrical rods, which are split into three equal segments. This arrangement creates an electrode structure suitable for confining the ions in both radial and axial directions. The ion trap geometry is shown in Fig. 3.

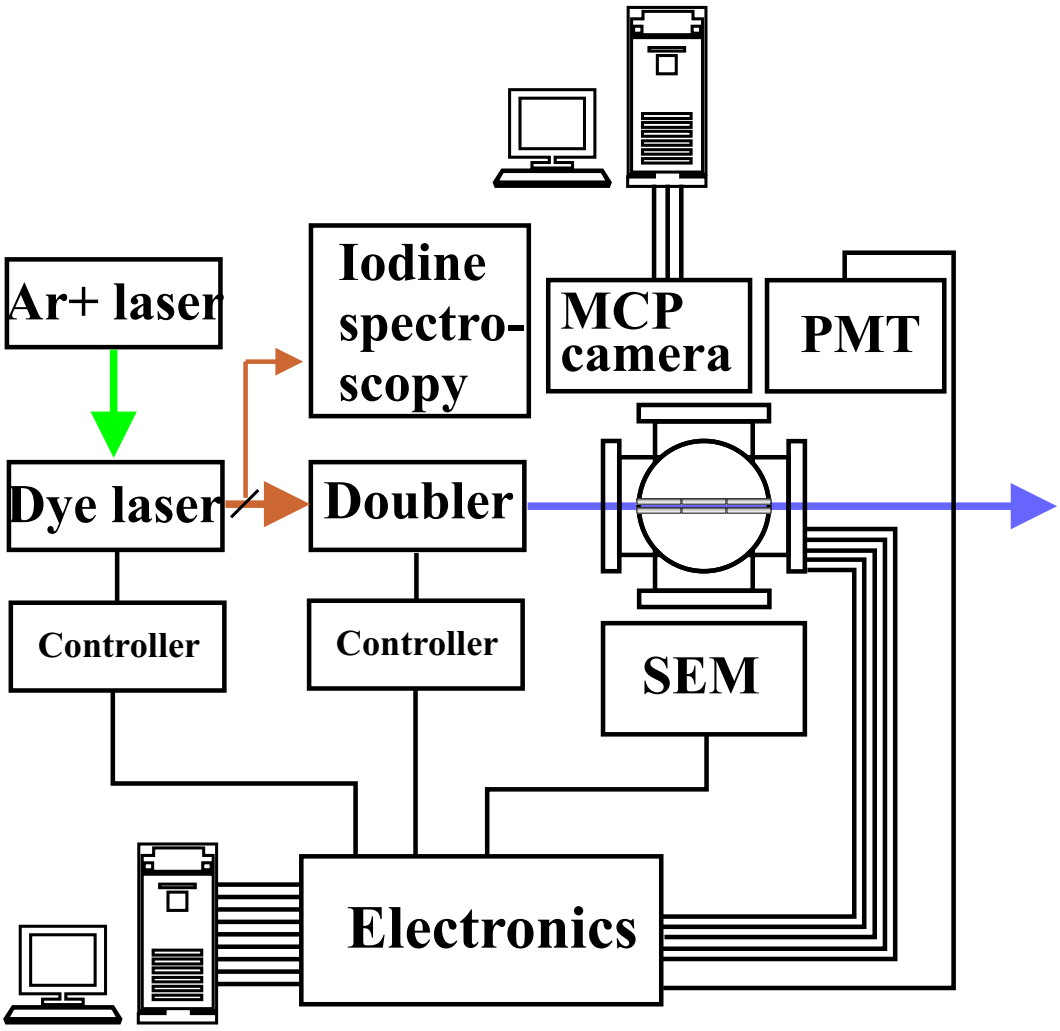

Fig. 1. Block diagram of the experimental setup.

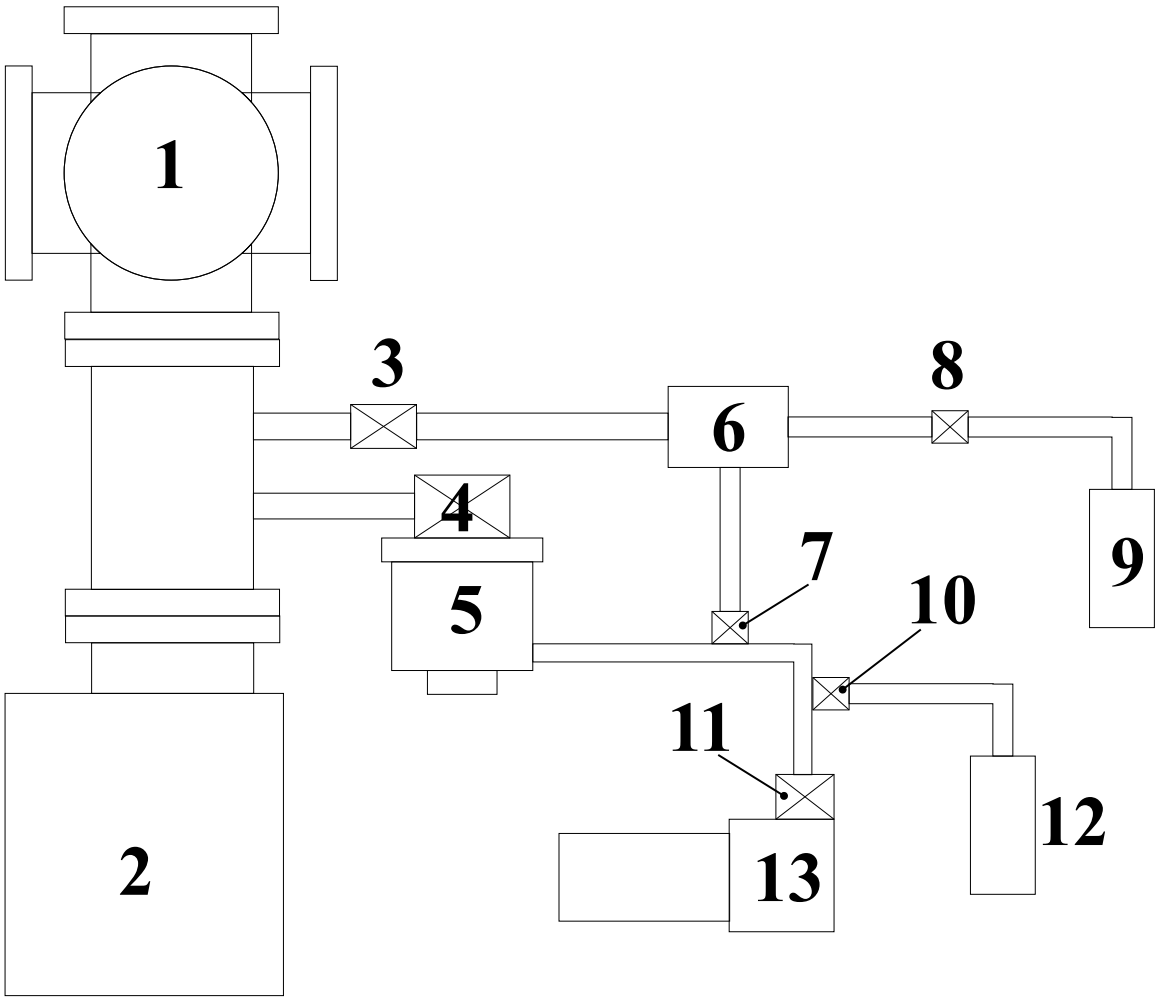

Fig. 2. Schematics of the vacuum system. 1: Six port stainless steel chamber; 2: VacIon pump; 3: High precision leak valve; 4: Turbomolecular pump shutoff valve; 5: Turbomolecular pump; 6: Inert gas (Ar,Xe) reservoir; 7: Inert gas reservoir evacuation valve; 8: Inert gas reservoir fill valve; 9: Inert gas bottle; 10: Needle valve used to leak Helium gas into the foreline; 11: Foreline pump shutoff valve; 12: Helium bottle; 13: Foreline mechanical pump.

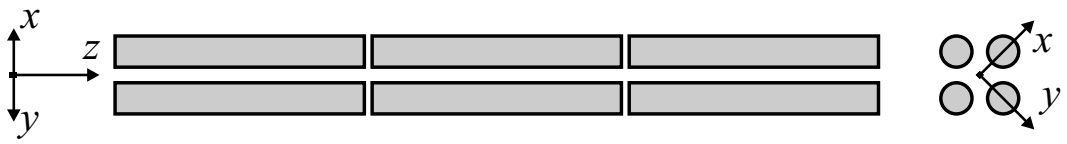

Fig. 3. The ion trap geometry.

The radius of the electrodes is 3mm, the distance from the trap axis to the electrode surfaces is 2.61mm, and the length of each electrode segment is 50mm.

The ion confinement along the axis of the trap is achieved by applying dc offsets to the each of the three segments of the trap electrodes. Usually the dc offset of the center segment is the lowest since it is necessary for the ion detection (the center segment is located opposite to the electron multiplier detector and the fluorescence detection quartz window). The confinement of ions in the radial direction is achieved by applying rf voltage to the electrodes.

2. Rf ion confinement theory

When the rf voltage is applied to the electrodes as described above, the electric field around the trap center is approximately quadrupolar. The quadrupole electric potential due to the rf voltage applied to the rods is given by:

$$\phi(x, y; t) = (U - V cos(\Omega t)) \frac{x^2 - y^2}{2r_0^2}, \tag{2.1}$$

where $-\frac{V}{2} cos(\Omega t)$ is the applied rf voltage, U is the quadrupole dc offset (usually zero), and r_0 is the distance from the trap axis to the electrode surface. The spatial part of the potential in Eq.(2.1) is parabolic, so that along either radial coordinate the potential is parabolic. The orientation of these parabolas quickly alternates with time, the net result being the radial confinement of the ions. The equations of motion

of an ion of mass m and charge e in such a potential are:

$$m\frac{d^2x}{dt^2} = -\frac{e}{mr_0^2}(U - Vcos(\Omega t))x, \tag{2.2}$$

$$m\frac{d^2y}{dt^2} = \frac{e}{mr_0^2}(U - Vcos(\Omega t))y, \tag{2.3}$$

$$m\frac{d^2z}{dt^2} = 0. \tag{2.4}$$

Conventional parameter substitutions:

$$a = a_x = -a_y = \frac{4eU}{mr_0^2\Omega^2}, \tag{2.5}$$

$$q = q_x = -q_y = \frac{2eV}{mr_0^2\Omega^2}, \tag{2.6}$$

$$\eta = \frac{\Omega t}{2}, \tag{2.7}$$

reveal that the equations of motion along radial coordinates, Eq.(2.2) and Eq.(2.3), are the canonical Mathieu equations:

$$\frac{d^2u}{d\eta^2} + (a - 2q\cos(2\eta))u = 0, \tag{2.8}$$

where $u = x, y$. The properties and solutions of the Mathieu equations are well studied. For our purposes the most important property of the Mathieu equations is that their solutions are finite if the values of q and a are properly chosen. The finite character of the solutions translates into the confinement of the particles. An approximate solution of the equations (2.2) and (2.3) is possible for lower values of the q parameter by utilizing the time averages. The motion of the ion is separated into the slow and fast varying parts (called *macromotion* and *micromotion*, respectively). The macromotion of the ion can then be depicted as the result of the *ponderomotive*

force. The ponderomotive force is usually written down as the gradient of the ponderomotive potential, which in the ion trapping field is referred to as *pseudopotential*. The expression for the pseusdopotential is:

$$\Psi(x,y) = \frac{e}{4m\Omega^2}\left[\left(\frac{\partial\phi}{\partial x}\right)^2 + \left(\frac{\partial\phi}{\partial y}\right)^2\right], \tag{2.9}$$

where the partial derivatives are taken over the spatial part of the electric potential[14].

For the quadrupole trapping potential given by Eq.(2.1) the ponderomotive potential takes the form:

$$\Psi(x,y) = \frac{eV_0^2}{m\Omega^2 r_0^4}\left(x^2+y^2\right) = \frac{\overline{D}}{r_0^2}\left(x^2+y^2\right), \tag{2.10}$$

where $V_0 = V/2$ is the amplitude of the rf signal, $\overline{D}$ is the potential depth (in Volts) of the pseudopotential. As one can see from Eq.(2.10), the time averaged effect of the rf quadrupole field is equivalent to a parabolic potential well. Since the motion of a particle in a parabolic potential is oscillatory, the macromotion of the ions in the trap is characterized by the frequency of these oscillations, the *secular frequency*:

$$\omega_s = \frac{\sqrt{2}eV_0}{m\Omega^2 r_0^2} = \frac{eV}{\sqrt{2}m\Omega^2 r_0^2}. \tag{2.11}$$

B. LASER SYSTEM AND UV

The laser and optical system used in these experiments is schematically presented in Fig. 4. The Ar^+ ion laser is a Coherent INNOVA 200 model laser, which is operated in a single wavelength mode at 514.5nm. The laser is operated with the output powers of $4.5-6.5$W. The Ar^+ ion laser output is used to pump the dye laser, Coherent 699-21. Lambdachrome dye Rhodamine 110 dissolved in ethylene glycol was used as the active medium. The range of wavelength that can be obtained using this dye includes

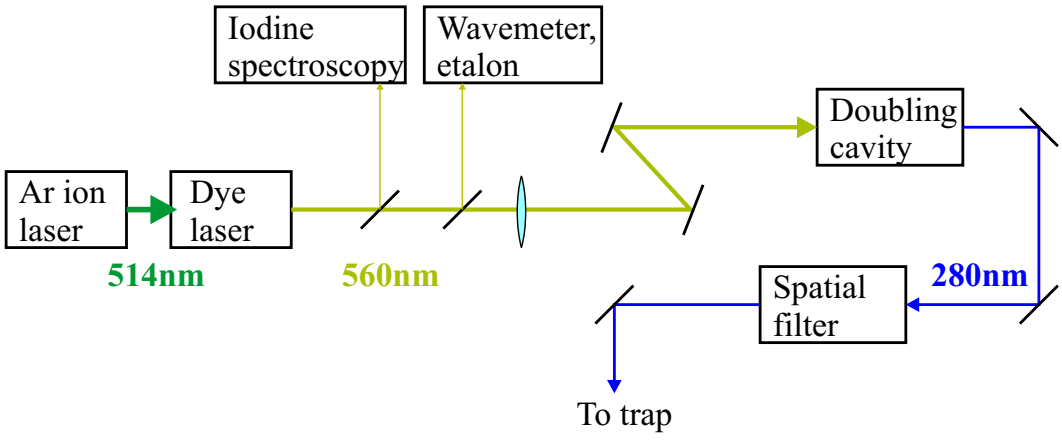

Fig. 4. Block diagram of the laser system.

560nm which is the wavelength that, after frequency doubling, is used for cooling the Magnesium ions. The typical output power of the dye laser is around 400mW at 560nm. While the instantaneous linewidth of the dye laser is only 100kHz, due to acoustic noise the output frequency fluctuates and the effective linewidth is around 3MHz.

Part of the dye laser output is picked off for the iodine saturation spectroscopy which is described in the next chapter, as well as for other means of frequency measurements (wavemeter and scanning etalon). The rest is directed into the external buildup cavity through the mode matching lens. In the buildup cavity the intensity of the light is increased due to the coherent addition of the laser light over multiple paths inside the cavity, and also due to the narrow waist of the cavity mode. The narrow waist of the buildup cavity mode is located inside a nonlinear optical crystal (KDP). The nonlinear interaction generates coherent UV radiation at 280nm wavelenth, which corresponds to twice the dye laser frequency. The highest output power of the UV radiation from the buildup cavity was 1.5mW. Typically 100μW to 800μW

of UV radiation power is used in the experiments. The UV light is sent through the spatial filter to improve the mode, which reduces the scattered light. A polarizing cube is inserted in the UV beam path. Since the UV radiation produced in the doubling cavity is linearly polarized, cube rotation adjusts the UV light intensity. It is then sent through the center of the trap along the trap axis and focused at the center, where it illuminates the Magnesium ions. The iodine spectroscopy is described in detail in the next chapter. The other parts of the laser and optical system are described in detail elsewhere[14].

CHAPTER III

DOPPLER-FREE IODINE SPECTROSCOPY

A. IODINE SATURATION SPECTROSCOPY

1. Iodine absorption lines

The absorption spectrum of the iodine molecule I_2 is widely used as the reference for determining the absolute value of the laser frequency. The iodine atoms have large atomic weight, and the chemical bond between the two iodine atoms in the molecule is weak. As a result, the vibrational frequency of the iodine molecule is small, so the gaps between the vibrational levels are small. The weak chemical bond results in a large distance between the atoms in the molecule. Combined with the large mass of the atoms it produces a high moment of inertia. Therefore the gap between the rotational energy levels is small as well. These factors cause a great many vibrational and rotational sublevels of the ground electronic state to be populated at room temperature. In turn it results in many absorption lines that span the major part of visible spectrum [15, 16]. The iodine absorption spectrum consists of thousands of lines from several to several dozen GHz apart.

2. Doppler-free absorption spectroscopy

Each of the iodine absorption lines is in fact a group of narrowly spaced hyperfine absorption lines[16]. The natural linewidths of the hyperfine lines are quite small (on the order of a few MHz). However, due to Doppler broadening, groups of these lines are merged together. To observe these hyperfine lines, one has to employ a spectroscopic method which is not susceptible to Doppler broadening. The most popular Doppler free spectroscopy method is the so-called *saturation spectroscopy* [17, 18].

The usefulness of the iodine saturation spectroscopy for laser stabilization has increased dramatically with the introduction of the frequency-modulated or heterodyne saturation spectroscopy techniques [19, 20, 21]

Saturation spectroscopy is based on a simple principle: each molecular (or atomic) optical transition can only absorb (scatter) a limited number of photons in a second. When a limited number of molecules (atoms) are exposed to the incoming photon flux they can only remove photons from that flux at a fixed rate. Once that rate is approached any increase in the photon flux will not be absorbed. Therefore the relative attenuation of light passing through an absorbing medium will decrease as the light intensity is increased. This effect is called *saturation* of the absorption. It can be used to target only the molecules that are not moving in the direction of the laser beam and therefore not exhibiting a Doppler shift. To achieve this two beams are sent through the cell filled with iodine vapor. The beams of the same frequency f_P are overlapped and are traveling along the same line in opposite directions. One of the beams is usually much stronger than the other, it's called *the pump beam.* The weaker beam is called *the probe beam* whose transmission is observed. A molecule that has velocity v_z in the direction of the pump beam will see the pump beam as having a frequency of $f_P(1 - v_z/c)$ and the probe beam as having a frequency of $f_P(1 + v_z/c)$ due to the Doppler shift. Thus only the molecules with $v_z = 0$ will see the two beams of the same frequency. If that frequency coincides with one of the absorption frequencies of the molecule, the transmission of the probe beam will increase due to the saturation effect. An example of such a saturation spectrum is shown in Fig. 5.

While it is possible to observe the increase in transmission due to saturation, some extra measures are usually taken to increase the signal level. The setup used for iodine saturation spectroscopy is shown in Fig. 6. In addition to the probe beam that

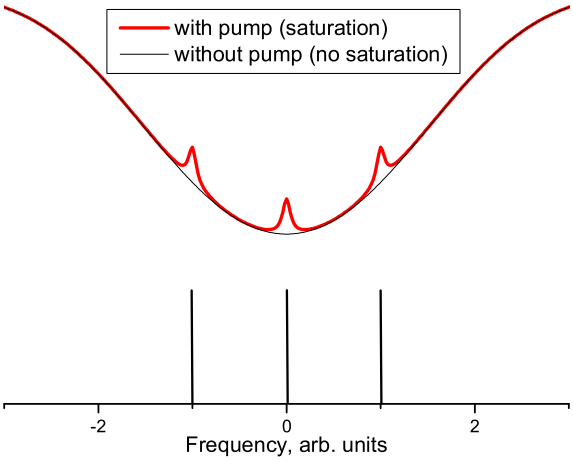

Fig. 5. An example of change in transmission due to saturation. Black (thin) line shows the transmission due to three Doppler broadened absorption lines at frequencies $0, \pm 1$. Red (thick) line shows the transmission when a strong counter-propagating pump beam is present.

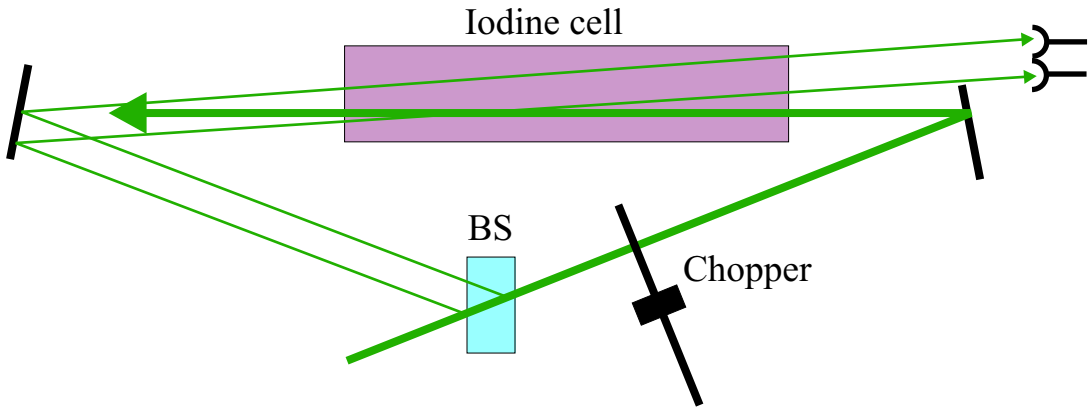

Fig. 6. Optical setup for iodine saturation spectroscopy.

is overlapped with the pump beam, another probe beam is directed through the cell. This extra beam is not overlapped with the pump beam and therefore is not affected by the saturation effect. The difference in the transmission of the two probe beams is measured by a differential photodetector. To improve the signal to noise ratio, a chopper is placed in the path of the pump beam. The chopper periodically interrupts the pump beam, thus periodically introduces and removes the saturation effect in the transmission of the probe beam. Therefore the amplitude of the modulation in the transmission of the probe beam is proportional to the saturation effect. This modulation can be detected by a lock-in amplifier. Using a lock-in amplifier and signal modulation greatly improves the signal to noise ratio.

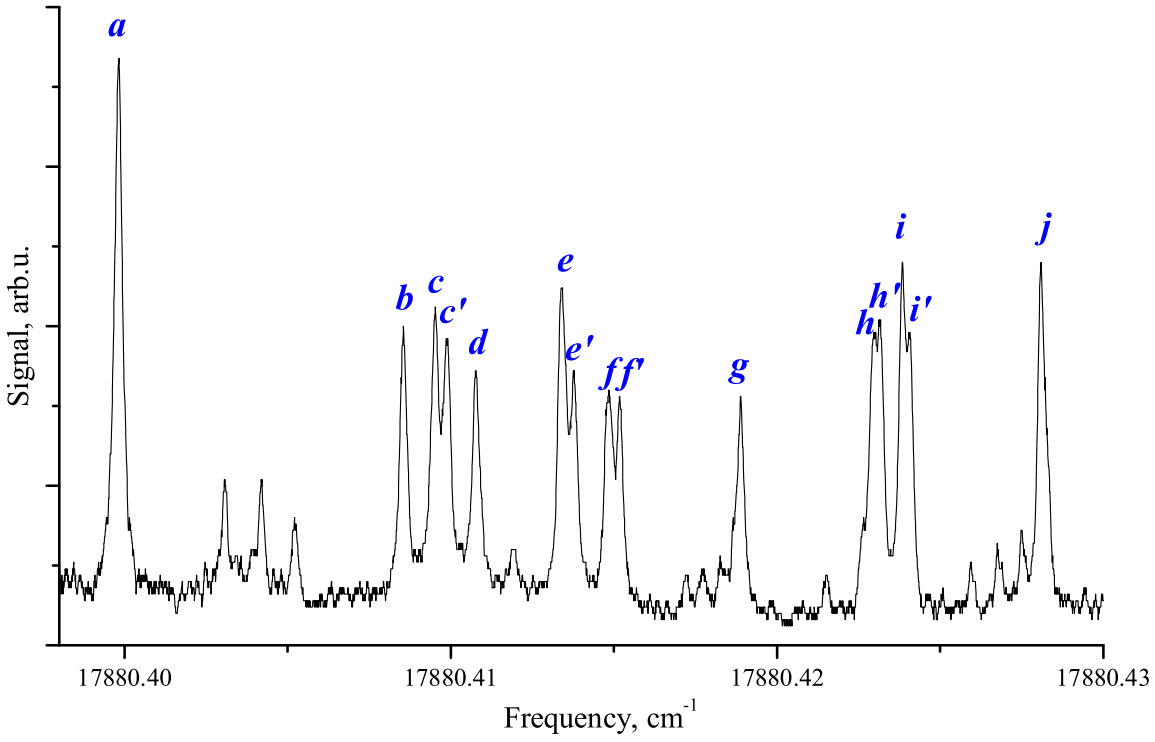

Fig. 7. The iodine saturation signal.

The absorption spectrum of iodine in the frequency range used to cool Mg^+ ions

is shown in Fig. 7. The frequencies of the spectral lines are calculated based on the data from the iodine line atlas[22]. The data in the atlas does not show the splittings for the lines *c,e,f,h,i*, possibly because the experimental conditions used to obtain the atlas data were optimized for the stronger iodine absorption lines. Line positions and the splittings are summarized in Table I.

Table I. Iodine hyperfine line frequency data. The line positions are taken from [22]. The splittings are determined from the experimental data in Fig. 7

Line	Frequency, cm^{-1}	Splitting, MHz
a	17880.39985	–
b	17880.40833	–
c	17880.40937	10
d	17880.41037	–
e	17880.41344	10
f	17880.41498	10
g	17880.41889	–
h	17880.42333	7
i	17880.42427	7
j	17880.42865	–

B. ACOUSTO-OPTIC MODULATOR

The flexibility and range of applications of iodine saturation spectroscopy is greatly enhanced if an acousto-optic modulator (AOM) is integrated into the optical setup.

1. The AOM principle of operation

The acousto-optic effect describes the interaction of light and acoustic waves propagating through the same media[23]. The acoustic wave consists of regions of different mechanical tension. The mechanical tension in the material affects index of refraction. As a result of this acoustic wave an index of refraction grating is created. The spatial period of this grating is equal to the wavelength of the acoustic wave Λ. The optical wave is scattered (diffracted) by this grating. Depending on the interaction length between the optical and acoustic waves the diffraction can occur in two different regimes. The diffraction regime is determined by the value of the dimensionless quality factor Q:

$$Q = \frac{2\pi\lambda L}{n\Lambda^2}, \tag{3.1}$$

where λ is the wavelength of the optical wave, L is the interaction length, n is the index of refraction of the medium.

- **Raman-Nath diffraction** $Q \ll 1$**.** The interaction length is small. This situation is identical to the diffraction on an ordinary diffraction grating such as the ones used in spectrographs and other optical instruments. All diffraction orders can be observed, with their intensities dependent on the incident angle of the beam.

- **Bragg diffraction** $Q \gg 1$**.** The interaction length is large. This situation could be likened to utilizing a series of thin diffraction gratings each causing the Raman-Nath diffraction beams to appear. These diffracted beams undergo constructive and destructive interference. As a result there exists an incident angle for which only one diffraction order is seen and the diffraction efficiency

can reach 100%.

In most applications the Bragg diffraction mode is used. The acousto-optic interaction also depends on the polarizations of the acoustic wave. When the acoustic wave has longitudinal polarization (the material deformation occurs in the direction of wave propagation), the so called isotropic interaction takes place. This type of interaction occurs in homogeneous crystals and can also be achieved for certain orientations in birefringent crystals. In the case of homogeneous or longitudinal-mode interaction the maximum diffraction efficiency is achieved when the light beam is incident at the acoustic grating at the *Bragg angle* θ_B:

$$\theta_B \approx \sin\theta_B = \frac{m\lambda}{2\Lambda}, \tag{3.2}$$

where $m = \pm 1, \pm 2, ...$ is the diffraction order. The intensity of the diffracted light depends on many parameters. For the first order of diffraction it can be written as:

$$\eta_0 = \frac{I_1}{I} = \sin^2\sqrt{\frac{\pi^2 L}{2\lambda^2 H} M_2 P}, \tag{3.3}$$

where diffraction efficiency η_0 is the ratio of the diffracted light intensity to the incident light intensity; H is the height of the acoustic beam, P is the power of the acoustic beam, M_2 is the so called *figure of merit* of the material. P, H, and M_2 together determine the amplitude of the variations in the refractive index. If the incident angle of the light does not exactly match the Bragg angle for a given acoustic wave, the diffraction efficiency will be lower. In this situation the diffraction efficiency is given by the following expression:

$$\eta = \eta_0 \mathrm{sinc}^2\sqrt{\eta_0 + \frac{\Delta\phi^2}{4}}, \tag{3.4}$$

where η_0 is the diffraction efficiency for the ideal angle match as given in Eq.(3.3),

$\Delta\phi = \frac{\pi\lambda L\Delta\Lambda}{2\Lambda}$ is the *phase asynchronism*. At the ideal incidence angle (Bragg angle) the diffraction efficiency is maximum and is decreased with the deviation from that angle. Thus this effect limits the bandwidth of any device based on the acousto-optic interaction. For a fixed wavelength of the incident light the expression (3.4) determines the range of frequencies of the acoustic wave that can diffract this light with acceptable efficiency. Alternatively if the frequency of the acoustic wave is fixed, the above expression limits the range of wavelengths that are diffracted. This bandwidth limiting effect can be minimized by changing the geometry of the acoustic wave. The current solution is to use a divergent acoustic wave. As the light crosses the path of a divergent acoustic wave it consecutively passes through the regions in which it intersects the propagation direction of the wave at different angles, including the desirable Bragg angle. One other thing to point out about employing a range of frequencies in the acousto-optic device is when the frequency of the acoustic wave is changed, so is the diffraction angle. As a result, the direction of the diffracted beam depends on the rf frequency. This effect can be used to scan the direction the laser beam within a narrow range of angles.

An important byproduct of the acousto-optic interaction is that the wavelength of the diffracted light beam is changed. Due to the fact that the diffraction grating is moving with the sound velocity, the corresponding Doppler shift changes the frequency of the diffracted beam. It can be shown that this frequency change is equal to the frequency of the acoustic wave for the first order of the diffracted beam. The sign of this frequency change depends on the direction of the acoustic wave. The easiest way to understand this process is by using momentum and energy conservation of a "scattering" process. This is illustrated in Fig. 8.

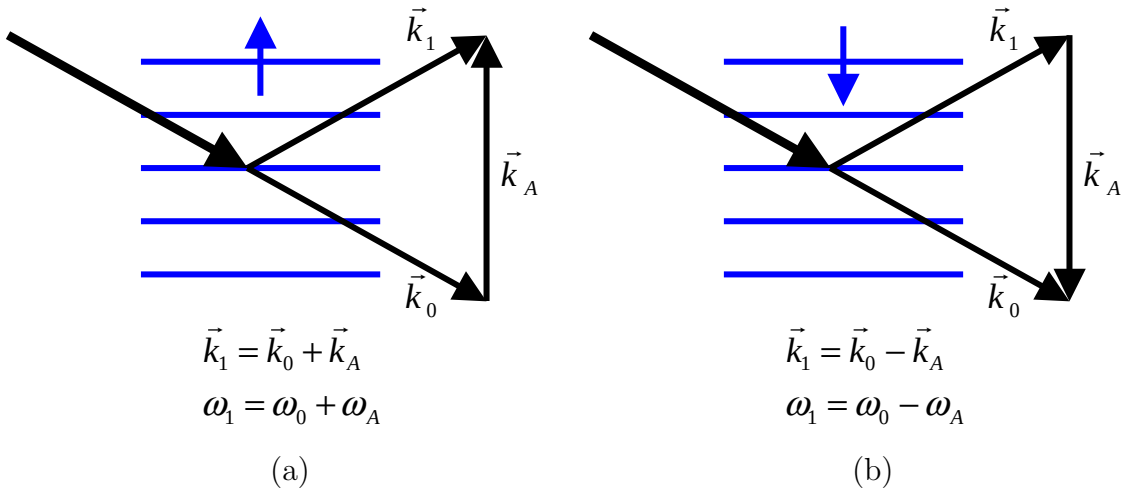

Fig. 8. Momentum conservation picture of the AOM frequency shifting.

2. AOM characteristics and driving electronics

The acousto-optic modulator used in the experiment is built around a tellurium dioxide (TeO_2) crystal, made by Brimrose corporation (model TEF-800-500). The characteristics of the crystal are summarized in Table II.

Table II. Characteristics of the AOM modulator Brimrose model TEF-800-500.

Material	Tellurium Oxide (TeO_2)
Optimized for frequency range	$500 - 1000$ MHz
Active aperture	$50\mu m$
Diffraction efficiency	60%
Bragg angle	53mrad
Acoustic mode	Longitudinal
Acoustic velocity	4200 m/s

In order to provide flexibility in controlling the operating parameters of the modulator, an rf driving circuit was built. Its block diagram is shown in Fig. 9.

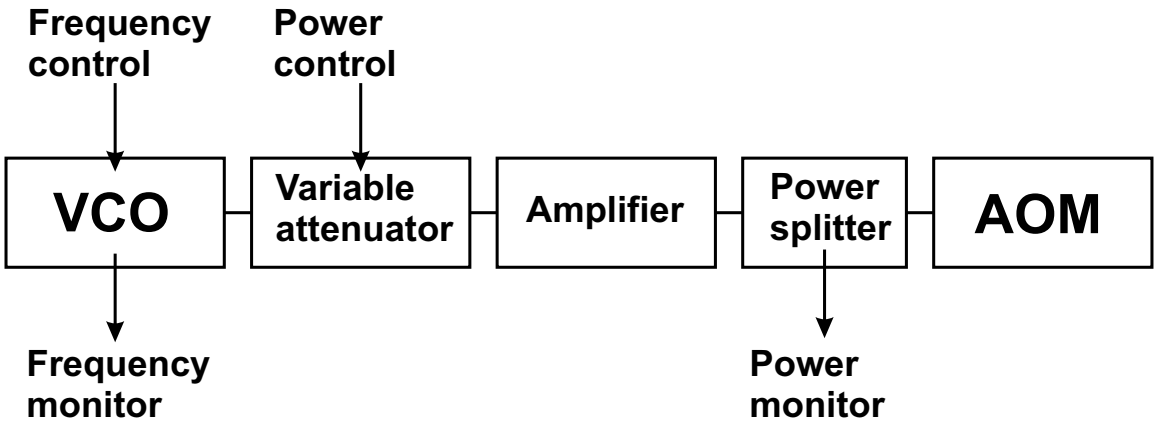

Fig. 9. Block diagram of the AOM rf driving circuit.

The frequency of the rf signal is determined by the voltage applied to the control input of the voltage-controlled oscillator (VCO). The main source of instability of the rf signal frequency produced by the VCO is due to the changes in temperature. To reduce this effect the whole setup is mounted on a 1/2 inch thick aluminum plate that serves as a common heatsink. This way after an approximately 2 hour warm-up period the oscillator frequency remains very stable (the frequency fluctuations are approximately 10kHz per hour). The frequency provided by the VCO ranges from 500MHz to 1050MHz. Normally the VCO frequency is controlled by the output voltage of a DAC channel of the computer. The resolution of the DAC channel is 12 bit which limits the frequency adjustment step to approximately 0.2MHz. A seventh order polynomial of the following form describes output frequency of the VCO as a function of the DAC channel voltage:

$$\begin{aligned} f_{VCO} &= 466.853 + 10.6898 \times V + 33.2079 \times V^2 - 10.5077 \times V^3 + 1.64329 \times V^4 \\ &\quad -0.116756 \times V^5 + 0.00217933 \times V^6 + 7.13719 \cdot 10^{-5} \times V^7. \end{aligned} \tag{3.5}$$

The deviation of the VCO frequency from the polynomial in Eq.(3.5) is given in Fig. 10.

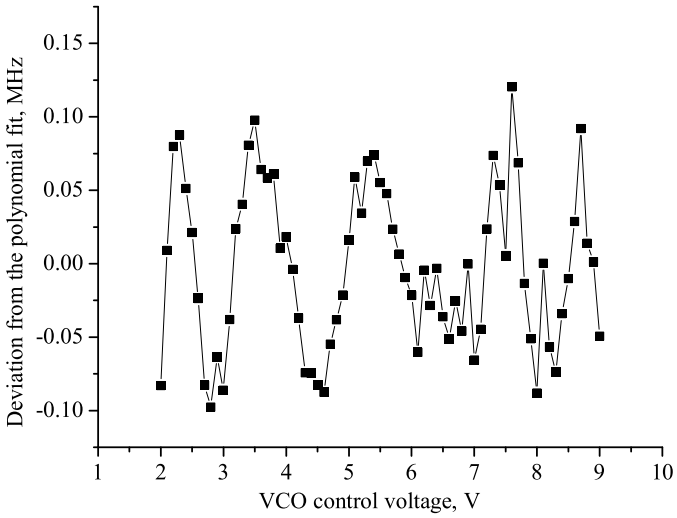

Fig. 10. The deviation of the VCO frequency dependence on DAC control voltage from the polynomial fit. The jagged character of the graph is due to the 12th bit rounding of the DAC voltage.

The signal from VCO is sent through the variable attenuator. The current through the attenuator controls the amplitude of the rf signal on its output. Thus the circuit can control both the frequency and the amplitude of the rf signal. The signal is then amplified to the desired power by the 39dB rf power amplifier and applied to the AOM. Approximately 1% of the rf power sent to the AOM is picked off and rectified to monitor the applied power.

C. THE IODINE SATURATION SPECTROSCOPY SETUP

The iodine saturation spectroscopy setup shown in Fig. 6 earlier has been modified to incorporate the AOM. Two versions of the setup were developed in the course of this research. The first version targets the iodine molecules that have zero velocity

component in the direction of the laser beam. The second version targets a group of molecules whose velocity component in the direction of the laser beam is non-zero. The two versions compliment each other and enhance the functionality of the iodine saturation spectroscopy.

1. Zero-velocity setup

The zero-velocity version of the setup is shown in Fig. 11. The portion of the laser beam picked off the dye laser output is directed through the AOM. Depending on the mutual orientation of the laser beam and the AOM (see Fig. 8), the beam frequency is shifted up or down by the AOM frequency. A small amplitude harmonic modulation signal is added to the frequency control voltage of the VCO, which introduces a modulation into the AOM frequency. In turn this results in the frequency modulation of the dye laser beam. As the end result, the frequency of the laser beam at the output of the AOM is shifted and modulated. The amplitude of the frequency modulation is very small (around 5MHz).

A glass plate is used to pick a pair of probe beams off the main beam. The main (pump) beam is then guided through the iodine cell in one direction, and the two probe beams propagate through the iodine cell in the opposite direction. This results in the classic anti-collinear beam arrangement as was described earlier. Except now the frequencies of the pump and the probe beams are modulated, i.e. they are quickly scanned back and forth across a few MHz wide frequency range. The frequency modulation serves two purposes. First, it facilitates the use of a lock-in amplifier for signal detection. The lock-in amplifier significantly improves the signal-to-noise ratio and stability in the presence of the laser intensity fluctuations. Second, the signal produced by the lock-in amplifier is related to the *derivative* of the saturated absorption. Denote the transmission of the iodine as a function of the laser frequency

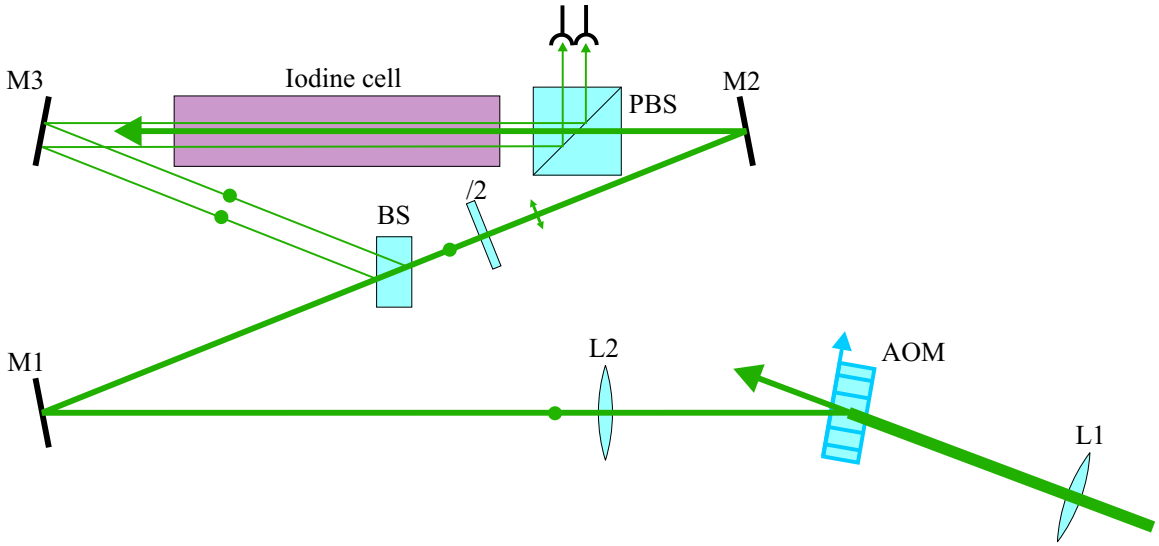

Fig. 11. Optical setup used to perform saturation spectroscopy measurements with AOM and frequency modulation.

as $T(\omega_L)$, then the intensity of the transmitted probe beam in the absence of frequency modulation is $I_0 T(\omega_L)$, where I_0 is the intensity of the transmitted light through an empty cell (no absorption). If we introduce a small frequency modulation so that the frequency of the laser is $\omega_L(t) = \omega_L^{(0)} + \epsilon \cos \Omega t$, the probe beam intensity will be

$$I = I_0 T(\omega_L^{(0)} + \epsilon \cos \Omega t) \approx I_0 T(\omega_L^{(0)}) + \left[\epsilon I_0 \frac{dT}{d\omega} \left(\omega_L^{(0)} \right) \right] \cos \Omega t, \tag{3.6}$$

where the quantity in the square brackets is proportional to the signal at the output of the lock-in amplifier. Thus instead of the peak at the location of a hyperfine line in the iodine spectrum, a *dispersion*-like signal is observed. This signal is used as the error signal to control the laser frequency. The zero crossing point of the error signal corresponds to the maximum of the saturated transmission peak. An idealized shape of the signal is shown in Fig. 12. This lineshape is quite useful in determining the position of the absorption line since finding the zero crossing point is easier than the

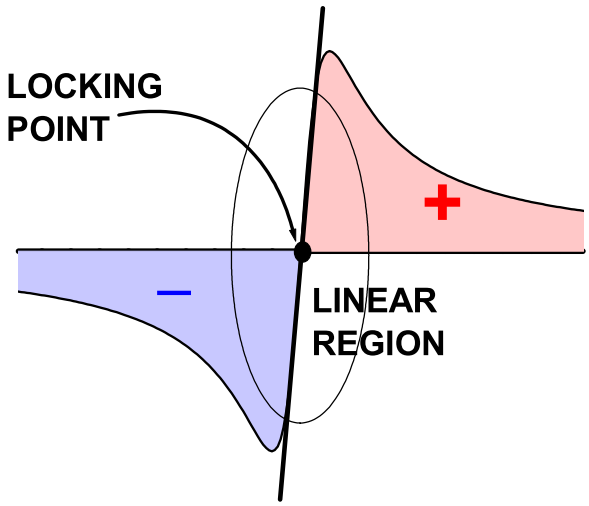

Fig. 12. Typical dispersion-like error signal used for locking purposes.

peak maximum. But most importantly this lineshape can be used for *locking* or fixing the laser frequency to the position of the absorption line. The *locking point*, i.e. the point where the electronics tries to keep the laser frequency, is where the signal crosses zero. It is very useful that the signal around the locking point resembles a straight line, since it means that a linear feedback control can be applied. Linear feedback control theory and the corresponding locking electronics used to keep the laser locked around that point are well developed. Another advantage that a dispersion-like signal has for locking is that the signal has the same sign over a wide range of frequencies on either side of the locking point. The locking electronics is also designed to take advantage of that. The sign of the signal is used to determine in which direction to adjust the laser frequency; such a simple mechanism can bring the laser frequency to the locking point even if it jumps outside the linear region. The block diagram of the electronics used to lock the dye laser to the iodine line is shown in Fig. 13. The error signal is generated by the lock-in amplifier referenced to the same generator

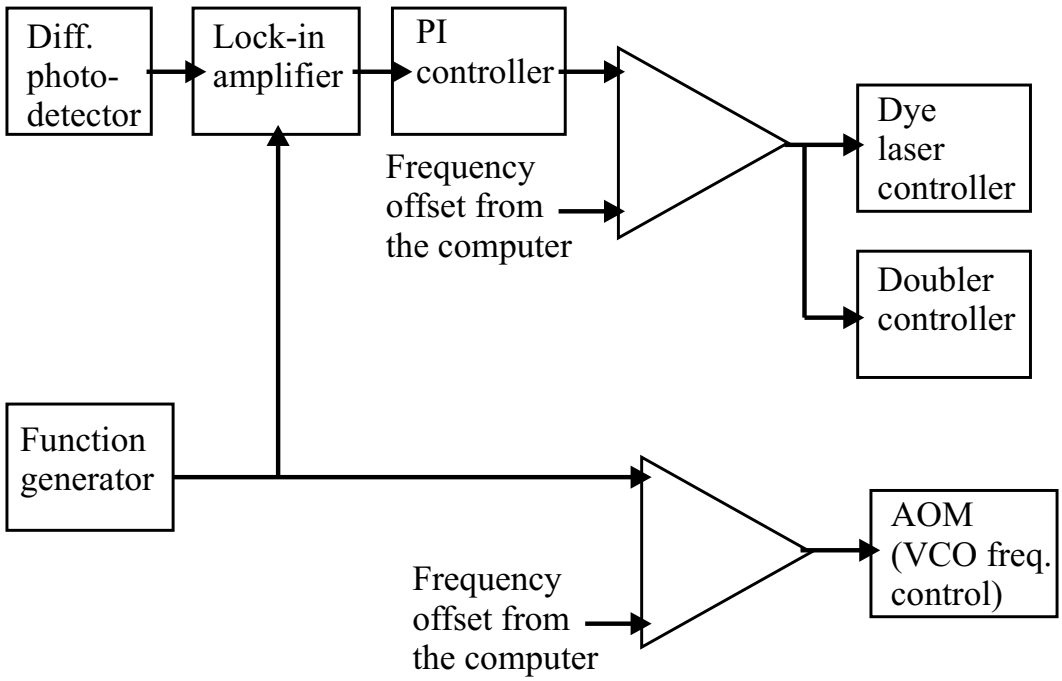

Fig. 13. Block diagram of the electronics for locking to the Doppler-free iodine line.

that modulates the frequency of the AOM. The error signal dependence on the laser detuning from the iodine hyperfine line has general dispersion-like shape as described above. A PI controller is designed to adjust its output so that the error signal is zero. The PI controller used here is of the same type that is used to lock the doubling cavity to the dye laser frequency[14]. The two summing nodes were introduced into the loop to achieve the synchronous frequency scanning of the dye laser and the AOM frequency. The result of such scanning is that the frequency of the dye laser is precisely controlled during the scan of the frequency. However the variations of the AOM diffraction efficiency with the change of the AOM frequency have proven that more advanced electronic and optical parts have to be used to achieve necessary signal quality. Most importantly, the optical quality of the iodine cell windows and a more advanced balanced differential photodetector are crucial for this purpose.

To achieve experimental goals set forth for this research it was sufficient to set the AOM to a fixed frequency for the imaging experiments. It provided long cooling times at a fixed laser frequency and allowed the observation of the laser cooled ion crystals. For the fluorescence lineshape measurements, the set of the iodine absorption lines such as the one seen in Fig. 7 was measured during the laser frequency scan. It provided an accurate reference needed to determine the laser frequency during the scan.

As was mentioned before, the saturation signal amplitude depends on two main parameters: the intensity of the pump beam and how much the pump and the probe beam overlap inside the iodine cell. The change of the AOM frequency alters the direction of the diffracted beam, which can destroy the beam overlap. However, the saturation spectroscopy setup has been designed to maintain perfect beam overlap (the beams are exactly parallel) independent of the rf frequency of the AOM, as illustrated in Fig. 14. The lens at the exit of the AOM is placed in such a way that it produces a collimated beam (the AOM crystal is in the focus of the lens), so that the change in the angle of the diffracted beam will produce parallel beam displacement. To maintain the overlap of the beams inside the iodine cell the glass plate which is used to pick off the probe beams is placed at the top of an equilateral triangle. As can be seen from Fig. 14, while the AOM frequency changes the beam direction the optical arrangement transforms this change into translational motion of all the beams inside the iodine cell, while maintaining the beams angles and positions relative to each other. To allow for perfect beam overlap the polarization of the pump beam is rotated 90 degrees and a polarizing beamsplitter cube is placed in the path of the beams. The pump beam passes through the cube while the probe beams are deflected and sent to the detection electronics as illustrated in Fig. 11.

The iodine hyperfine absorption lines provide a fixed set of wavelengths that the

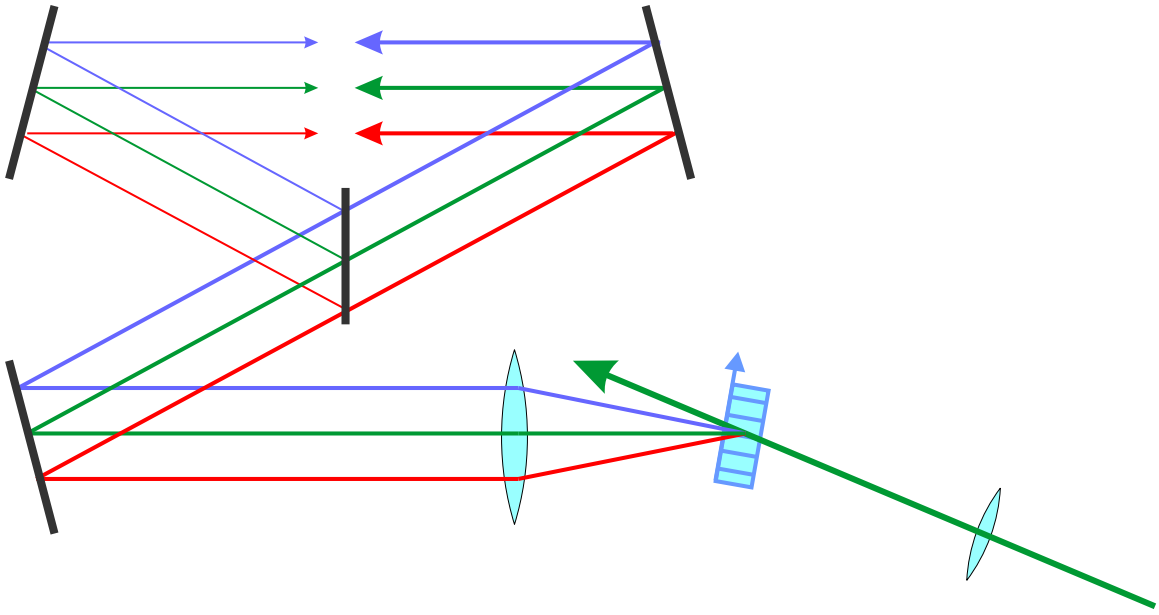

Fig. 14. Maintaining the beam overlap for different AOM deflection angles.

laser can be locked onto. The AOM shifts the position of the iodine absorption lines *relative to the dye laser frequency*, because the iodine absorption is measured using the frequency shifted laser beam. For example, consider the case when the position of some hyperfine iodine line is at frequency f_{hf}, and the AOM can shift the frequency in the range from 500MHz to 1000MHz. By keeping the AOM shifted beam on the iodine absorption line, the main dye laser beam can be in one of the two frequency bands: $f_{hf} - 1000MHz$ to $f_{hf} - 500MHz$ or $f_{hf} + 500MHz$ to $f_{hf} + 1000MHz$, depending on the AOM orientation. Therefore we have a $\pm 500MHz$ "dead band" around the absorption line. The next section describes a way to reduce this "dead band".

2. Nonzero-velocity setup

A variation of the previous setup can be used. In this case the probe beams are provided by the AOM as before, but *the pump beam is not frequency shifted.* There are two ways to achieve this:

- pick off another small portion of the main laser beam and use it as a pump beam;
- a more economic use of the laser power would be to use the undiffracted beam that passes through the AOM; in this case the AOM can be run at low diffraction efficiency parameters to increase the power of the undiffracted (pump) beam.

Unlike the previous case, where the pump and the probe beams have the same frequency, now the pump and the probe beams have different frequencies and the group of molecules targeted for saturation spectroscopy is moving in the direction of the laser beams $v_z \neq 0$. Let us assume that the frequency of the pump beam is f_1 and the frequency of the probe beam is $f_2 = f_1 + f_{AOM}$. In order for the saturation absorption reduction in the probe beam to occur both the pump and the probe beam have to be seen as having the same frequency f_0 by a group of molecules. It is possible if

$$f_0 = f_1 \left(1 + \frac{v_z}{c}\right) = f_2 \left(1 - \frac{v_z}{c}\right), \tag{3.7}$$

or

$$\left(1 + \frac{v_z}{c}\right) = \left(1 + \frac{f_{AOM}}{f_1}\right) \left(1 - \frac{v_z}{c}\right). \tag{3.8}$$

The solution to equation (3.8) is that the frequency f_0 and the velocity of the targeted group of molecules are:

$$\begin{aligned} f_0 &= f_1 + \frac{f_{AOM}}{2 + f_{AOM}/f_1} \approx f_1 + \frac{f_{AOM}}{2}, \\ v_z &= c\left(\frac{f_0}{f_1} - 1\right) \approx c \cdot \frac{f_{AOM}}{2f_1}. \end{aligned} \tag{3.9}$$

There is a factor that limits the applicability of this method, since it requires a group of ions to be moving with certain velocity. The larger the AOM frequency shift the higher the velocity. However, the number of ions with higher velocity values decreases according to the Gaussian velocity distribution. This reduces the signal from saturated absorption. Ultimately the Doppler broadening determines the range of useful AOM frequency shifts. Half of the Doppler broadened linewidth of the molecular iodine at room temperature for laser wavelength of $560nm$ is approximately 210MHz. In this configuration the saturation absorption targets the molecules that have the Doppler shift equal to the half of the AOM frequency (see Eq.(3.9)). If the AOM frequency shift is 420MHz, the saturation spectroscopy targets the molecules whose Doppler shift is 210MHz. The signal due to saturated absorption is reduced by a factor of 2 compared to the configuration that uses zero-velocity molecules. As the Gaussian distribution declines very rapidly, doubling the AOM frequency to 840MHz reduces the signal by a factor of 16. I was able to observe the saturation signal for the lower range of frequencies accessible with the help of the AOM (≈600MHz). It is certainly possible with the help of better photodetector and lock-in amplifier to obtain signal levels usable for the laser frequency locking even at the highest AOM frequency (≈1000MHz). Overall this method has a future in extending the frequency range accessible with the AOM.

CHAPTER IV

MOLECULAR DYNAMICS SIMULATIONS OF LARGE ION CLOUDS

A. INTRODUCTION

The *molecular dynamics* (MD)[24, 25, 26] methods are based on the idea that the knowledge of the interparticle interactions allows for the direct numerical solution of the equations of motion of the particles. Studying the numerical solutions allows prediction and description of the bulk properties of the system, system dynamics and other complicated phenomena that do not yield to analytical methods. Since this method requires extensive numerical calculations, first research[27, 28, 29] using the molecular dynamics approach appeared when the first computers became available.

Applying the molecular dynamics methods to the non-neutral plasma confined in an ion trap is met with extra difficulties as compared to the traditional liquid or solid state simulations. First, the Coulomb interaction between the particles in the plasma has a theoretically unlimited range. Therefore it is impossible to limit the interactions between the particles to just a few neighbors. Ideally one would have to account for interactions between *each pair of particles* in the system. Second, in addition to the Coulomb interaction between the particles there is an external oscillating potential. This introduces many different time scales into the picture, such as the timescale of the ion's secular oscillation (10^{-5}s), and the timescale of the particle motion in the oscillating potential (10^{-7}s). A timestep has to be chosen so that it is small on the fastest timescale, yet in order to deduce any meaningful conclusions the simulation has to continue long enough even on the slowest timescale. All this makes the molecular dynamics simulations of the ion trap plasma much more computation intensive. Most of the time the numerical effort in the ion trapping area is concentrated on a single

ion[30], and the influence of the other trapped particles is introduced through some sort of averaged potential[31]. However, despite the difficulties, the MD approach has been used to obtain the density distribution of the ions in the trap, as well as some dynamic properties of the ion crystals in spherical[32] and linear[33] rf traps. The scale record in this area is held by the recent simulation[34] that involved 1000 ions, whose motion is monitored for $50,000$ oscillation periods of the trapping field.

B. DESCRIPTION OF THE APPROACH

1. Equations of motion

In this MD calculation the equation of motion for each ion,

$$\frac{d^2\vec{r}_i}{dt^2} = \frac{\vec{F}_i}{m_i}, \tag{4.1}$$

is solved numerically. In Eq.(4.1) $\vec{r}_i$ and m_i are position vector and mass of the ith particle, respectively; $\vec{F}_i = \vec{F}_i(\vec{r}_1, ..., \vec{r}_N, \vec{v}_1, ..., \vec{v}_N; t)$ is the total force acting on the ith particle, which may depend on the positions and the velocities of all other of the total of N ions, and time. There are several contributions to this force:

$$\vec{F}_i(\vec{r}_1, ..., \vec{r}_N, \vec{v}_1, ..., \vec{v}_N; t) = \vec{F}_i^{(trap)} + \vec{F}_i^{(coulomb)} + \vec{F}_i^{(stoch)}. \tag{4.2}$$

The trapping force $\vec{F}_i^{(trap)}$ is determined by the trapping potential through the relation $\vec{F}_i^{(trap)} = \nabla_i U_{trap}(\vec{r}_i, t)$. It only depends on the position of the ion in question and on time. It can take two forms. In the first form the trapping potential is approximated by its time averaged effect, i.e. the ponderomotive potential as in Eq.(2.10). In the second form the trapping potential is a time dependent oscillating harmonic potential as in Eq.(2.1). In either case the trapping force only has components perpendicular to the trap axis. The trapping force is responsible for the confinement

of the ion cloud in the radial direction. The Coulomb force $\vec{F}_i^{(coulomb)}$ is due to the Coulomb repulsive forces between each pair of ions in the trap:

$$\vec{F}_i^{(coulomb)} = \sum_{j=1, j\neq i}^{N} k_C \frac{Z_i Z_j e^2}{r_{ij}^2}, \frac{\vec{r}_{ij}}{r_{ij}} \tag{4.3}$$

where $\vec{r}_{ij} = \vec{r}_i - \vec{r}_j$ is the displacement between the ith and the jth ions, k_C is the Coulomb constant, Z_i is the charge of the ith ion. The stochastic force $\vec{F}_i^{(stoch)}$ is due to the random interactions of the ions with their surroundings, such as collisions with the buffer gas and the scattering of the laser light. The stochastic force includes two different aspects of such random interactions: the fluctuations that randomize the trajectories of the ions and the dissipation that describes the exchange of energy through these interactions.

2. Geometry of the problem

The coordinates used in the simulation are the same as shown in Fig. 3 depicting the ion trap. In it the z-axis is directed along the trap axis and the x- and y- axes are perpendicular to the trap axis and point towards the trap rods. As was stated earlier, simulating a very large number of ions is so computation intensive that it makes the direct MD simulations of large ion crystals ($N > 30,000$) impossible. Since in the case of our trap, and many other linear traps, the size of the ion cloud along the z-axis is much larger than its radial size, the edge effects along the trap axis can be neglected. Therefore, the ion cloud can be considered *infinite* along the z-axis. The advantage of considering an infinite cloud is that by employing the so-called *periodic boundary conditions* (*PBC*) [24, 25, 26], the equations of motion are only solved for a portion of ions that are present in a slice of the cloud. The idea behind the PBC is that the infinite cloud is formed by periodic replication of the slice being simulated. One

consequence of the replication is that for each particle in the slice there is an infinite number of clones, or images of this particle, which are offset along the z-axis by an integer number of slice widths. This is shown in Fig. 15(a). While the equations of motions are solved for the particles in the slice, the PBC dictates that the following conditions are to be observed:

- If during the computation the ion is forced out of one side of the slice boundary, it is re-introduced into the slice at the opposite side of the boundary. The velocity of the particle remains the same. This is illustrated in Fig. 15(b). As the particle crosses the slice boundary, its image is entering the slice from the opposite boundary.

- The Coulomb interaction forces are calculated using the *minimum image convention* as illustrated in Fig. 15(c). Since the main computational effort involves calculating the interaction forces between all the particles in the system, using only a slice of the crystal doesn't provide computational advantage, if the interactions between all the images were to be calculated. However when using the minimum image convention the computational effort is reduced since it limits the calculations to the closest neighbors, particles or clones. Figure 15(c) illustrates it by showing the interactions of ion 1 as lines connecting it to other ions/clones. A solid line indicates that the particular pair interaction is taken into account. The dashed line indicates that there is a duplicate ion that is closer, and therefore this pair interaction is discarded. The minimum image convention also ensures that when the particle is re-introduced into the system as described in the previous paragraph, it doesn't change the potential energy of the system.

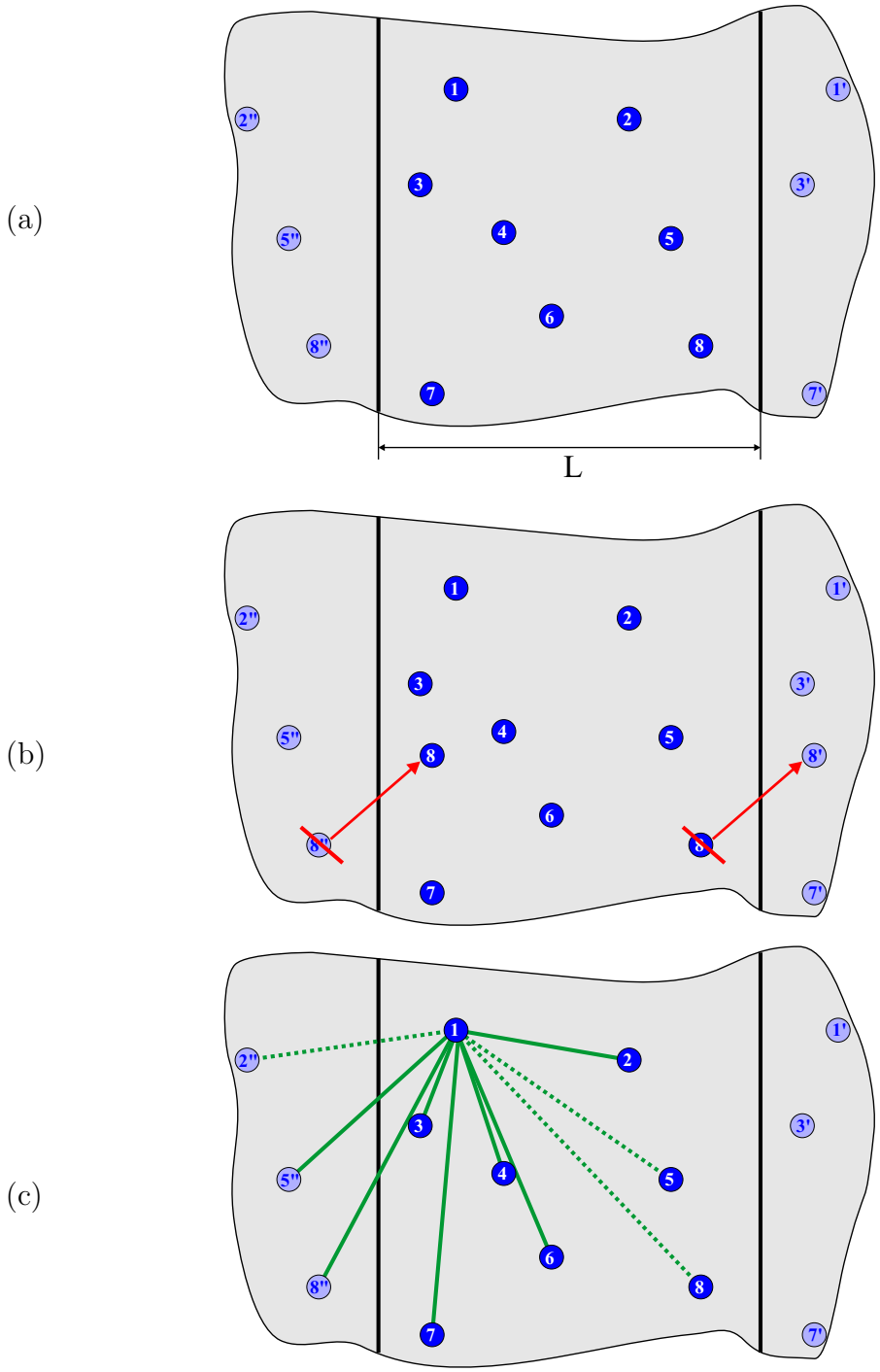

Fig. 15. The periodic boundary conditions. (a) The periodicity; (b) The crossing of the slice boundary; (c)The minimum image convention.

The minimum image convention of the PBC effectively truncates the interaction distance between the ions. In the plasma the collective effect of all the charges effectively limits the interaction length to the so-called Debye radius[35]. The length of the slice must be chosen much larger than the Debye radius of the confined ion plasma, for the PBC to produce good results.

3. Gear algorithm

To solve the equation of motion of the i^{th} particle (4.1), the *Gear algorithm*[36] is applied. The Gear algorithm is used here because of its very important property: it needs to calculate the forces acting on each particle only once each time step. It defines the following 6-element vector quantity for each of the particles:

$$q_{i,\alpha} = \begin{bmatrix} r_{i,\alpha} \\ \Delta t \frac{dr_{i,\alpha}}{dt} \\ \frac{(\Delta t)^2}{2} \frac{d^2 r_{i,\alpha}}{dt^2} \\ \frac{(\Delta t)^3}{6} \frac{d^3 r_{i,\alpha}}{dt^3} \\ \frac{(\Delta t)^4}{24} \frac{d^4 r_{i,\alpha}}{dt^4} \\ \frac{(\Delta t)^5}{120} \frac{d^5 r_{i,\alpha}}{dt^5} \end{bmatrix}, \tag{4.4}$$

where $i = 1, \ldots, N$ is the particle number and $\alpha = x, y, z$ is the coordinate index. First step of the algorithm is to predict the new values of the vector, $q^p_{i,\alpha}$. The prediction is based on the Taylor series expansion and does not involve the equation of motion. Based on the original value of the vector $q^o_{i,\alpha}$ the Taylor series expansion result can be written in the following matrix form:

$$q^p_{i,\alpha} = \begin{bmatrix} 1 & 1 & 1 & 1 & 1 & 1 \\ 0 & 1 & 2 & 3 & 4 & 5 \\ 0 & 0 & 1 & 3 & 6 & 10 \\ 0 & 0 & 0 & 1 & 4 & 10 \\ 0 & 0 & 0 & 0 & 1 & 5 \\ 0 & 0 & 0 & 0 & 0 & 1 \end{bmatrix} q^o_{i,\alpha}. \tag{4.5}$$

The position and the set of its derivatives represented by the vector q at the end of the time step Δt is called the corrected value $q^c_{i,\alpha}$. It is calculated using the equation of motion of the system:

$$q^c_{i,\alpha} = q^p_{i,\alpha} + \hat{c}\left(\frac{\Delta t^2}{2}\frac{F_{i,\alpha}}{m_i} - \frac{\Delta t^2}{2}\frac{d^2 r^p_{i,\alpha}}{dt^2}\right), \tag{4.6}$$

where $\frac{\Delta t^2}{2}\frac{d^2 r^p_{i,\alpha}}{dt^2}$ is the third element of the predicted vector $q^p_{i,\alpha}$. $\hat{c}$ is the vector of corrector coefficients. The values of corrector coefficients are dependent on the order of the equation of motion as well as its functional form. In our case the equation is of second order and the forces are strictly functions of the particle positions. In that case the corrector coefficients are:

$$\hat{c} = \begin{bmatrix} \frac{3}{20} \\ \frac{251}{360}\frac{1!}{\Delta t} \\ 1\frac{2!}{\Delta t^2} \\ \frac{11}{18}\frac{3!}{\Delta t^3} \\ \frac{1}{6}\frac{4!}{\Delta t^4} \\ \frac{1}{60}\frac{5!}{\Delta t^5} \end{bmatrix}. \tag{4.7}$$

In the case when the forces are also dependent on the velocities of the particles, the first corrector coefficient of 3/20 is replaced with the value of 3/16.

4. Initial conditions

In order to solve the equations of motion Eq.(4.1), initial positions and velocities must be known for each ion. The velocity distribution of the ions at a certain temperature is Gaussian. Thus the initial values of the velocity are assigned to individual ions from a Gaussian random number generator. The radial ion distribution of the ions at high temperatures is Gaussian, so at high temperatures the initial positions of the ions are randomly generated in the same way as the initial velocities. As the temperature gets lower, the shape of the radial distribution is no longer Gaussian (for details see Chapter V describing the plasma thermodynamics). Therefore it is not possible to obtain the initial positions of the ions by using some form of random number generation. A different approach is needed.

For the lowest temperature, the radial and velocity distributions of the ions were determined in the following way. First, an initial ion configuration is generated at high enough temperature so that the coordinate distribution is Gaussian. Then, the system is allowed to evolve over many rf oscillation periods (usually over $20,000$) with a friction term introduced into the equations of motion. The presence of friction impedes the thermal motion and dissipates the initial kinetic thermal energy. Initially the friction term is very small and is gradually increased, so that the dissipation is increased when the ions settle into the crystal structure. The evolution of the ions brings them into the crystalline structure with the temperature of the system reaching around 10^{-7}K due to friction. Then the friction is gradually removed and the ions are allowed to evolve without friction for a long time to establish proper radial and velocity thermal distributions. This takes approximately $100,000$ rf oscillation periods. One of the results of this simulation is that at low temperatures (below 100mK) the heating from the rf field is undetectable. Thus at the end of this thermalization period the ion

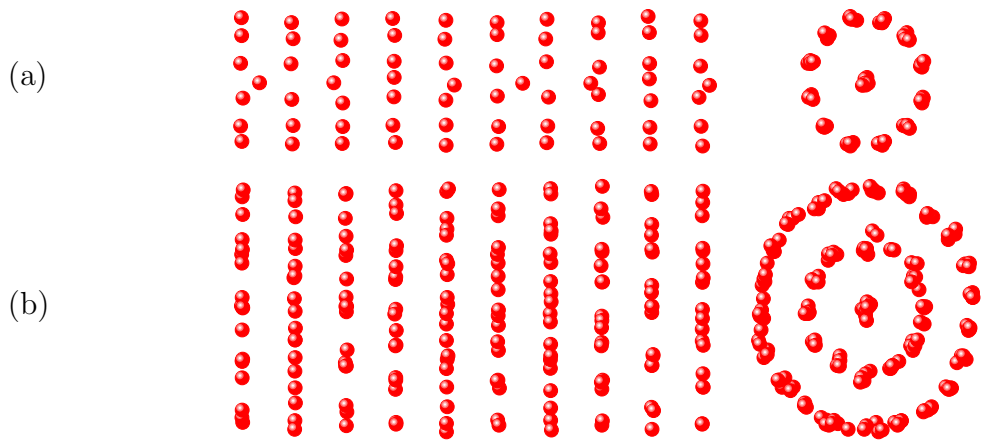

Fig. 16. The ion positions at the low temperatures. (a) the linear density of ions is 340 ions/mm (68 ions in 200μm segment were used in calculation); (b)the linear density of ions is 930 ions/mm (186 ions in 200μm segment were used in calculation);

temperatures are still very low: $10^{-5} - 10^{-6}$K. The ions arrange into the shell crystal structures at these temperatures, as shown in Fig. 16. Such low temperatures have not been achieved in the ion trap, and therefore are not studied in detail. The initial conditions for the higher temperatures ($T >$ 1mK are of interest) are generated by taking the initial conditions for the closest lower temperature, scaling up the velocities to match the new higher temperature, and allowing the system to thermalize over $100,000$ rf oscillation periods.

C. EVOLUTION OF THE ION CLOUD IN THE RF FIELD

The most important question to be answered in these simulations is the evolution of a large ion cloud in the trapping rf field. The solution for a single particle in the rf field is available analytically[37, 38]. However, the solution is not valid when many particles interact with each other, as well as with the rf field. There are many physical properties that can be determined through these computer simulations. Radial

distributions, velocity distributions, and the heating rates of the ion clouds under different conditions are described in the following sections.

1. Radial ion number distribution

After the initial ion distribution is generated as described above, the ions are allowed to evolve over a number of rf oscillation periods (usually 2000) to calculate the thermalized radial distribution. During this time evolution the distance of an ion from the trap axis is calculated according to the following different procedures:

- The average ion position over an oscillation period is used. This way the ion oscillations due to the rf field are averaged out.
- The ion position at a specific phase of the rf field is used. This way the influence of the ion motion due to the rf field is revealed. The phase values of $\pi/2$,π, $3\pi/2$ and 2π are used.
- The ion positions at the time when the kinetic energy is at the minimum are used.
- The ion positions at every integration step are used. In a sense this is the true ion distribution, since it reflects the probability to find the ion at certain position at an arbitrarily chosen moment of time.

The difference between the different methods outlined above is illustrated in Fig. 17. The probability distribution in Fig. 17(a) corresponds to an ion crystal consisting of an inner string and one outer ion shell. These features show up clearly in the graph. The inner string of ions remains unchanged independent of the probability calculation method, which means that it remains virtually unperturbed by the rf trapping field. As one can see from the figure, despite the variety of calculating

(a)

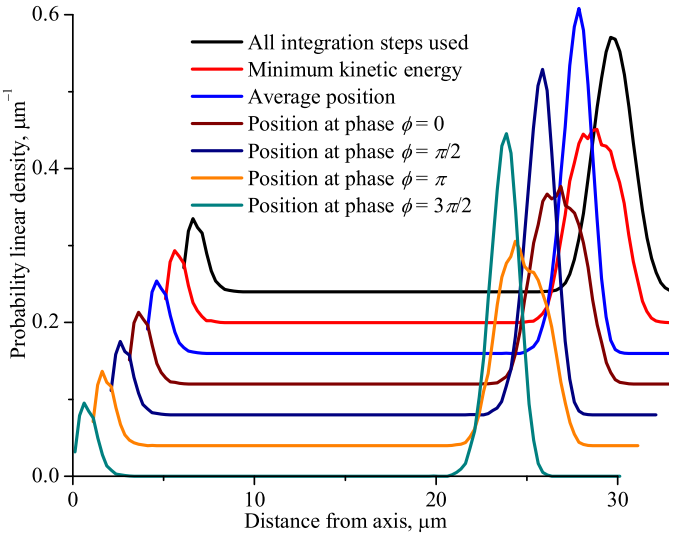

(b)

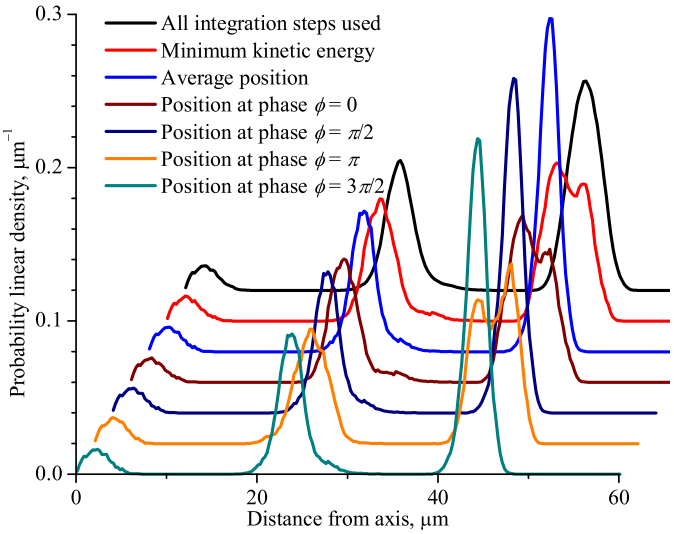

Fig. 17. The radial probability linear density of finding an ion at a given distance from the trap axis for different calculation methods. (a) the linear density of ions is 340 ions/mm (68 ions in 200μm segment were used in calculation); (b)the linear density of ions is 930 ions/mm (186 ions in 200μm segment were used in calculation);

methods the graphs can be divided into three distinct groups based on the appearance of the outer ion shell. The first group consists of the graph that calculates the average particle position, and the graphs for particle positions at the rf trapping field phase $\pi/2$ and $3\pi/2$. On these graphs the outer shell is represented by a single sharp peak, which means that at phase $\pi/2$ (or $3\pi/2$) the particle is located at its oscillation center, i.e. it would normally have the maximum velocity in the oscillation. The second group consists of the graph that calculates particle positions at the time when the total kinetic energy is at a minimum, and the graphs for particle positions at the rf trapping field phase 0 and π. On these graphs the outer shell is represented by a wider peak. It means that at phase 0 (or π) some ions are closer and some are further from the trap axis relative to the position of their oscillation center. At the same time it tells us the particles are almost at rest at that time (since this matches the minimum kinetic energy condition). It should be noted that the evolution of the radial probability distribution is consistent with the behavior of a free particle under the influence of an oscillatory force. The maximum displacement corresponds to the maximum magnitude of the force. Lastly, on the graph that takes into account particle positions at each integration point the outer shell is represented by a peak that is expectedly the average of the peaks of the first and the second groups. Figure 17(b) illustrates the same tendencies repeated for a larger ion crystal which contains one extra ion shell. One can also see that the amplitude of the ion oscillations in the outer shell is large enough to distinguish two peaks corresponding to the maximum displacement of the ions.

The evolution of ion distribution with temperature can be seen in Fig. 18 and Fig. 19. Figure 18 shows the radial probability distributions at low temperatures. As the temperature is increased we witness the "melting" of the ion crystal: the peak features corresponding to the shell structure disappear. At the same time the average

(a)

(b)

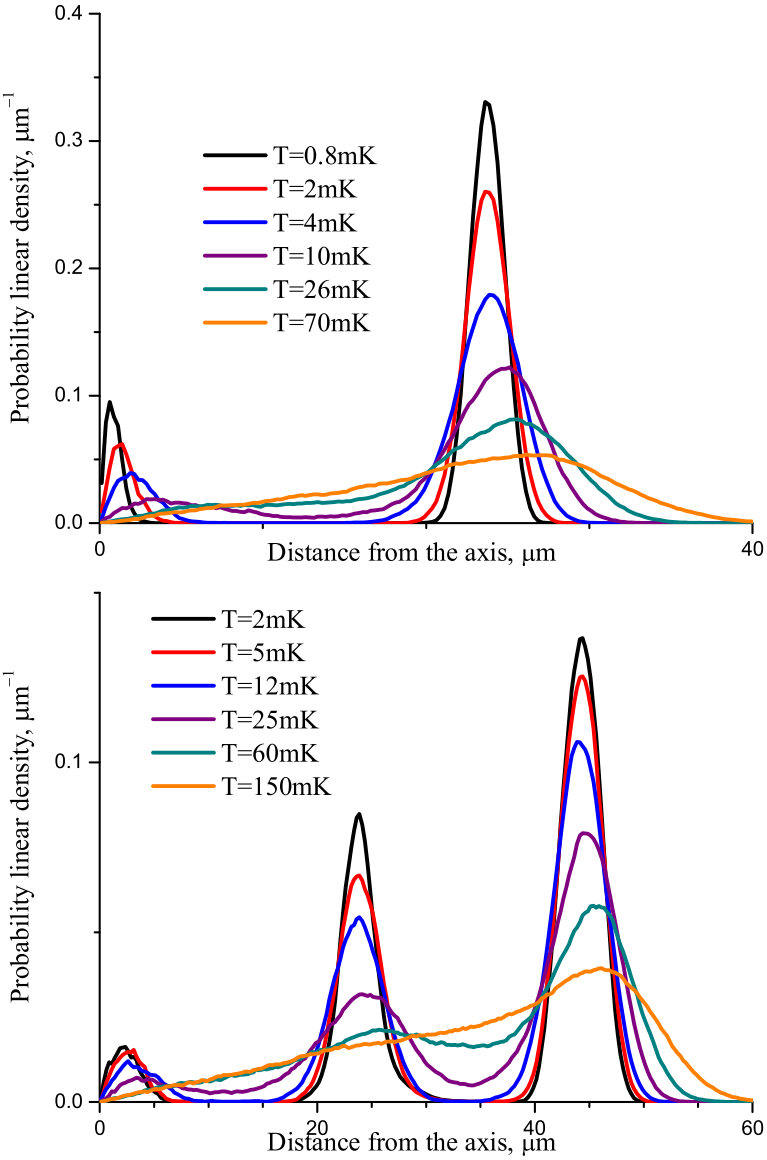

Fig. 18. The probability linear density of finding an ion at a given distance from the trap axis, low temperatures. (a) the linear density of ions is 340 ions/mm (68 ions in 200μm segment were used in calculation); (b)the linear density of ions is 930 ions/mm (186 ions in 200μm segment were used in calculation);

(a)

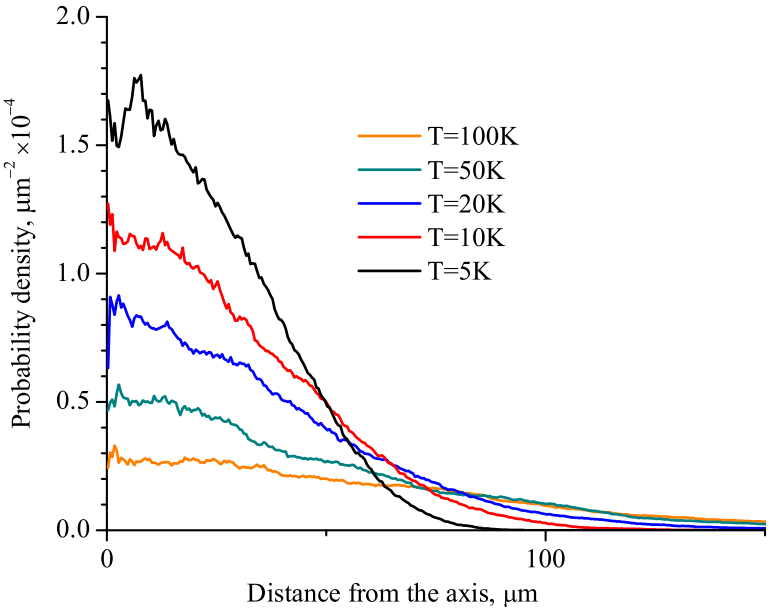

(b)

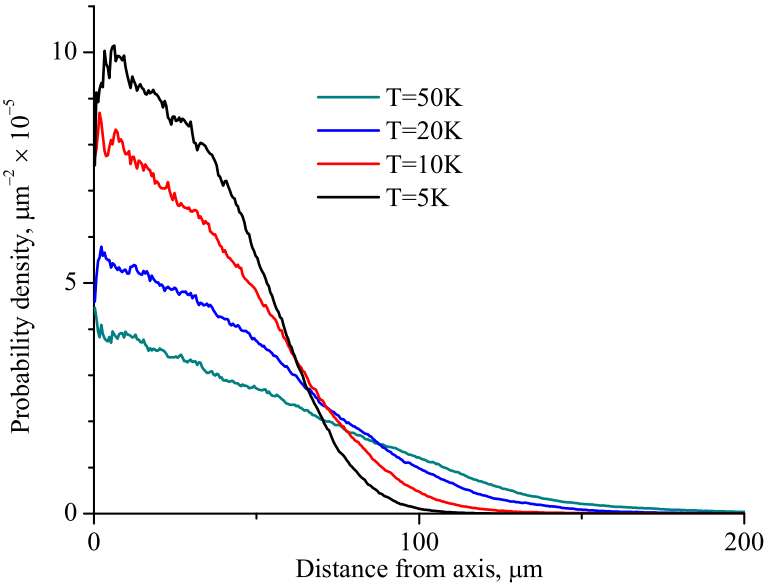

Fig. 19. The probability area density of finding an ion at a given distance from the trap axis, high temperatures. (a) the linear density of ions is 340 ions/mm (68 ions in 200μm segment were used in calculation); (b)the linear density of ions is 930 ions/mm (186 ions in 200μm segment were used in calculation);

ion density of the crystal, or its mean square radius, remains practically unchanged. The ion radial densities at higher temperatures are illustrated in Fig. 19. It is noted that the physical quantity displayed in Fig. 19 is the *probability area density*, and not the linear density as in the previous figures. At higher temperatures the probability distributions calculated by different methods become practically identical and therefore one could use any one of the methods described above for calculations. The theory predicts that the probability density remains constant until a certain distance from the trap axis and then falls off to zero over a distance of the Debye length (for the analytical predictions of the radial distribution of the ions please refer to Chapter V that briefly discusses the plasma thermodynamics). In practice, however, we can see that there is a slight deviation from the theoretical prediction. While the rapid Gaussian decrease on the Debye scale beyond a certain distance from the trap axis indeed takes place, the probability density is not quite constant in the central region. The narrow drop in probability density around $r = 0$ along with the slow dropoff away from the trap axis are attributed to the ion oscillations. The graphs shown in Fig. 19 serve illustrative purposes. Their accuracy is limited by the fact that at the higher temperatures the size of the simulation slice along the axis of the trap is less than the Debye shielding radius.

2. Velocity distribution

The velocity distributions are important to answering some of the central questions of these simulations. Since the ion motion happens on different time scales, and consequently it is classified into the micromotion and macromotion, it is important to determine how each type of motion is reflected in the ion velocity distributions. In the ion MD simulation mentioned earlier[34] the velocity value averaged over one oscillation period was used to determine the total kinetic energy of the ion in an effort

to eliminate the micromotion contribution to the total energy. To test different ways to calculate the ion temperatures, several different methods were used to calculate the velocity distributions, similarly to the ion density radial distribution:

- The average velocity over an oscillation period is used. This way the ion oscillations due to the rf field are averaged out.
- The ion velocity at a specific phase of the rf field is used. The evolution of the ion velocity relative to the phase of the trapping field is studied. The phase values of $\pi/2$,π, $3\pi/2$ and 2π are used.
- The ion velocity at the moment when the ion cloud's total kinetic energy reaches its minimum value over one oscillation period is used.
- Ion velocities at every integration step are used. This is the true velocity distribution.
- In addition to the above methods, which are identical to the methods used to calculate ion density radial distribution, a new method is added. In this method the value of the velocity used to tabulate the distribution is calculated in the following way: $v = 2\sqrt{v_c^2 + v_s^2}$,where $v_c = \sum_i v_i \cos\phi_i$, $v_s = \sum_i v_i \sin\phi_i$. The sum is calculated over all the steps i of the period so that the phase ϕ_i of the oscillation field spans the interval from 0 to 2π. This is equivalent to calculating the amplitude of the Fourier component of the ion motion at the trapping field frequency.

The radial ion number distributions have already revealed that the ions in the crystal move in unison with the trapping rf field. This feature is again exposed when the differences in the velocity distribution graphs calculated by different methods are studied. The probability distribution of the axial velocity component remains

Gaussian independent of the calculation method. The radial velocity distribution, however, shows features that correspond to the oscillatory motion. Figure 20 shows the differences in velocity distributions at low temperatures when these different calculation methods are employed. Just like the ion density radial distribution, the

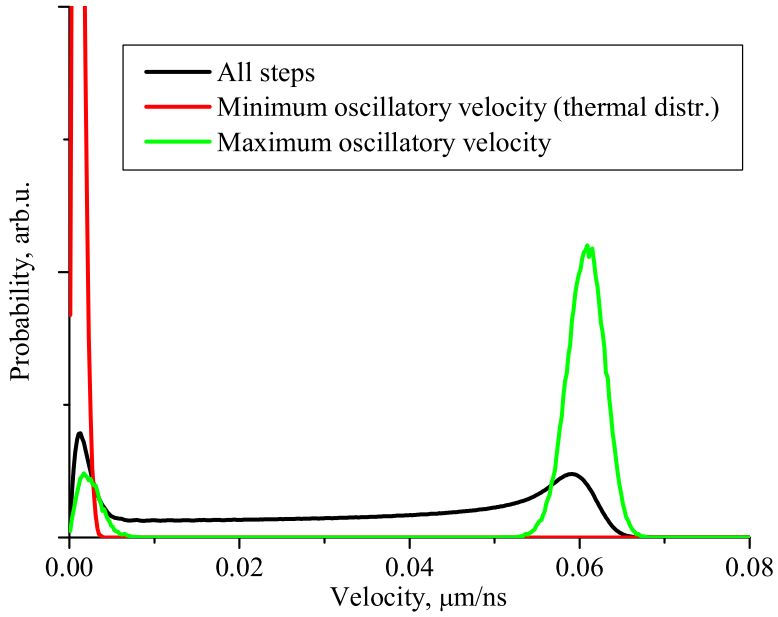

Fig. 20. The velocity distributions calculated at different phases of the oscillatory motion. Low temperatures. The top portion of the thermal (red) distribution is out of the graph scale to show more detail in the other two distributions. The linear density of ions is 340 ions/mm (68 ions in 200μm segment were used in calculation)

radial velocity distributions calculated by different methods can be separated into three groups. The first group (shown in red in Fig. 20), which is basically the Gaussian distribution corresponding to the thermal macromotion of the ions, can be obtained by either using the ion velocities averaged over the rf oscillation period, or the ion velocities at the rf phase equal to 0 and π. The second group (green) shows the maximum contribution to the velocity distribution due to the oscillatory motion

since it is calculated at the rf phases of $\pi/2$ and $3\pi/2$ when the velocity due to the rf oscillatory motion is maximized. The third graph (black) is basically the average of the other two as all the evolution steps thus all the phases are taken into account. When the oscillatory velocity is at its minimum, the velocity distribution is simply Gaussian. However, when the velocity of the oscillatory motion is at maximum, the velocity distribution is distorted. From the green graph in Fig. 20 one can see two distinct peaks in this case, one corresponds to the ions in the inner string of ions and the other to the outer shell of ions. The difference in the velocity amplitudes for each of these groups is apparent. Finally, when one considers the velocity at every step of the oscillatory motion, the radial velocity distribution spreads out more or less evenly from the minimum value to the maximum value of the oscillatory velocity, corresponding to the different phases of the oscillation. The temperature dependence of the radial velocity distributions at the maximum oscillatory velocity is shown in Fig. 21. As the temperature increases, the peaks start to spread out, showing that the thermal kinetic energy becomes comparable to the oscillatory energy.

The velocity distributions calculated at the minimum of the oscillatory energy are quite close to the theoretically predicted Gaussian distribution, an example is shown in Fig. 22. Additionally, the Gaussian fits for the axial and radial components of the velocity distributions have nearly the same width, i.e. the same temperature. At temperatures above 20K, the values obtained from the velocity distribution are not very reliable. This conclusion is reinforced by the fact that at these higher temperatures the axial velocity distribution no longer appears to be Gaussian. The reason for this distortion is that the Debye length at these temperatures exceeds $L/2$, the half length of our simulated slice. $L/2$ is the effective cutoff distance for the pair interaction in the simulation and has to be larger than the Debye length to accurately represent the physics of the problem. Longer slices, and therefore more interacting

(a)

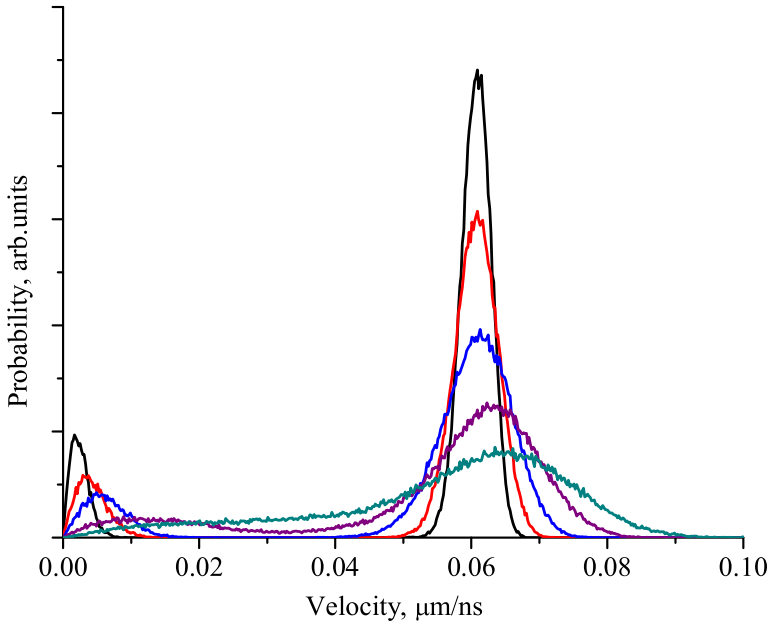

(b)

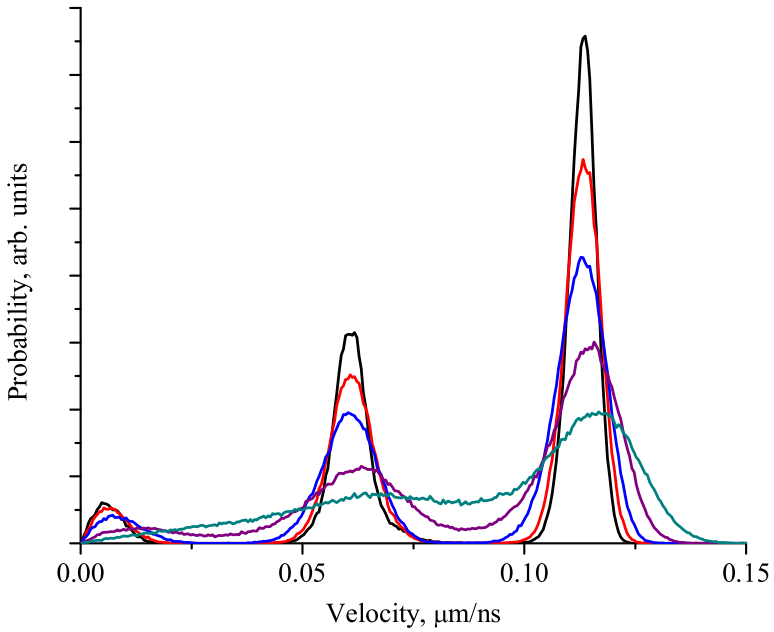

Fig. 21. The evolution of the velocity distributions with temperature (maximum oscillation velocity). (a)the linear density of ions is 340 ions/mm (68 ions in 200μm segment were used in calculation); (b) the linear density of ions is 930 ions/mm (186 ions in 200μm segment were used in calculation).

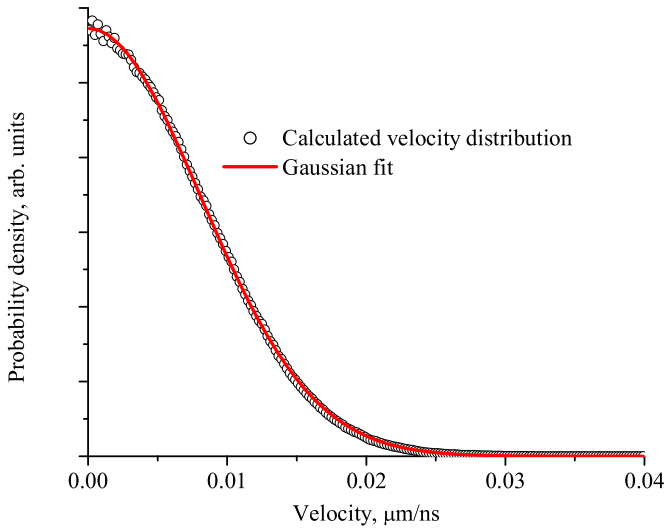

Fig. 22. An example of the ion radial velocity distribution calculated at the rf phase zero. The corresponding temperature is 190mK.

particles are needed to properly study the system at higher temperatures.

3. Evolution of the kinetic energy

To understand the thermal processes that happen during the laser cooling of the ion clouds, we have to study the evolution of the kinetic energy of these clouds. When studying the kinetic energy of the ions in the direction perpendicular to the trap axis, i.e. the *radial temperature*, one very important fact follows from the previous section. It was shown that the probability distribution of the radial velocity matches the Maxwell distribution when the phase of the rf trapping field is 0 or π, i.e. when the rf trapping potential is at its maximum. The temperature of that distribution can therefore be considered to be the temperature of the ion macromotion. Thus, by monitoring the kinetic energy of the ions when the phase of the rf field is either 0 or π, we are monitoring the evolution of the ion temperature. This convention is in

contrast with a different approach[34], where the average value of the radial velocity over an rf oscillation period was used to calculate the temperature of the ions. The temperature obtained by using the average velocity is lower than the temperature obtained by using the velocity at the minimum rf oscillatory energy by a factor of $2-3$. This difference can be explained by the observation that by averaging the velocity over an oscillation period one averages out not only the micromotion, but also all other processes which happen on the time scale which is shorter than the period of the rf oscillation. An example of such a process would be ion-ion collisions. The kinetic energy of the ions associated with the motion along the trap axis can be evaluated at any moment of time because there is no micromotion along the axis. However for consistency both radial and axial temperatures were evaluated at the same phase ($\phi = 0$) of the rf trapping field.

It is illustrative to first study the evolution of the kinetic energy on the scale of a few oscillation periods. An example of such evolution of the radial temperature is shown in Fig. 23. One can see that the evolution of both radial and axial temperatures exhibits a quasi-periodic oscillations. If one measures the frequency of these oscillations, the value is close to twice the secular oscillation frequency (see Eq.(2.11)). The factor of two is due to the temperature being proportional to the square of the velocity. Since the secular oscillation of each ion is independent, and the phase of secular oscillation varies randomly from ion to ion, this oscillations should average out over many ions. However due to the limited number of ions (N=68 in the figure presented) the averaging is not perfect. The temperature fluctuations that are created due to this effect are consistent with the general law of thermodynamic fluctuations ($\frac{\Delta T}{T} = 1/\sqrt{N}$). One can also verify that along with oscillations of the kinetic energy, the matching oscillations are present in the quadrupole moments of the ion cloud's radial density distributions.

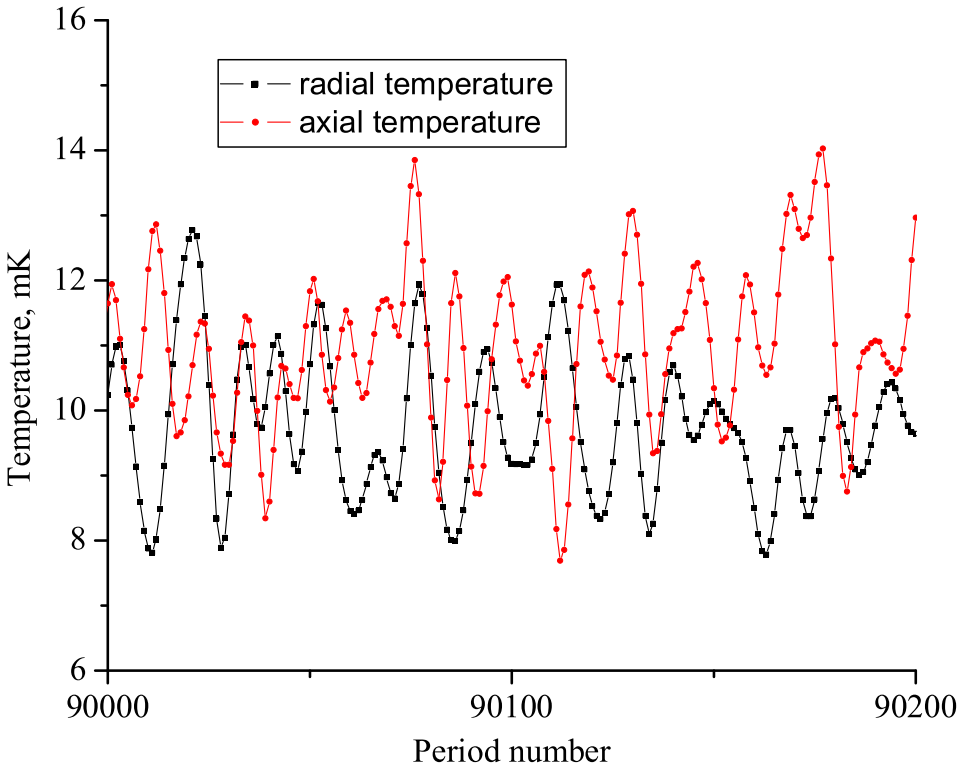

Fig. 23. The quasiperiodic fluctuations in the radial and axial temperature ($N = 68$, $L = 200\mu m$).

Ultimately, the heating rate of the ion cloud is obtained by monitoring the evolution of kinetic energy. To do that the cloud is first thermalized to a given temperature, i.e. the ions are allowed to evolve for $\approx 50,000 - 100,000$ rf oscillation periods. The kinetic energy of the ion cloud is set to the desired value after each period by scaling the velocities of the ions. Additionally, the ion velocities are "scrambled" every 1000 periods. The "scrambling" consists of randomly changing the direction of the radial velocities of the ions while maintaining their magnitudes. This scrambling is done to remove possible traces of the correlation between ions that are present at lower temperatures. After the thermalization, the ions are then allowed to evolve without any external adjustments to the ion velocities for about $50,000$ rf oscillation periods.

An example of the evolution of the ion clouds' kinetic energy is given in Fig. 24. The

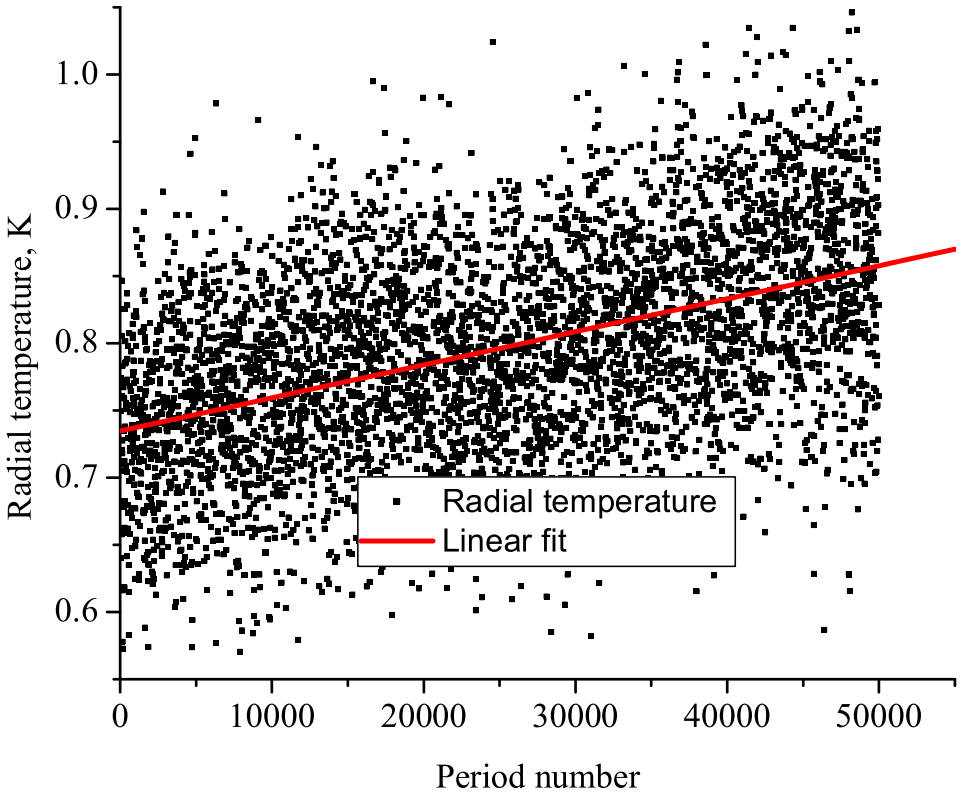

Fig. 24. An example of change in temperature due to rf heating. Shown is the radial kinetic energy of the ion cloud with parameters $N = 68$, $L = 200\mu$m,$V_0 = 100$V.

slope of the linear fit gives the rate of the rf heating. The values of the rf heating rates were obtained under different trapping parameters and temperatures. The dependence of the rf heating rates on the ion cloud temperatures for two rf trapping voltages is shown in Fig. 25. The graph for $V_0 = 100$V is extended into larger temperature values by keeping the same linear density of the ions, but extending the length of the studied slice from $L = 200\mu$m to $L = 600\mu$m, thus increasing the cutoff length of the Coulomb interactions. The rf heating rate was calculated for both values of L at the temperature $T = 5$K to verify that they produce the same heating rate. The

(a)

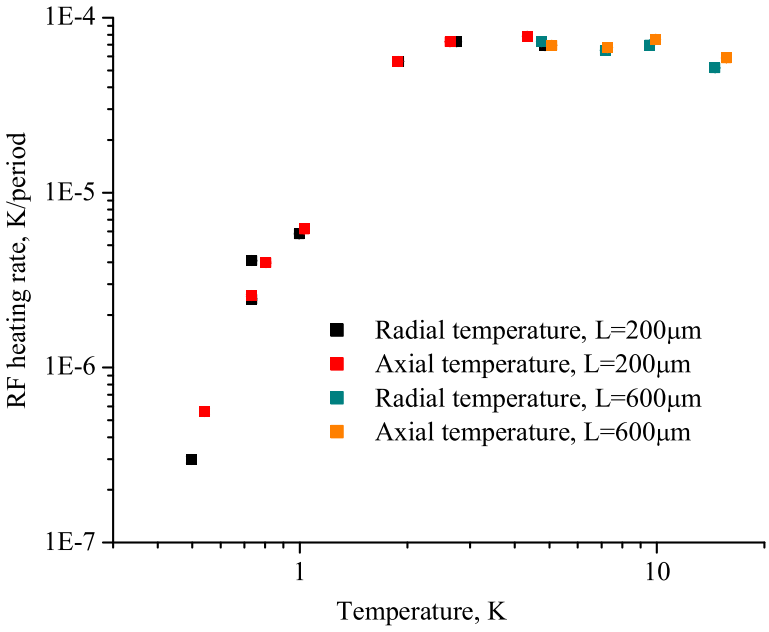

(b)

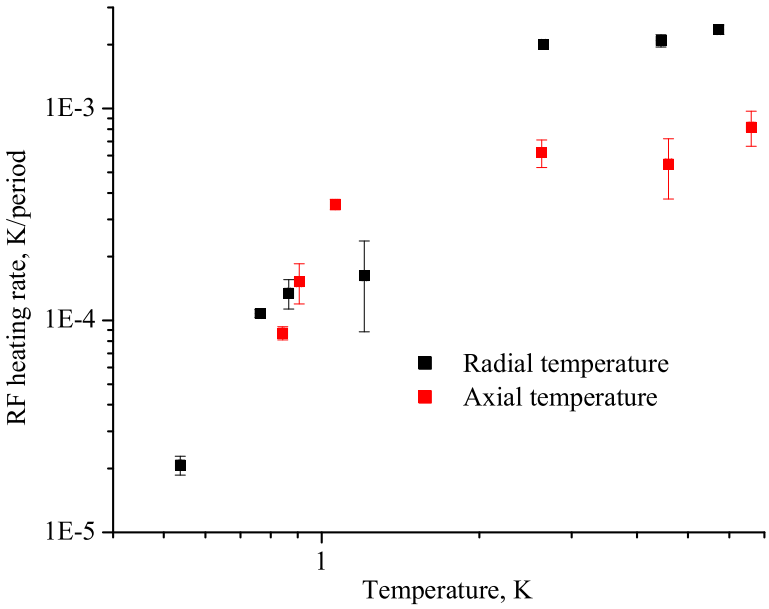

Fig. 25. The rf heating rate as a function of temperature. (a) the trapping voltage amplitude $V_0 = 100$V; (b) the trapping voltage amplitude $V_0 = 200$V.

graphs only cover the ion cloud temperatures beginning from approximately 0.5K. This is because at lower temperatures, down to a fraction of a millikelvin, there is no detectable rf heating present. This is a very important fact. It means that it is possible in principle to store the ion clouds in the trap at ultralow temperatures for extended periods of time without involving laser cooling. Of course in a real rf trap there are other heating mechanisms present, that will gradually heat the ions up, such as the thermal current noise in the trap rods, the rf heating due to imperfections in quadratic trapping potential, collisions with background gas, etc. As the temperature approaches 1K the rf heating starts to increase rapidly. If one is to plot the rf heating rates in the neighborhood of 1K, the rf heating rate increases as the 5th power of temperature. At around 5K the rf heating rate reaches what appears to be a plateau. It stays at approximately the same value in the temperature interval up to 15K, while it does appear to decrease slightly. The temperatures above 15K were not studied as they require more computing power than I have at my disposal at the moment. Another interesting phenomenon is exhibited in the plateau region of the rf heating rate curve in Fig. 25(b). The rf heating rates of the radial and the axial degrees of freedom start to differ significantly from each other. This is due to the fact that at this higher trapping voltage the maximum rf heating rate is so high that the heating process cannot be considered as adiabatic. The rate with which the kinetic energy is being added to the radial motion is faster than the rate with which it transfers into the axial motion.

The change of the rf heating rates with the trapping voltage is shown in Fig. 26. Three different temperatures of the ion cloud (T = 0.5K,1K,5K) are chosen to study how the heating rates behave in three different regions of the heating curve: the appearance of the rf heating at 0.5K, the sharp rise in the heating rate at 1K, and the plateau at 5K. The linear fits shown in the graph demonstrate the power

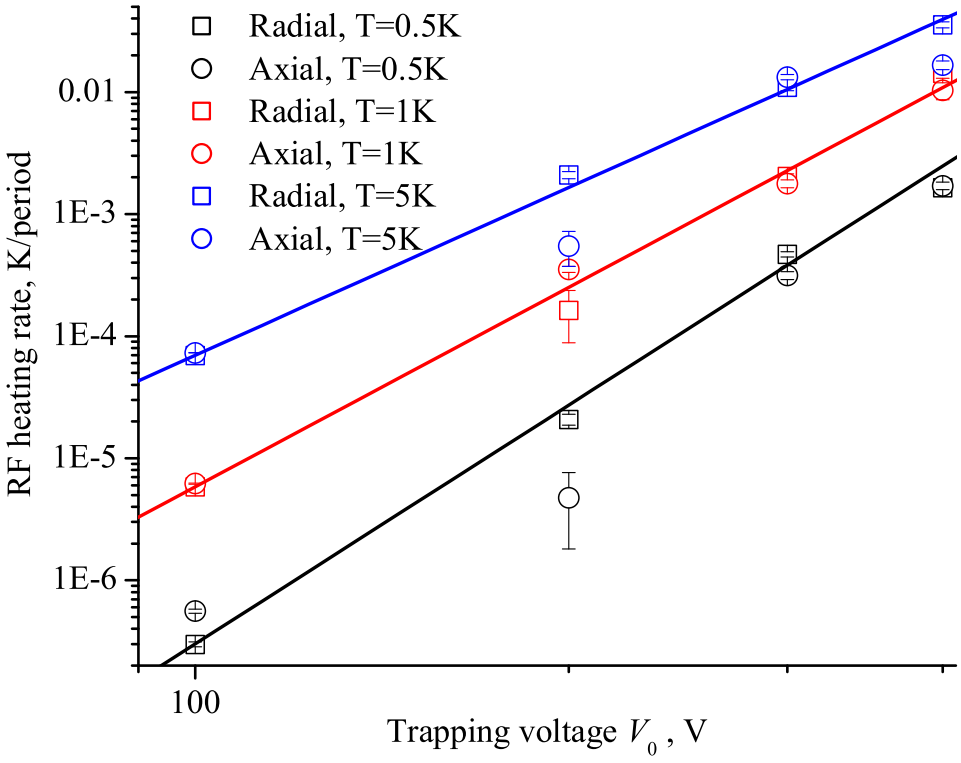

Fig. 26. Change of rf heating rates with trapping voltage.

law dependence of the heating rate on the rf voltage. Apparently, as the temperature increases, the slope of the power law curve decreases. The power is 6.5 for T=0.5K, 5.5 for T=1K, and 4.5 for T=5K.

To obtain the insight into the influence of the size of the ion cloud on the rf heating, a few simulations were also performed with a larger number of particles $N = 186$. In particular, the heating rates for the ion clouds with trapping voltage $V_0 = 100$V for $N = 68$ and $N = 186$ were calculated. The heating rate for a given number N is taken as the average of radial and axial heating rates. Then the ratio of the heating rates for $N = 186$ and $N = 68$ was calculated. It is equal to 2.1 at $T = 0.5$K and 1.7 at $T = 1$K. That is a very interesting number, since it is quite

different from what one would expect. When the number of ions is increased from 68 to 186, the radius of the ion cloud is doubled. Since the amplitude of the rf trapping field increases as the square of the distance from the trap axis, the majority of the additional ions are exposed to the rf fields of 4 times the amplitude as compared to the ions in the ion cloud with 68 ions. Thus the energy of the micromotion in the ion cloud with $N = 186$ is 8 times larger as compared to the cloud with $N = 68$. Yet the heating rate is only increased by a factor of two. While I cannot explain this interesting behavior it is most likely the reason behind the recent advances in achieving extremely large multi-layered ion crystals.

D. HEATING DUE TO RANDOM PHASE FLUCTUATIONS

The experiments have shown that the minimum temperature that can be achieved in the ion cloud varies a lot with the number of ions, the trapping potential, and the laser power. However, the rf heating is not present, or at least was not detectable, for ion cloud temperatures below 0.5K. Thus the mechanism responsible for setting the low limit on the ion cloud temperature is not the rf heating. In order to better understand the limiting factors in the low temperature region, here I attempt to study other heating mechanisms by generalizing them as the random perturbation in the ion motion.

The simulation is set up in the following way. The initial ion distribution at a given temperature is generated as described earlier. Then the ions are allowed to move in the oscillating rf field but are being subjected to random "kicks" to their velocities. At each integration step every ion has a probability of experiencing this "kick". The kick itself is done in the following way. A randomly oriented velocity vector of a preset amplitude is added to the ion's velocity. The amplitude of the kick

velocity, $|\vec{\Delta v}|$, is one of the parameters of this random process, the other one is the frequency f of the kicks. The ion velocity magnitude is then adjusted so that it has the same value as it did before the kick. The magnitude of the kick relative to the average ion velocity in the cloud determines the average deflection angle due to the kick. Since this process conserves the energy, the term "kick" is somewhat misleading. A more appropriate description of this process would be velocity deflection.

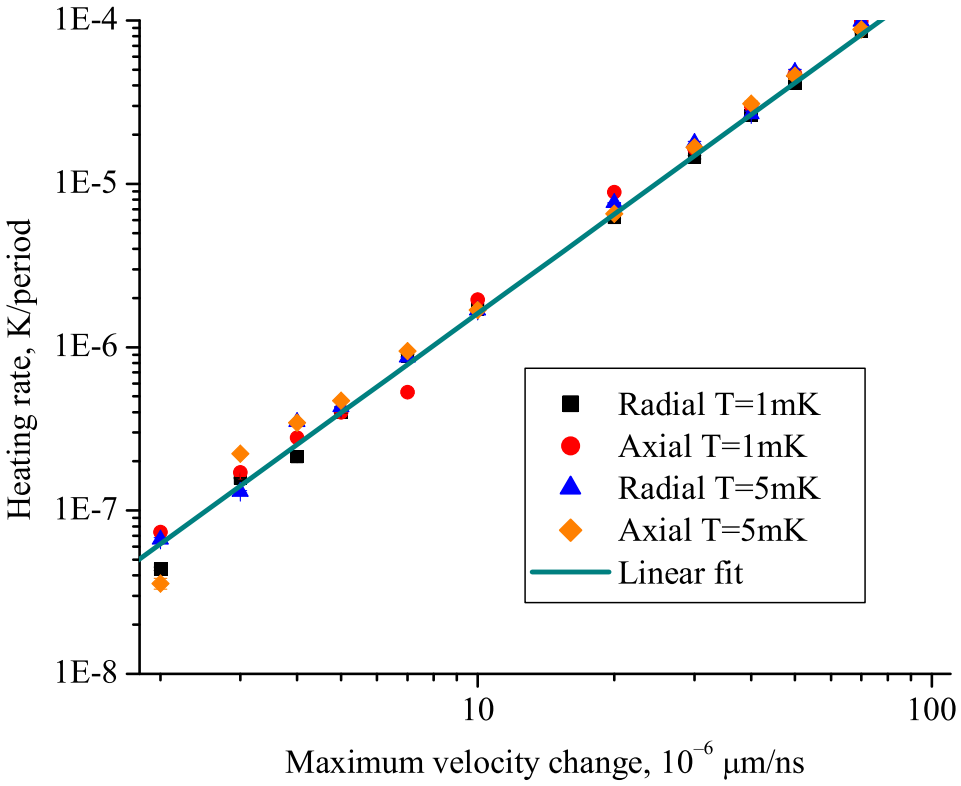

Fig. 27. Heating due to the random deflections of the velocity. The frequency of the deflections is 20 per ion per rf period.

Figure 27 shows the dependence of the resulting heating rate due to the random kicks to the velocity. The linear fit on the log-log graph shown in the figure quite accurately matches the quadratic dependence of the heating rate on the magnitude of

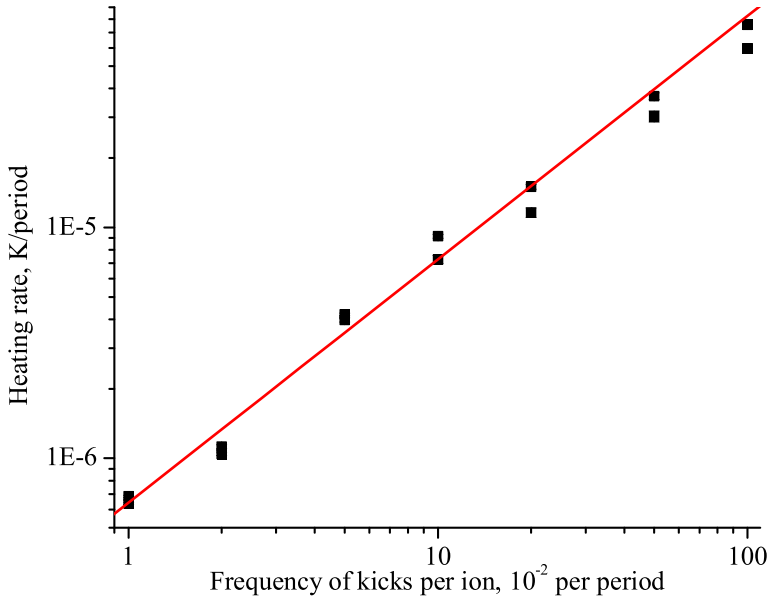

Fig. 28. Heating due to the random deflections of the velocity, frequency dependence. The amplitude of each "kick" is $2\times10^{-5}\mu$m/ns.

the random adjustments to the velocity. Another fact that follows from the presented data is that the heating rate does not depend on the initial temperature of the ions. One can see that the heating rates for the two different temperature values as shown in Fig. 27 are very close to each other. The dependence of the heating rate on the frequency of the random deflections is presented in Fig. 28. The slope of the linear fit on the log-log graph is close to one (1.05) which shows that the heating rate depends linearly on the rate of the velocity perturbations. This and the quadratic dependence of the heating rate on the magnitude of the kick *exactly* match the properties of the usual random walk process in the momentum space. Thus it is important to point out that the random process described here is *not* the familiar random walk, since only the direction of the velocity is changed. If no rf field and coulomb interactions are present, this random deflection process will not change the temperature of the system.

Another property that separates the random deflection process from the random walk is the magnitude of the heating rate. The heating rate for both processes can be written as

$$\frac{\Delta K}{\Delta t} = A\frac{m\left|\vec{\Delta v}\right|^2}{2}f, \tag{4.8}$$

where $\frac{\Delta K}{\Delta t}$ is the rate of increase in kinetic energy(heating rate), m is the mass of the particle, f is the frequency of the random deflections, and $|\vec{\Delta v}|$ is the magnitude of each "kick". The difference is in the value of the coefficient A. For the process of random walk in the momentum space the coefficient $A = 1$. In the case of this simulation the coefficient $A = 0.87$ for $V_0 = 100$V, $N = 68$, $L = 200\mu$m. The simulation was also performed to see if this heating rate is affected by the timing of the perturbations relative to the rf phase. The results show that there is no detectable dependence of the heating rate on the time of the "kicks".

This heating effect could contribute to limiting the lowest temperature that can be achieved by laser cooling of the ions in the rf trap. The Doppler cooling limit exists due to the presence of the recoil heating during the scattering of the photons. The scattering of photons by the ions stored in the trap is accompanied by an *additional* heating process due to the random change in the velocity direction as described above. The heating rates due to these two processes would provide about equal contributions to the total heating rate, if the interaction with photons is approximated as instantaneous as it is done in this simulation. This means that the heating rate due to the scattering of the photons by the ions stored in the trap is at least twice that of the free ions/atoms. The average lifetime of the Magnesium ion in the excited state (which is the time that passes between the absorption and re-emission of the photon) is $\approx$ 4ns, and the rf oscillation period is $\approx$ 136ns. Therefore the time that the ion spends in the excited state can have influence on the heating rate. Further

investigation is needed to study the effects of the time delay between the absorption and re-emission of the photon on the heating rate.

E. SYMPATHETIC COOLING

Simulations of the sympathetic cooling of the ions inside the trap were also performed. Two ion species, one of mass $m_1 = 24$a.u. (corresponds to Magnesium) and the other $m_2 = 720$a.u. (corresponds to the fullerene molecule). The same number of ions (100) was used for each species. The amplitude of the rf trapping voltage was set to $V_0 = 400$V, the same as used in the experiment. The axial temperature of the Mg^+ ions was kept constant to simulate the effect of laser cooling. This is achieved by rescaling the velocities after each oscillation period. Since the sympathetic cooling experiment has shown that the axial temperature of the Mg^+ ions is around 5K, this value was used in the simulation. The fullerene ions started out with a temperature of 100K in both radial and axial directions. After 10^6 oscillation periods the radial temperatures of both the Magnesium and fullerene ions were equalized at 10K. The axial temperature of the fullerene ions has reached 8K. Figure 29 shows the evolution of the axial temperature of the fullerene ions over the course of the simulation. The temperature of the fullerene ions appears to decrease exponentially. The time constant corresponding to this exponential decay doubles from 85ms in the beginning of the simulation to 170ms at the end of it. This result shows that despite a huge disparity in the masses of the ions, they can reach approximately same axial temperature.

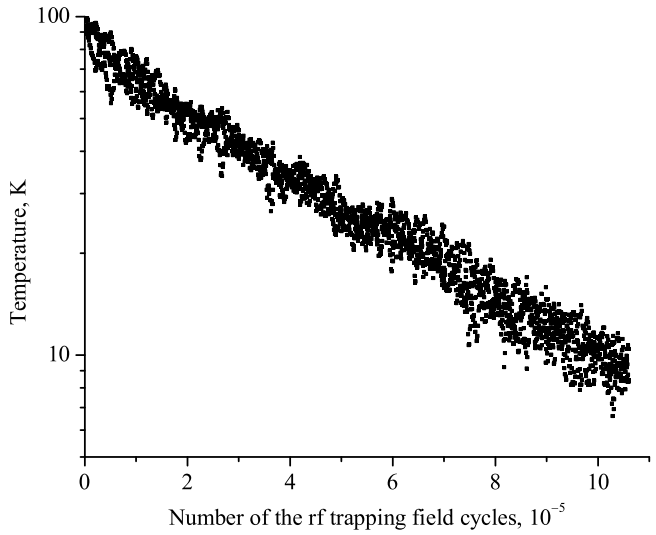

Fig. 29. Time evolution of the axial temperature of the fullerene ions when sympathetically cooled by Mg^+ ions. The axial temperature of the Mg^+ ions is maintained at 5K.

CHAPTER V

THERMODYNAMICS OF LASER COOLING

This chapter provides the theoretical background in laser cooling and plasma thermodynamics. The information given here is useful in interpreting the results of the molecular dynamics simulations and the experimental data.

First, the properties of the fluorescence lineshapes and laser cooling efficiency at different temperatures are described. Second, a way to calculate the radial ion density of the infinitely long plasma column in the harmonic trapping well is given. The properties of the radial ion density distributions are discussed. Finally, the Coulomb collision process is described and a method to use the Coulomb collisions to obtain rf heating rates is given. The rate equations are introduced that describe the increase of the kinetic energy in the ion cloud due to the rf heating and the decrease due to the laser cooling. The balance of these two processes is reached at some equilibrium temperature. The dependence of this temperature on the laser detuning determines the fluorescence lineshapes.

A. LASER COOLING

1. Voigt lineshape

Let us consider a collection of ions at temperature T. The velocity distribution along a chosen direction is then described by a Gaussian:

$$P(v)dv = \sqrt{\frac{m}{2\pi kT}} \exp\left[-\frac{mv^2}{2kT}\right] dv \tag{5.1}$$

where $P(v)dv$ is the probability of an ion to have its velocity in the interval v to $v + dv$. The absorption/fluorescence profile of a chosen transition for any of these

ions is described by normalized Lorentzian lineshape $g_L(\omega)$:

$$g_L(\omega) = \frac{\gamma}{\pi}\frac{1}{\gamma^2 + (\omega_0 - \omega)^2}, \tag{5.2}$$

where ω_0 is the transition frequency and γ is the half width at half maximum (HWHM) of the profile.

The absorption/fluorescence lineshape of such an ensemble of ions is a sum of all of the individual ions' profiles:

$$\begin{aligned} g(\omega) &= \int g_L(\omega; v) \times P(v) dv \\ &= \int_{-\infty}^{+\infty} \frac{\gamma}{\pi}\frac{1}{\gamma^2 + (\omega_0 - (1 - \frac{v}{c})\omega)^2} \times \sqrt{\frac{m}{2\pi kT}} \exp\left[-\frac{mv^2}{2kT}\right] dv, \end{aligned} \tag{5.3}$$

where $g_L(\omega; v)$ is the profile of an ion that has velocity v along the direction of light propagation. The expression (5.3) takes into account that the light frequency seen by the ion is Doppler shifted:

$$g_L(\omega; v) = \frac{\gamma}{\pi}\frac{1}{\gamma^2 + (\omega_0 - (1 - \frac{v}{c})\omega)^2}, \tag{5.4}$$

with ω as the light frequency in the laboratory frame. To integrate Eq.(5.3) we will make a variable substitution $\xi = \sqrt{\frac{m}{2kT}}v$. The integral then becomes

$$g(\omega) = \int_{-\infty}^{+\infty} \frac{\gamma}{\pi}\frac{1}{\gamma^2 + \left(\omega_0 - \left(1 - \frac{\xi}{c}\sqrt{\frac{2kT}{m}}\right)\omega\right)^2} \times \frac{1}{\sqrt{\pi}} \exp\left[-\xi^2\right] d\xi \tag{5.5}$$

$$= \int_{-\infty}^{+\infty} \frac{\gamma}{\pi}\frac{mc^2}{2kT\omega^2}\frac{1}{\Gamma^2 + (\Delta - \xi)^2} \times \frac{1}{\sqrt{\pi}} \exp\left[-\xi^2\right] d\xi, \tag{5.6}$$

where

$$\Gamma = \gamma \frac{c}{\omega} \sqrt{\frac{m}{2kT}} \tag{5.7}$$

$$\Delta = (\omega_0 - \omega) \frac{c}{\omega} \sqrt{\frac{m}{2kT}}. \tag{5.8}$$

When the natural linewidth of the transition is negligible, i.e. $\gamma \to 0$, and $g_L(\omega) \to \delta(\omega_0 - (1 - \frac{v}{c})\omega)$, then the normalized lineshape $g(\omega)$ becomes:

$$g(\omega) = \sqrt{\frac{mc^2}{2\pi kT\omega^2}} \exp\left[-\frac{mc^2(\omega - \omega_0)^2}{2kT\omega^2}\right]. \tag{5.9}$$

Most of the time this lineshape can be approximated by a Gaussian function and is called the Doppler lineshape:

$$g_D(\omega) = \sqrt{\frac{mc^2}{2\pi kT\omega_0^2}} \exp\left[-\frac{mc^2(\omega - \omega_0)^2}{2kT\omega_0^2}\right] = \frac{1}{\Delta_D}\sqrt{\frac{\log 2}{\pi}} \exp\left[-\log 2 \frac{(\omega - \omega_0)^2}{\Delta_D^2}\right], \tag{5.10}$$

where the HWHM of the Doppler lineshape Δ_D is:

$$\Delta_D = \sqrt{\log 2}\sqrt{\frac{2kT\omega_0^2}{mc^2}}. \tag{5.11}$$

Also, using the notation for HWHM of a Lorentzian $\Delta_L = \gamma$, we can write

$$\Gamma = \frac{\Delta_L}{\Delta_D}\sqrt{\log 2}, \tag{5.12}$$

$$\Delta = \frac{\omega - \omega_0}{\Delta_D}\sqrt{\log 2}. \tag{5.13}$$

In general, however, the lineshape is neither Lorentzian nor Gaussian but a mixture of both, called the Voigt lineshape:

$$g_V(\omega) = \sqrt{\frac{\log 2}{\pi}} \frac{1}{\Delta_D} \int_{-\infty}^{+\infty} \frac{1}{\pi} \frac{\Gamma e^{-\xi^2 d\xi}}{\Gamma^2 + (\xi - \Delta)^2} = \sqrt{\frac{\log 2}{\pi}} \frac{1}{\Delta_D} \Re[w(\Delta + i\Gamma)], \qquad (5.14)$$

where $w(z)$ is Faddeeva function of a complex argument. This function gives the Lorentzian lineshape when $\Gamma \gg 1$, and Gaussian lineshape when $\Gamma \ll 1$. Numerical HWHM values calculated using expression (5.14) were used to estimate the temperature of the ions from their fluorescence lineshape.

2. Cooling efficiency

At a given temperature T, the velocity distribution of the ions along the direction of the laser beam is Gaussian as given by Eq.(5.1). Let us consider an ion that initially has a velocity component v, therefore the momentum mv, along the axis of the laser beam. All the photons in the laser beam have the same momentum $\hbar k$ along this axis. After absorbing a photon the new momentum of the ion becomes $mv + \hbar k$. The re-emission of the photon on the average doesn't change the momentum of the ion since the re-emitted photon can go in any direction with equal probability. Thus the average change of momentum of the ion in a single scattering process is $\hbar k$. The change in kinetic energy of the ion with velocity v in a single scattering is then

$$\Delta K(v) = \frac{m(v + \hbar k/m)^2}{2} - \frac{mv^2}{2} \approx v\hbar k. \qquad (5.15)$$

The more accurate approach [39] accounts for the so-called recoil shift in the process of absorption and re-emission of the photon. Including the change in the photon energy due to the recoil, the more accurate expression of the change in kinetic energy of the ion in a single scattering process is:

$$\Delta K(v) = v\hbar k + 2R = v\hbar k + \frac{(\hbar k)^2}{m}. \tag{5.16}$$

Assuming the lineshape of the transition is Lorentzian as in Eq.(5.4), then the probability of an ion, with velocity component v along the laser beam axis, to absorb and scatter a photon during time interval dt is

$$P_{abs} = A g_L(\omega; v) dt, \tag{5.17}$$

where A is a coefficient that depends on the intensity of the incoming radiation and the properties of the transition. In the unsaturated regime A is proportional to the field strength of the light, or the Rabi frequency.

The average change in total kinetic energy over time interval dt of the ion cloud that has Gaussian velocity distribution is

$$\begin{aligned} \langle \Delta K \rangle &= \int dv P(v) \Delta K(v) P_{abs}(v) \qquad (5.18) \\ &= \int dv \sqrt{\frac{m}{2\pi kT}} \exp\left[-\frac{mv^2}{2kT}\right] \left(\hbar\frac{\omega}{c}v + \frac{\hbar^2\omega^2}{mc^2}\right) A\frac{\gamma}{\pi}\frac{1}{\gamma^2 + (\omega(1-\frac{v}{c}) - \omega_0)^2}. \end{aligned}$$

Substitution $\xi = \sqrt{\frac{m}{2kT}}v$ yields

$$\begin{aligned} \langle \Delta K \rangle &= \int d\xi \sqrt{\frac{1}{\pi}} \exp\left[-\xi^2\right] \left(\hbar\frac{\omega}{c}\sqrt{\frac{2kT}{m}}\xi + \frac{\hbar^2\omega^2}{mc^2}\right) A\frac{\Gamma}{\pi}\frac{c}{\omega}\sqrt{\frac{m}{2kT}}\frac{1}{\Gamma^2 + (\Delta - \xi)^2} \\ &= \int \xi d\xi \sqrt{\frac{1}{\pi}} \exp\left[-\xi^2\right] \hbar A\frac{\Gamma}{\pi}\frac{1}{\Gamma^2 + (\Delta - \xi)^2} \\ &\quad + \int d\xi \sqrt{\frac{1}{\pi}} \exp\left[-\xi^2\right] \frac{\log 2}{\Delta_D}\frac{\Gamma}{\pi}\frac{1}{\Gamma^2 + (\Delta - \xi)^2} A\frac{\hbar^2\omega^2}{mc^2}. \qquad (5.19) \end{aligned}$$

It is easy to see that the second integral in the above expression is proportional to the Voigt lineshape, therefore the second term that describes recoil heating is equal

to $A\frac{\hbar^2\omega^2}{mc^2}g_V(\omega)$. The first term in the expression can be integrated:

$$\begin{aligned} & \int \xi d\xi \sqrt{\frac{1}{\pi}} \exp\left[-\xi^2\right] \hbar A \frac{\Gamma}{\pi} \frac{1}{\Gamma^2 + (\Delta - \xi)^2} \\ = \; & \frac{A\hbar\Gamma}{\sqrt{\pi}} \left(\frac{\Delta}{\Gamma} \Re[w(\Delta + i\Gamma)] - \Im[w(\Delta + i\Gamma)] \right) \qquad (5.20) \\ = \; & \frac{A\hbar}{\sqrt{\pi}} \Re\left[(\Delta + i\Gamma) w(\Delta + i\Gamma) \right], \qquad (5.21) \end{aligned}$$

where $w(z)$ is again a Faddeeva function of a complex argument. The total cooling rate can be rewritten as:

$$\left\langle \frac{\Delta K}{\Delta t} \right\rangle = \frac{\hbar A}{\sqrt{\pi}} \Re\left[(\Delta + \alpha\Gamma + i\Gamma) w(\Delta + i\Gamma) \right], \qquad (5.22)$$

where $\alpha = \frac{\hbar\omega^2}{mc^2\gamma}$ is the characteristic value of the transition which determines at which temperatures (what stage on the Doppler to Lorentzian lineshape) the recoil energy becomes relevant. The larger the value of α, the more this threshold is moved towards the Doppler region.

The expressions derived above can help to answer an interesting question: how far from resonance should the laser be red detuned in order to achieve the most efficient laser cooling (maximum kinetic energy taken from the ions per unit time). The results of calculations using the above expressions are shown in Fig. 30. The main conclusion to draw from the figure is that cooling is the most efficient at detunings slightly less (60% for Lorentzian and 85% for Gaussian lineshapes) than the HWHM of the fluorescence/absorption line. It is noted that the HWHM increases with temperature, therefore the laser detuning required for optimal cooling also increases with temperature.

A rough estimate can be made to evaluate the number of photons needed to cool down the Mg^+ ion from 100K to 1mK. Assuming that the laser detuning is

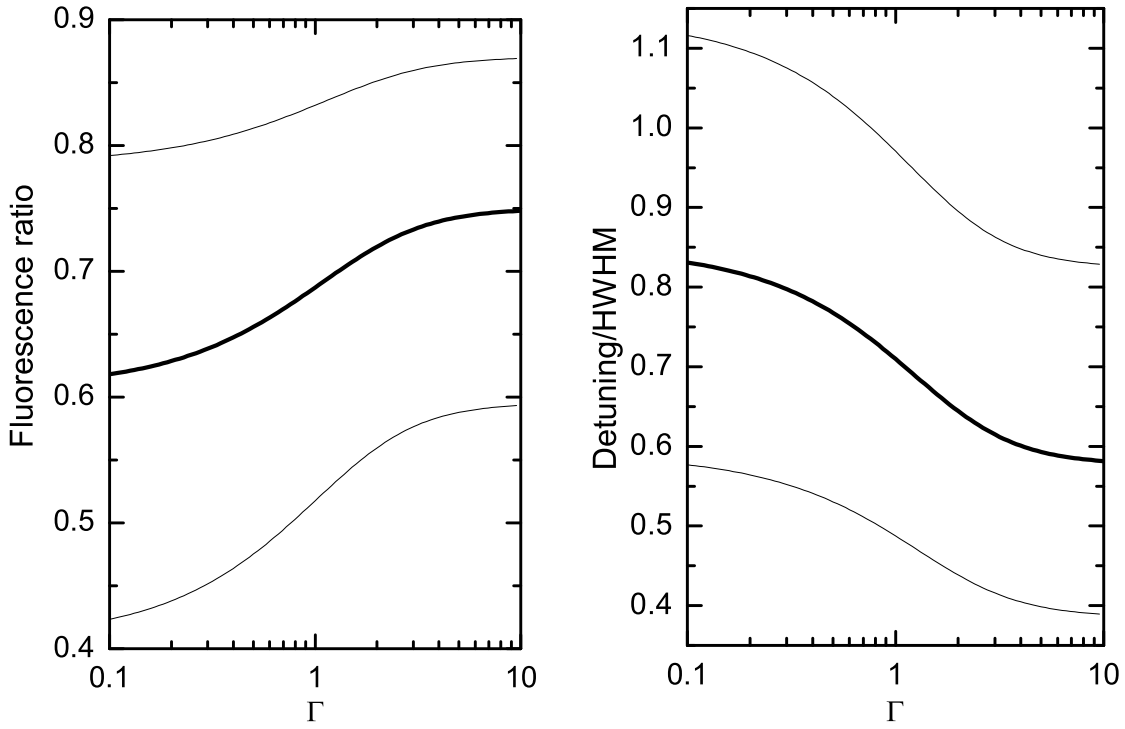

(a) (b)

Fig. 30. Optimum cooling efficiency for different lineshapes described by Γ. Bold line traces the position of optimal detuning, the thin lines indicate the boundaries in which the cooling is within 90% of optimal. a)The vertical axis represents the ratio of the fluorescence intensity at the cooling detuning to the maximum fluorescence. b) The vertical axis shows the detuning in the units of HWHM

kept constant at the value equal to half natural linewidth of the cooling transition, the total number of photons needed is $\approx 50,000$. This number can be significantly reduced if the laser detuning is not kept constant but is adjusted as the temperature of the ion changes.

B. PLASMA THERMODYNAMICS

1. Ion clouds stored in a trap

In order to describe the thermodynamics of laser cooling, we need to have a suitable thermodynamical description of the ion clouds stored in the trap. The well known Mathieu equations describe the motion of a single ion in a quadrupole oscillating potential of the ion trap. In reality, however, there are more than just a single ion stored in the trap. It is important to know how the stored ions interact with each other and what are the effects on the trapping.

It has been shown[40] that in thermodynamic equilibrium the ion density is given by the following expression (Boltzmann distribution):

$$n(r) = N\frac{exp\left[-\frac{e\Phi(r)}{kT}\right]}{\int dV exp\left[-\frac{e\Phi(r)}{kT}\right]}, \tag{5.23}$$

where $\Phi(r)$ is the total electric potential at the distance r from the center of the trap. It consists of two contributions:

$$\Phi(r) = U(r) + \phi(r). \tag{5.24}$$

In the above equation $U(r)$ is the external harmonic potential due to the rf trapping field:

$$U(x, y, z) = U(r) = \frac{D}{r_0^2}r^2 \tag{5.25}$$

where r_0 is the radius of the trapping region, D is the depth of the trapping potential and r is the distance from the center of the trap. $\phi(r)$ is the mean field created by the ions themselves. Thus expression (5.23) is the self consistent equation that determines the ion density distribution. Along with the Poisson equation that relates

the charge density and the electric potential. The Poisson equation in this case reads:

$$\nabla^2\phi = -\frac{en(r)}{\epsilon_0}. \tag{5.26}$$

With the convenient introduction of the following function [40, 35]:

$$\psi(r) = -\frac{e}{kT}\left[\Phi(r) - \Phi(0)\right], \tag{5.27}$$

the expression for density distribution (5.23) becomes

$$n(r) = n_0 exp\left[\psi(r)\right] \tag{5.28}$$

where n_0 is the ion density at the origin. Then the Poisson equation (5.26) can be written as

$$\begin{aligned} \nabla^2\psi &= -\tfrac{e}{kT}\left[\nabla^2\phi + \nabla^2 U\right] \\ &= \tfrac{e^2 n_0}{\epsilon_0 kT} exp\left[\psi\right] - \tfrac{4e^2 D}{kTr_0^2} \\ &= \tfrac{1}{\lambda_D^2}\left[exp(\psi) - \tfrac{4\epsilon_0 D}{en_0 r_0^2}\right], \end{aligned} \tag{5.29}$$

where

$$\lambda_D = \sqrt{\epsilon_0 kT/e^2 n_0} \tag{5.30}$$

is the Debye length. By introducing the scaled distance $\xi = r/\lambda_D$ and a dimensionless parameter γ,

$$\gamma = \frac{4D\epsilon_0}{en_0 r_0^2} - 1, \tag{5.31}$$

equation (5.29) becomes:

$$\left[\frac{1}{\xi}\frac{d}{d\xi}\xi\frac{d}{d\xi}\right]\psi = e^{\psi} - 1 - \gamma. \tag{5.32}$$

This equation is a nonlinear differential equation and has to be solved numerically. It has been shown[41] that the solution is bound only for $\gamma > 0$. This condition establishes the maximum possible number density for the trapped ions for a given depth of the trapping potential well and the diameter of the trap:

$$n_0 < \max(n_0) = \frac{4D\epsilon_0}{er_0^2} \tag{5.33}$$

To obtain the shapes of the density distributions, and other properties of the ion clouds, we will have to solve this equation numerically. It helps to transform this equation in order to simplify the use of library integration routines. Introducing two functions $Y_1(r) = \xi\frac{d}{d\xi}\psi(r)$ and $Y_2(r) = \psi(r)$ we can rewrite Eq.(5.32) as a system of two first order differential equations:

$$\begin{cases} Y_1' &= \xi\left(e^{Y_2} - 1 - \gamma\right) \\ Y_2' &= Y_1/\xi. \end{cases} \tag{5.34}$$

Since the initial conditions on ψ demand $\psi'(0) = \psi(0) = 0$, we can deduce that the initial conditions on our functions of interest are $Y_1(0) = 0$ and $Y_2(0) = 0$. It also helps to note that asymptotically the solution of the system of the two equations must satisfy $Y_1'(0) = Y_2'(0) = 0$. We will also introduce two more functions into the system of the equations $Y_3(\xi)$, proportional to the linear density of ions enclosed inside radius ξ, and $Y_4(\xi)$, the average square radius of the ion positions inside the radius ξ:

$$Y_3(\xi) = \int_0^{\xi} d(\pi\xi'^2)\frac{n(\xi')}{n_0} = \int_0^{\xi} d\xi' 2\pi\xi' e^{Y_2(\xi')} \tag{5.35}$$

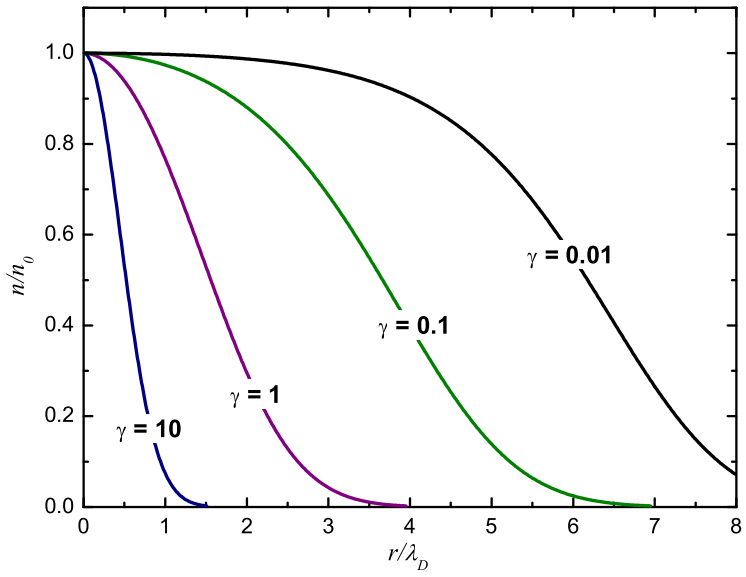

Fig. 31. Density distributions for different values of parameter γ.

$$Y_4(\xi) \;=\; \int_0^{\xi} d(\pi\xi'^2)\xi'^2\frac{n(\xi')}{n_0} = \int_0^{\xi} d\xi' 2\pi\xi'^3 e^{Y_2(\xi')} \tag{5.36}$$

Therefore $Y_3' = 2\pi e^{Y_2}\xi$ and $Y_4' = 2\pi e^{Y_2}\xi^3$. These functions provide important information about the ion distribution, namely $N = Y_3(\infty)\lambda_D^2 n_0 L$, where N is the total number of trapped ions, L is the length of the trap, and $\langle r^2\rangle = \lambda_D^2\frac{Y_4(\infty)}{Y_3(\infty)}$. The initial conditions for these functions are $Y_3(0) = 0$ and $Y_4(0) = 0$.

There is an important relationship between the parameter γ and the total number of ions. The number of ions should remain constant:

$$N = const = Y_3(\infty)\lambda_D^2 n_0 L = Y_3(\infty)\frac{\epsilon_0 kT}{e^2 n_0} n_0 L = Y_3(\infty)\frac{\epsilon_0 kTL}{e^2}. \tag{5.37}$$

Since the value of $Y_3(\infty)$ is determined only by the value of γ this establishes a direct relationship between the values of γ and the temperature for a given number of trapped particles N. The density distributions for different values of γ are shown

in Fig. 31. For the values $\gamma < 1$ the density distribution is uniform (constant) to some boundary and then falls off to zero over Debye distance $\Delta\xi \approx 1$. For the values $\gamma > 1$ the density distribution approaches a Gaussian, which is characteristic for ideal gases. Thus we define $\gamma = 1$ as the transition boundary between classical gas and the state where the plasma collective effects, namely the mean electric field of the ion cloud, start playing an important role. Since we know the relationship between γ and the temperature through the integral $Y_3(\infty)$ we can find the characteristic transition temperature corresponding to $\gamma = 1$. Since $Y_3(\infty)|_{\gamma=1} \approx 9.91$, then at this point $T|_{\gamma=1} = \frac{Ne^2}{9.91L\epsilon_0 k}$. For our trap $L = 50$mm, therefore $T|_{\gamma=1} \approx 4.2 \cdot 10^{-4} \times N$ (for $N = 10^3, 10^4, 10^5, 10^6$, the corresponding $T = 0.42, 4.2, 42, 420$K). The ion cloud temperature as a function of the parameter γ is plotted in Fig. 32. An interesting fact is that the condition $\gamma = 1$ (or $n_0 = \frac{1}{2}(n_0)_{max}$) is met at the same temperature independent of the potential depth. In fact this holds true for any value of γ, i.e. the density distribution of the ion cloud is described by the same function independent of the trapping potential. The only difference between the density distributions at the same temperature but different potential depths is their radial size.

Also, since we know that the density in the center of the cloud changes with temperature as determined by Eq.(5.31), we can write the particle density in the center of the cloud as:

$$n_0(T) = \frac{\max(n_0)}{1 + \gamma(T)}. \tag{5.38}$$

The calculated result showing the dependence of n_0 on the temperature is shown in Fig. 33.

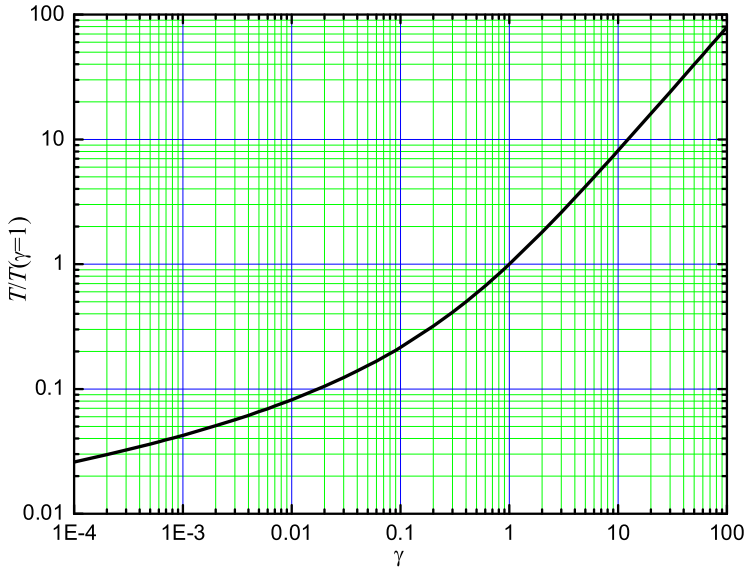

Fig. 32. The temperature dependence on the parameter γ relative to T($\gamma = 1$).

2. Collision heating

An important property of the trapped plasma is that it is constantly heated up through the applied rf field. The rf field induces the micromotion of the ions. The kinetic energy is transferred from the micromotion into the thermal macromotion through collisions. The Coulomb collision frequency is:

$$\gamma = n\sigma_C v, \tag{5.39}$$

where γ is the collision rate, n is the particle density, σ_C is the crossection of the Coulomb collisions, and v is the velocity of the particle experiencing the collision. For our purpose the velocity of the particle is the average, i.e. the thermal macromotion velocity $v = \sqrt{kT/m}$. The Coulomb collision crossection is[42]:

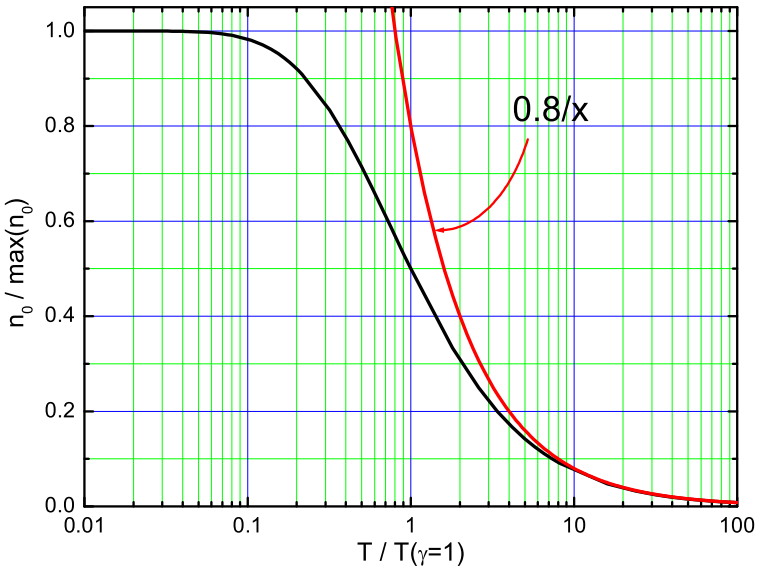

Fig. 33. The dependence of the density in the center of the ion cloud on the temperature. Temperature is measured in the units of temperature at $\gamma = 1$. At large temperatures the dependence of maximum density on temperature goes as T^{-1} in accordance with Gaussian character of the density distribution.

$$\sigma_C = \frac{e^4}{4\pi\epsilon_0^2 m^2 v^4} \log\left(1 + \Lambda^2\right), \tag{5.40}$$

where $\Lambda = 12\pi n\lambda_D^3$ is the plasma expansion parameter. It is important to note that logarithm in Eq.(5.40) is often written as $\log\Lambda$, and not $\log(1+\Lambda^2)$. That is because in most texts the plasma is considered at high temperatures, when the plasma expansion parameter $\Lambda \gg 1$. In that case $\log(1+\Lambda^2) \approx 2\log\Lambda$. The transfer of the kinetic energy of oscillations due to the rf trapping field (rf heating) occurs via collisions between the ions. The rate of energy transfer is roughly given by the expression

$$\frac{\Delta K}{\Delta t} = \gamma \langle \Delta\epsilon \rangle, \tag{5.41}$$

where $\langle \Delta\epsilon \rangle$ is the average energy transferred with each collision. Earlier[43, 44] this energy was approximated to be a fraction of the thermal energy $\langle \Delta\epsilon \rangle \propto kT$, which produced the following expression for the rf heating rate:

$$\frac{\Delta K}{\Delta t} = A \frac{kT}{2} \frac{e^4 n}{4\pi\epsilon_0^2 m^{1/2} (kT)^{3/2}} \log\left(1 + \Lambda^2\right), \tag{5.42}$$

where the coefficient A is estimated to be approximately $0.01 \times \frac{8}{15}$ from the simulation. This expression matches the general requirement for the rf heating imposed by the lineshape of the fluorescence of the trapped ions, i.e. that the rf heating has to decrease both at high and at low temperatures. At high temperatures the rf heating given by Eq.(5.42) behaves as:

$$\frac{\Delta K}{\Delta t} \propto T \frac{n}{T^{3/2}} = T^{-3/2}, \tag{5.43}$$

while at low temperatures it changes to

$$\frac{\Delta K}{\Delta t} \propto T \frac{n_0}{T^{3/2}} \left(n_0 \left[\frac{T}{n_0} \right]^{3/2} \right)^2 = T^{5/2}. \tag{5.44}$$

The graph of the rf heating versus the temperature of the stored ions is given in Fig. 34. The different heating curves correspond to different plasma parameter conditions. Since the plasma parameter Λ depends on both density and temperature, it can have different values at the same temperature.

The power law dependence of the rf heating at high temperatures would result in eventual heating of the ions out of the trap. In reality, this does not happen and the ions can often be stored in the trap for hours. The expression given by Eq.(5.42) does not apply to dilute ion clouds, or some cooling mechanism becomes relevant at high temperatures. One such cooling mechanism is the evaporative cooling. Since the ion trap has finite depth, the probability of an ion escaping the trap increases

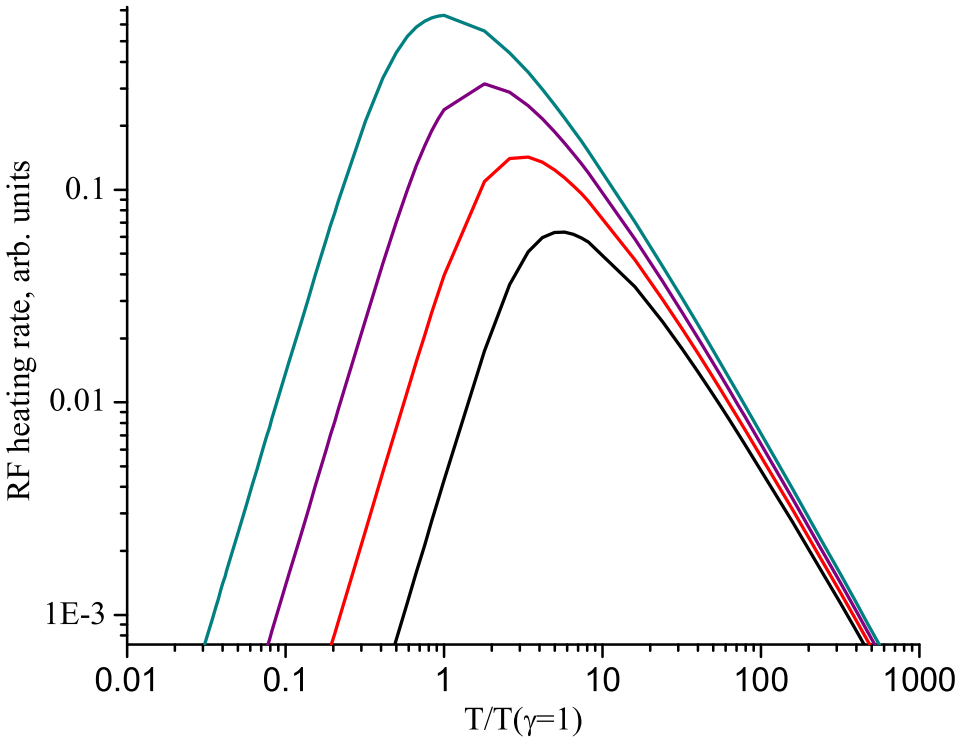

Fig. 34. The dependence of the RF heating on the ion temperature as given by Eq.(5.42).

with temperature. Since the ions escaping from the trap have higher kinetic energy (temperature) than the ions remaining in the trap, the effective temperature of the stored ions is lowered. Another energy dissipative processes that comes to mind is the energy dissipation through currents induced in the trap rods by the moving ions. The magnitude of these currents and thus the rate of energy loss should increase proportionally to the magnitude of the ion energy and thus this dissipation rate is proportional to T. This linear dependence would be able to overpower the decreasing rf heating at some temperature, and stabilize the temperature of the ions.

C. THERMAL EQUILIBRIUM

The kinetic energy (temperature) of the ion cloud is established by equilibrating the energy flows in and out of the cloud. One of the channels of the energy exchange is through the laser radiation as described in the section A. There are many other channels that are responsible for the energy exchange between the cloud and the environment: the collisions between the ions and the buffer gas, the collisions between the ions in the cloud that lead to thermalization of the rf vibrational motion (rf heating) etc. The equilibrium between all of these processes is eventually reached when the energy absorbed by the cloud is equal to the energy lost by the cloud. In this state the net energy flow is zero:

$$\frac{\Delta K}{\Delta t} = 0. \tag{5.45}$$

The two most important processes that occur in the trap are the laser cooling and the rf heating (heating due to the collisions with background gas in neglidgeble at UHV conditions). Both of these processes have been described in this chapter. The graphical solution to Eq.(5.45) is presented in Fig. 35. The rf heating is described by Eq.(5.42). The thick blue line shows the rf heating rate and the thin lines show the laser cooling rates at different detunings. The arrows indicate the intersection points between the rf heating curve and the laser cooling curve, i.e. the temperatures at which the heating and the cooling balance out. Figure 35(a) shows the case when the laser cooling is too weak to cause the ion cloud to crystallize. The temperature is decreased as the detuning decreases from 1GHz to 0.5GHz. However one can see that the equilibrium temperature at the detuning of 0.2GHz is higher than that at 0.5GHz and the temperature continues to increase as the detuning is further decreased. Thus the cooling due to laser radiation is not strong enough to overcome the maximum of

(a)

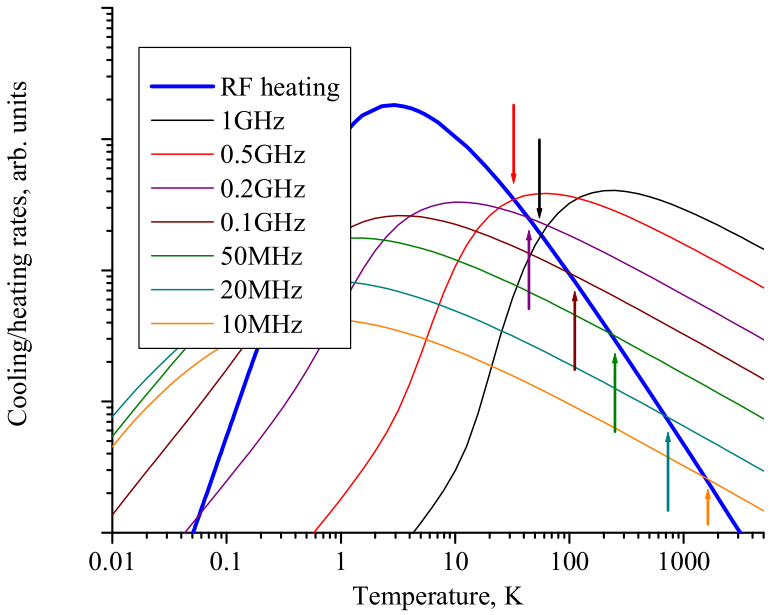

(b)

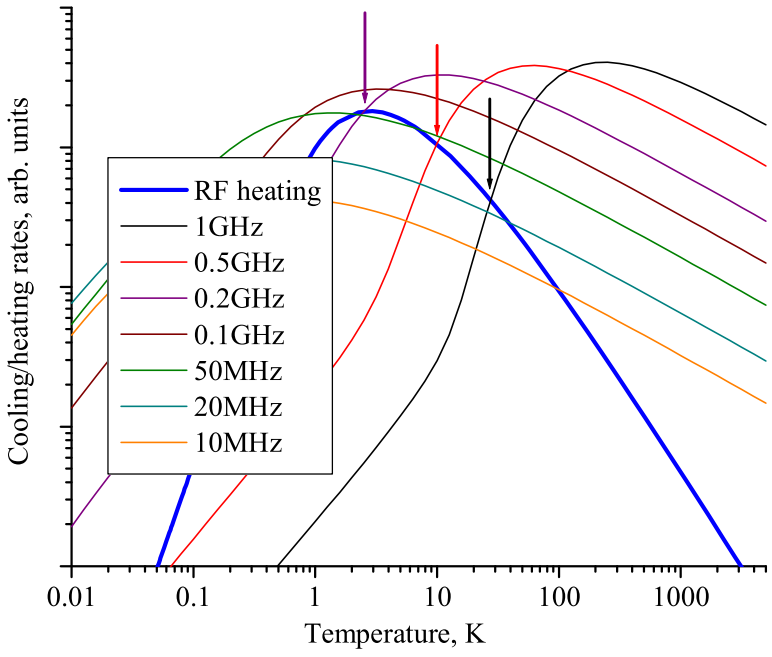

Fig. 35. Graphical illustration of the heat transfer balance.

the rf heating. Figure 35(b) shows what happens when the laser cooling strength is increased. In this case the temperature gradually decreases as one moves closer to the resonance. At the detuning of 0.2GHz the temperature is about 1K and the rf heating reaches its maximum. But at the next step in the laser detuning, 0.1GHz, there is not an intersection point since the laser cooling is higher than the rf heating at any temperature. That causes the temperature of the ion cloud to drop rapidly to the millikelvin range, where eventually laser cooling is balanced out by the recoil heating. Therefore the equations (5.45) and (5.42) qualitatively describe both situations that can occur in the experiment: a) the laser cooling is too weak and one observes a distorted Gaussian with the fluorescence starting to decrease before the transition frequency is reached; and b) the laser cooling is strong enough to crystallize the ions, and a fluorescence dip is observed as the temperature of the ion cloud drops rapidly from 1K to the milliKelvin range. The examples of the fluorescence signal as determined by the rf heating in Eq.(5.42) are shown in Fig. 36. The fluorescence curves corresponding to the relative strength of laser cooling of 1 and 5 do not exhibit the sudden drop in fluorescence. Increasing the strength of the laser cooling causes the temperature (and therefore the fluorescence signal) to drop at some detuning from the resonance frequency. The bigger the strength of the laser cooling, the earlier, further from the resonance the ion cloud temperature drops into the milliKelvin range. The dependence of the detuning at which the ion cloud experiences temperature drop on the strenght of the laser cooling is shown in Fig. 37.

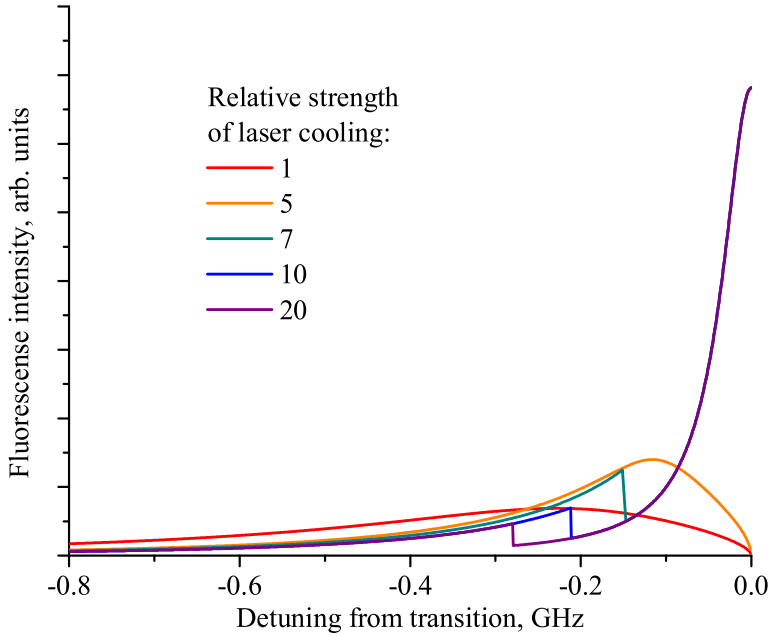

Fig. 36. Examples of the fluorescence signal from the laser cooled ions.

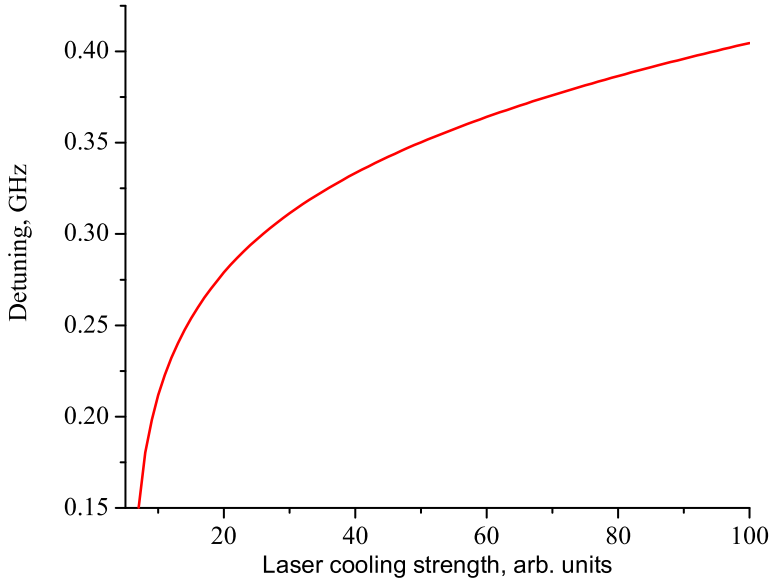

Fig. 37. Dependence of the detuning at which the ion cloud temperature experiences sharp drop on the strength of laser cooling.

CHAPTER VI

LASER COOLING AND SYMPATHETIC COOLING MEASUREMENTS

A. INTRODUCTION

Since the introduction[45, 46] of the idea of laser cooling[39], it has been applied in many areas of atomic physics. Almost immediately the laser cooling has been used for cooling the ions in the rf quadrupole traps[47, 48]. The theoretical basis for understanding of the laser cooling mechanisms has been developed quite rapidly[39, 49, 50, 51, 52], and subsequently more sophisticated cooling schemes[53, 54, 55] devised and implemented[56] with great success.

Laser cooling in the ion traps created a new set of interesting physical problems. The combination of the random thermal and regular oscillatory motion of the ions in an rf trap is quite complicated to describe analytically. The long range Coulomb interactions further complicate the picture. Therefore every step in understanding the processes involved in laser and sympathetic cooling is a challenge. Experimentally, application of laser cooling to the stored ions produced millikelvin temperatures in the rf traps. The ordered structures of the ultracold ions (ion crystals)[57, 58, 59], as well as a single stored ultracold ion[60], were observed. Most interestingly, two distinct modes in existence of the ion clouds were produced[58]: the ordered crystallized, and the un-ordered "chaotic" cloud states. Theoretically, many attempts have been made to describe the transition from the un-ordered to ordered state[61, 62, 63, 64, 65, 66, 67, 68]. This transition is exhibited by the sharp drop in the ion cloud temperature when the cooling rate exceeds certain threshold. This transition has hysteresis, i.e. when the cloud is in the ordered state and the cooling rate is gradually decreased,

the transition back into chaotic state occurs at a different (lower) cooling rate. The quantitative description of this phenomenon has yet to be achieved.

A more simplified approach, based on the principles of thermodynamics, is being developed[43, 69, 70, 71, 72, 44, 73] to describe the ion dynamics in the rf trap. While the chaos theory is probably quite appropriate for the few-ion clouds and crystals, the increase in size of the ion cloud should make the statistical models more relevant. And indeed, very large ion clouds and crystals have been studied recently[74, 12, 75].

The interest in the details of ion dynamics and the large ion clouds is due in large part to the sympathetic cooling[12, 76, 77]. Sympathetic cooling happens when two different ion species are trapped together in the trap and one of them is laser cooled. In this situation the other ion specie will eventually also cool down through thermal collisions. This phenomenon has been demonstrated on atomic ions[77, 76] and small molecular ions[13]. However, the previous theoretical studies have suggested[70] that sympathetic cooling is the most efficient when it involves ion species of similar mass. Thus the experimental efforts in sympathetic cooling are mostly concentrated on the close-mass ion mixtures. However the more intriguing goal is to achieve sympathetic cooling of large molecules by small ions which is the scope of this dissertation.

B. LASER COOLING OF THE Mg^+ IONS

1. Procedures

Laser cooling curves were obtained in the following way. The dye laser was manually tuned to the neighborhood of the Mg^+ ion transition frequency. Then it was placed into the computer controlled mode when the laser frequency is determined by the voltage on one of the computer's DAC channels. The computer slowly scans the laser frequency over a 3.8GHz scan range. The full scan typically takes one minute which

corresponds to a scan speed of approximately 60MHz/s. The signal from hyperfine saturation spectroscopy of iodine is recorded simultaneously with the Mg^+ fluorescence signal. The positions of the iodine hyperfine absorption peaks are known very accurately (see Table I), and they provide the reference points for the determination of the laser frequency. The laser frequency at the intermediate points is determined by linear interpolation. Figure 38 shows a typical interpolation graph.

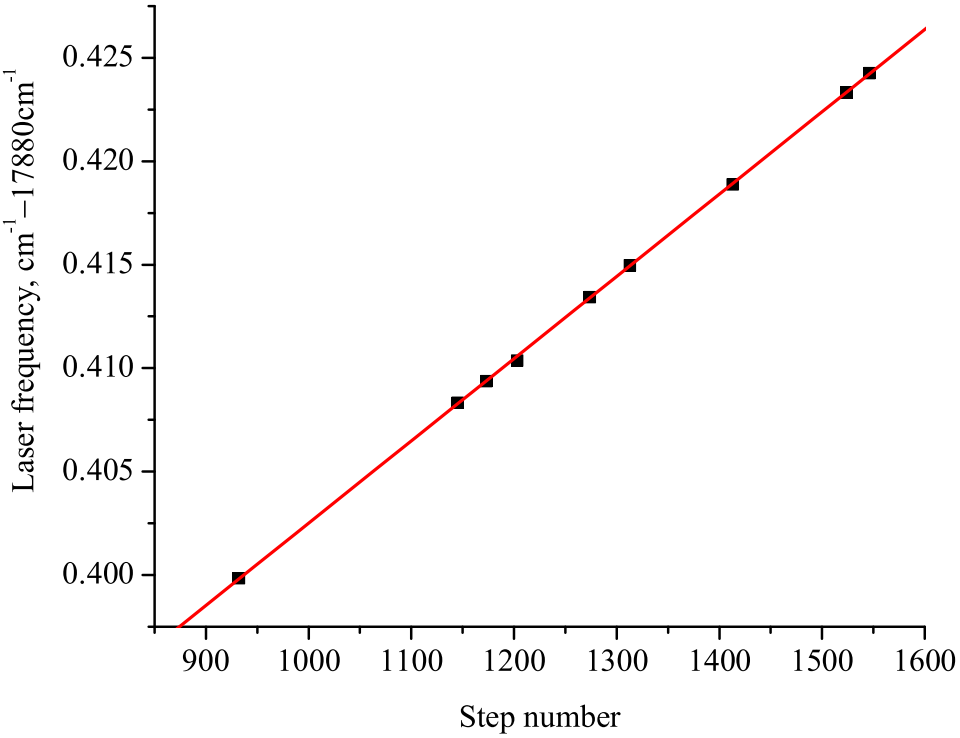

Fig. 38. Example of the interpolation graph used to determine the dye laser frequency during the scan. The dots correspond to the iodine hyperfine absorption line locations.

2. Influence of the rf heating

The influence of the rf heating on the fluorescence signal lineshape is shown in Fig. 39. From the graph one can follow the transformation of the fluorescence lineshape

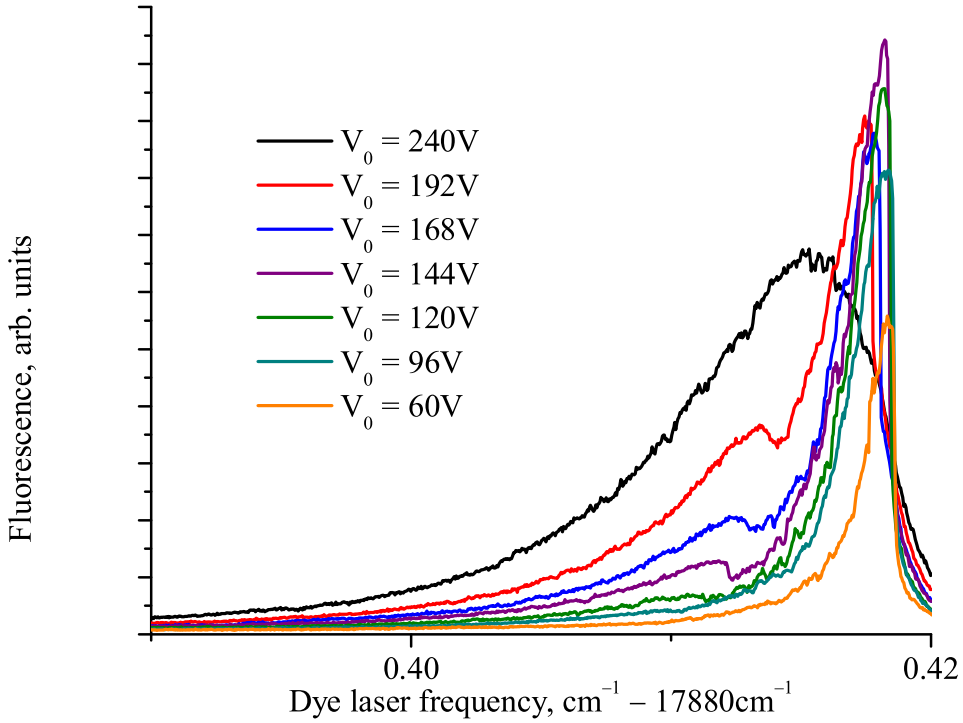

Fig. 39. The influence of the trapping voltage on the fluorescence lineshapes. The UV power is 400μW.

with the change in the trapping voltage amplitude V_0. As was shown in the MD simulations, the rf heating depends very strongly on the trapping voltage. At $V_0 = 240$V the laser cooling power is not enough to cause the dip in the fluorescence. However all of the fluorescence curves corresponding to lower trapping voltages do show the fluorescence drops. The width of the fluorescence line is also decreasing with the decreasing trapping voltage, which means that lower temperatures of the ion cloud are reached. Close to the transition frequency the fluorescence signal drops to al-

most zero, since the laser cooling power diminishes as the resonance frequency is approached. As soon as the cooling becomes insufficient to maintain the low temperature of the ion cloud, its temperature increases, in turn the heating rate from the rf field experienced by the cloud is increased. This snowballing effect creates the sharp drop in fluorescence, which drops even further as the laser cooling is replaced by laser heating when the laser frequency exceeds the transition frequency of the ion. From Fig. 39 one also observes that this drop happens at lower frequencies (further from the resonance frequency) as the amplitude of the rf trapping voltage increases. This is another fact that points to the higher heating rates for higher trapping voltages. One notices that even though while trapping voltages get smaller and the linewidths get narrower, the maximum fluorescence rate stops increasing somewhere between $V_0 = 144$V and $V_0 = 120$V. This effect points to the larger diameters of the ion cloud at lower trapping voltages, since the trapping potential is shallower. When the diameter of the ion cloud starts to exceed the diameter of the focused laser beam inside the trap, the maximum achieved fluorescence rate will be lower since the laser beam is overlapped with a smaller portion of the ion cloud, i.e. it shines on fewer ions. In addition to that, the ions were loaded using the exact same conditions ($V_0 = 120$V), and the trapping potential was adjusted to the desired value afterwards. The drop in the trapping voltage sometimes caused some ions (up to 20%) to escape from the trap, thus the number of ions stored in the trap was usually slightly smaller at the lower trapping voltages.

From the linewidths of the fluorescence curves shown in Fig. 39 one can estimate the lowest temperatures reached by the ion cloud due to the laser cooling. Using the expression (5.14) the temperatures corresponding to the different values of HWHM of the fluorescence line are calculated and plotted in Fig. 40. Only the temperatures below 1K are shown since at higher temperatures the lineshape is Gaussian and the

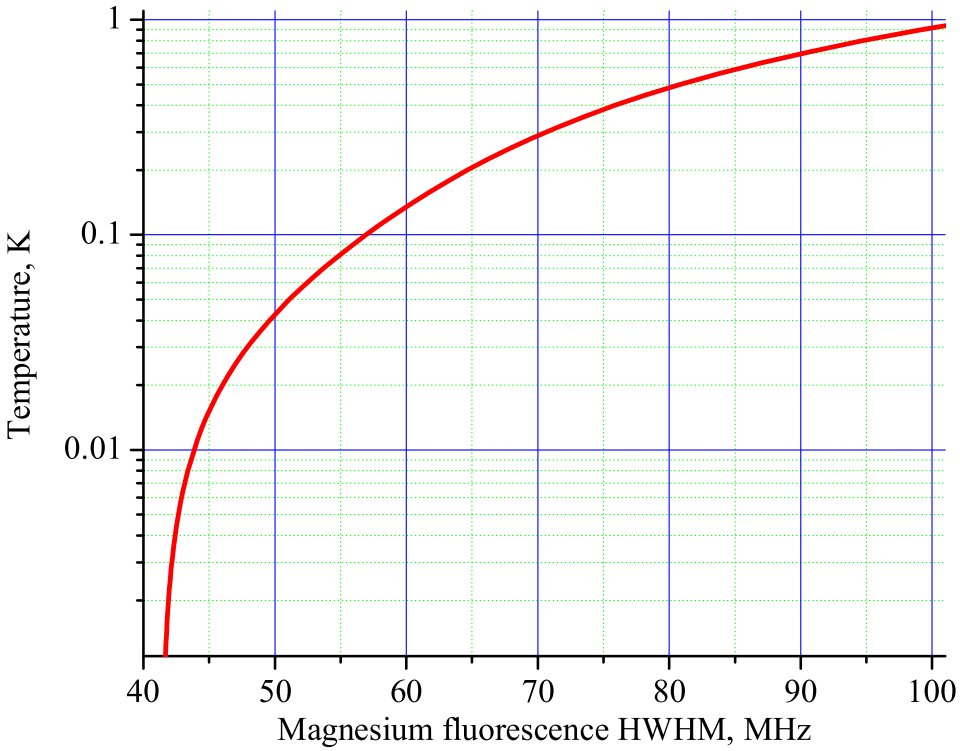

Fig. 40. HWHM of the Mg fluorescence line at low temperatures.

temperature dependence of the linewidth is expressed analytically (see Eq.(5.11)). The estimated temperature values are compiled in Table III.

Table III. Lowest temperatures achieved by laser cooling for different values of the trapping voltage V_0. UV power is 400μW.

Trapping voltage amplitude V_0, V	HWHM, MHz	Temperature, K
240	527	11.7
192	203	3.4
168	166	2.5
144	126	1.5
120	122	1.4
96	116	1.3
60	84	0.57

3. Effects of the cooling laser power

Higher laser cooling efficiency, and therefore lower temperatures, are expected when the laser power is increased. The increase in laser power is expected to increase the efficiency of laser cooling, and therefore lower temperatures. As shown by the simulations, at low temperatures (< 0.5K) the rf heating due to the quadrupole trapping field is negligible. Other heating mechanisms are expected to determine the lowest achievable temperature and the fluorescence lineshape. One such mechanism responsible for setting the low temperature limit is the recoil heating, which establishes the Doppler cooling limit on the laser cooling (see Chapter V). Of course the width of the fluorescence line is subject to the saturation broadening which would skew the

results, as it increases the linewidth as:

$$\Delta\omega = \gamma\sqrt{1 + \frac{I}{I_{sat}}}, \tag{6.1}$$

where $\Delta\omega$ is the broadened half-linewidth, γ is the natural half-linewidth, I is the laser intensity, and I_{sat} is the saturation intensity. In the case of $^{24}Mg^{+}$ transition that is being utilized here, the saturation intensity is $255 mW/cm^2$, and the size of the UV spot in the trap center is approximately $0.2 \times 0.6 mm$. That puts the saturation UV power at approximately $300\mu W$. The non-uniform intensity distribution across the UV beam spot and the positioning of the beam relative to the ion cloud are also sources of uncertainty in interpreting low temperature fluorescence lineshapes.

An example of how the fluorescence lineshapes change with laser intensity is illustrated in Fig. 41. As one can easily observe from the graph, the linewidth of

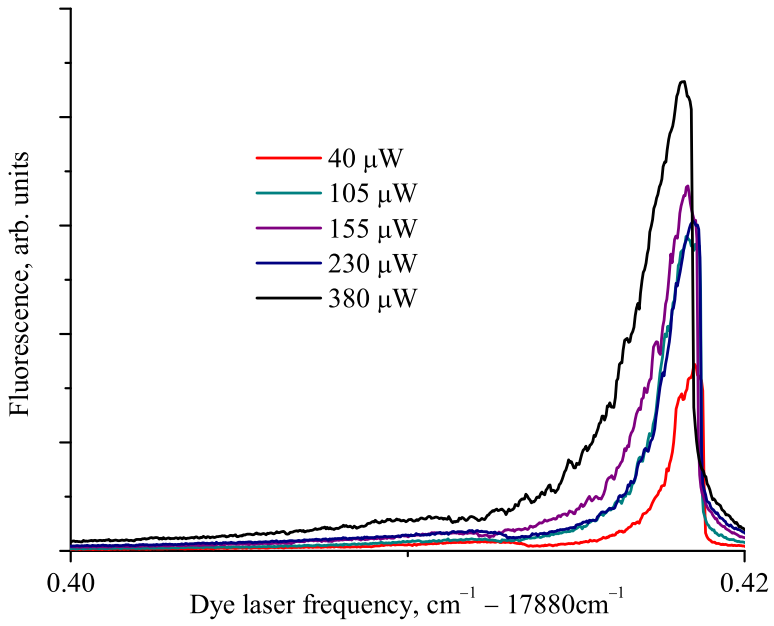

Fig. 41. Fluorescence lineshapes for different UV powers. The trapping voltage amplitude is $V_0 = 120V$.

the fluorescence line increases as the UV power is increased. The dependence of the fluorescence linewidth on the UV power for several trapping voltage amplitudes is plotted in Fig. 42. The linewidth of the fluorescence is indeed increasing, as

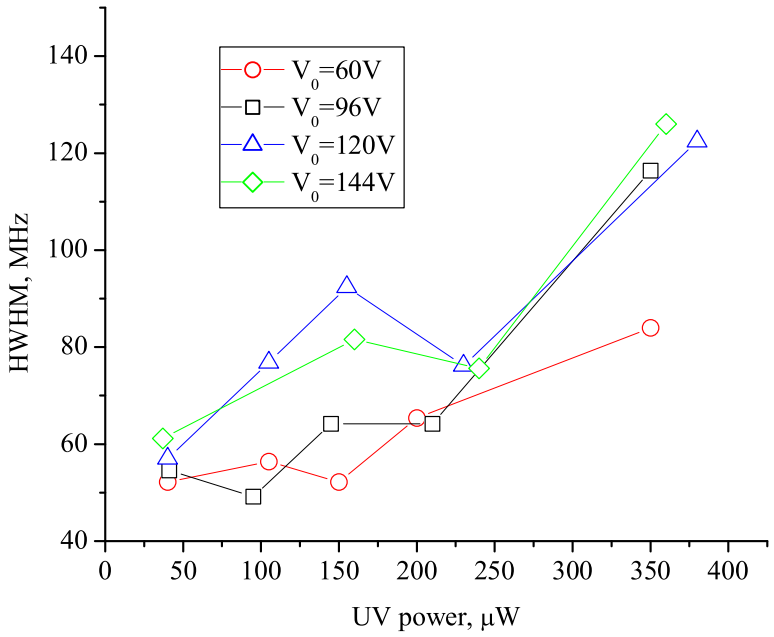

Fig. 42. Dependence of the fluorescence linewidth on UV power for different trapping voltage amplitudes.

it would in the case of saturation broadening, however there are some features on the graph that the saturation cannot explain. For example, it appears that the linewidth experiences a local minimum at some intermediate UV power, and this feature is repeated for every trapping voltage shown. If one is to take the square of the linewidth and attempt a linear fit according to Eq.(6.1), one obtains the value of the saturation intensity of about 100μW, but the linear fit is so poor that at best the associated error is comparable with the value. The linear fit fails for two out of four trapping voltages shown in Fig. 42, and produces the saturation intensity value of 300μW for the lowest trapping voltage in the graph $V_0 = 60$V. The picture is not

clear in this case in part due to the mode structure of the UV light emitted from the external doubling cavity. The mode is clearly non-Gaussian, and the intensity is not distributed uniformly within the laser beam. Another property can be seen from Fig. 42: the fluorescence linewidths are quite close to each other in value at small UV powers. The difference increases dramatically as the laser power is increased.

The fluorescence graphs contain more information available for analysis. Since the cooling rate is proportional to the laser detuning from the resonance $\Delta\omega = \omega_L - \omega_0$. The cooling rate is also proportional to the rate R at which the photons are scattered:

$$\frac{\Delta K}{\Delta t} = -\hbar\Delta\omega R. \tag{6.2}$$

The important fact is that the scattering rate is detected directly since it is the fluorescence rate. Some of the fluorescence graphs contain the "phase transition" dip in fluorescence which is present when the rate of laser cooling exceeds the heating rate and the temperature of the ion cloud drops dramatically. Since at the point right before the drop the heating rate is at its maximum, we can deduce its value from the directly measured cooling rate given by Eq.(6.2). The data extracted from the fluorescence graphs that show the necessary feature are compiled in Table IV. Expectedly the maximum heating rates increase along the rows of the table since that is the direction in which the trapping voltage increases. However, if the heating rates are independent of the laser power, they should stay constant for each of the columns in the table. In contrast to that the heating rates consistently increase with the laser power. The significance of the data compiled in Table IV is that this calculation method is independent of the saturation effects.

If there was a heating effect that would depend on both the laser power and the trapping voltage, it would explain the features of the power dependence shown in Fig.

Table IV. The maximum heating rates (in arbitrary units) for different laser powers.

$V_0 = 96$V		$V_0 = 120$V		$V_0 = 144$V		$V_0 = 192$V	
UV power	Max heating rate	UV power	Max heating rate	UV power	Max heating rate	UV power	Max heating rate
41μW	0.185	40μW	0.33	37μW	0.52	–	–
95μW	0.31	105μW	0.41	–	–	–	–
145μW	0.29	155μW	0.73	160μW	0.99	–	–
–	–	–	–	240μW	1.2	250μW	2.66
–	–	–	–	360μW	1.9	400μW	4.8

42. One such effect was discovered in MD simulations and is described in Chapter IV. It is associated with the random changes in the velocity directions. However, the magnitude of the heating mechanism in the reduced form that was studied is not sufficient to create such strong effect on the fluorescence linewidth. It could explain for instance why the drop in fluorescence near the transition frequency is moved further from the resonance when the laser power is increased (this effect can be seen in Fig. 41). It is possible that the random changes in the ion velocities due to the scattering of the photons are indeed responsible for the effect reported here if the timing of the photon absorption and re-emission is to be considered. This interesting question is in the plans for further investigations.

4. Laser cooling at high rf amplitudes

The measurements were also conducted at higher values of the rf trapping amplitude. At such high trapping voltages the laser cooling power was not sufficient to achieve the fluorescence dip characteristic to the sudden temperature drop of the ion cloud. The

fluorescence linewidths are quite large, so the saturation effects are not of importance. The fluorescence linewidth data for V_0 =288V and V_0 =384V are summarized in Table V. It follows from the data that increasing the UV power does not result in better

Table V. The fluorescence linewidths and temperatures at high trapping voltages.

	$V_0 = 288$V			$V_0 = 384$V		
UV power, μW	103	185	330	100	180	320
Fluorescence linewidth, MHz	511	602	526	607	708	660
Estimated temperature, K	21.7	26.6	22.5	26.7	32.3	29.7

cooling in this case. My MD simulations do not extend far into the temperatures as high as those shown in the table. It has been shown that rf heating at its maximum has a plateau that starts around 5K and continues into higher temperatures (see Fig. 25). The data collected in Table V suggests that the rf heating drops sharply on the other side of the plateau. That would explain why increasing the cooling power fails to produce appreciable drop in the achieved temperatures.

C. SYMPATHETIC COOLING OF THE FULLERENE IONS

Sympathetic cooling of the fullerene ions using the laser cooled Mg^+ ions is one of the goals of this research. Cooling the heavy molecular ions to ultra-low temperatures will create an opportunity to study spectroscopic molecular properties more precisely than before. Undoubtedly, a wealth of new phenomena and data will be obtained and studied. This research is the first step in this exciting direction.

To study the sympathetic cooling, Magnesium and fullerene ions were stored in the trap simultaneously. The two different outer segments of the trap were used to

subsequently load the Magnesium and the fullerene ions. To do so a large dc offset was applied to the center segment of the trap during loading, so that the center segment serves as the separating barrier between the Magnesium and fullerene segments. This is done so that the very hot fullerene ions do not expel the Magnesium ions from the trap during the loading phase. The number of ions to load is determined by the loading time[14]. After the ions are stored in the separate segments, the dc barrier is gradually lowered and then given a small negative voltage (typically -0.5V). Thus both ion species trickle into the center segment where they mix together. UV radiation is then applied to cool the Magnesium ions and the fluorescence signal is recorded to deduce the ion temperature.

The great difficulty of cooling fullerene and Magnesium ions together is that, as my MD simulations have shown, the rf heating that needs to be overcome is increasing with at least the fourth power of the trapping voltage. However, it would be impossible to hold the fullerene ions in the trap if the trapping voltage is too low. The problem is worsened significantly by the fact that Magnesium experiences large rf heating at high trapping voltages and can consequently heat the fullerene ions so that they escape the trap. As a result the lowest trapping voltage amplitude that is needed to store both Mg^+ and fullerene ions is *higher* than that is needed to confine only the fullerene ions. Therefore, the window of trapping voltages that is available for trapping both ion species simultaneously is greatly reduced. The lowest trapping voltage that I was able to use for the simultaneous storage of both ion species was $V_0 = 384$V. The only parameter that I could further adjust to reduce the temperature that can be achieved via the laser cooling was the number of Mg^+ ions. As my MD simulations have shown, the rf heating is decreasing *slightly* when the number of ions is reduced. Ultimately the lowest Mg^+ temperature obtained by the method of sympathetic cooling was 5K. The data from that experiment is shown in

Fig. 43. The width of the Magnesium fluorescence is 200MHz, which corresponds to a temperature of 5K. The laser power used to obtain the graph in Fig. 43 is 400μW. It is possible that the temperature achieved in the experiment is actually lower than 5K since the width of the peak could be affected by saturation. This type of temperature of course can be reached by other means, for example, a supersonic jet. However, such a low temperature for heavy molecular ions has been achieved in the rf ion trap through sympathetic cooling for the first time to the best of my knowledge. If a more suitable (heavier) cooling agent, for example, Calcium or Barium, is to be used, lower temperatures, possibly down to the milliKelvin range, could be reached.

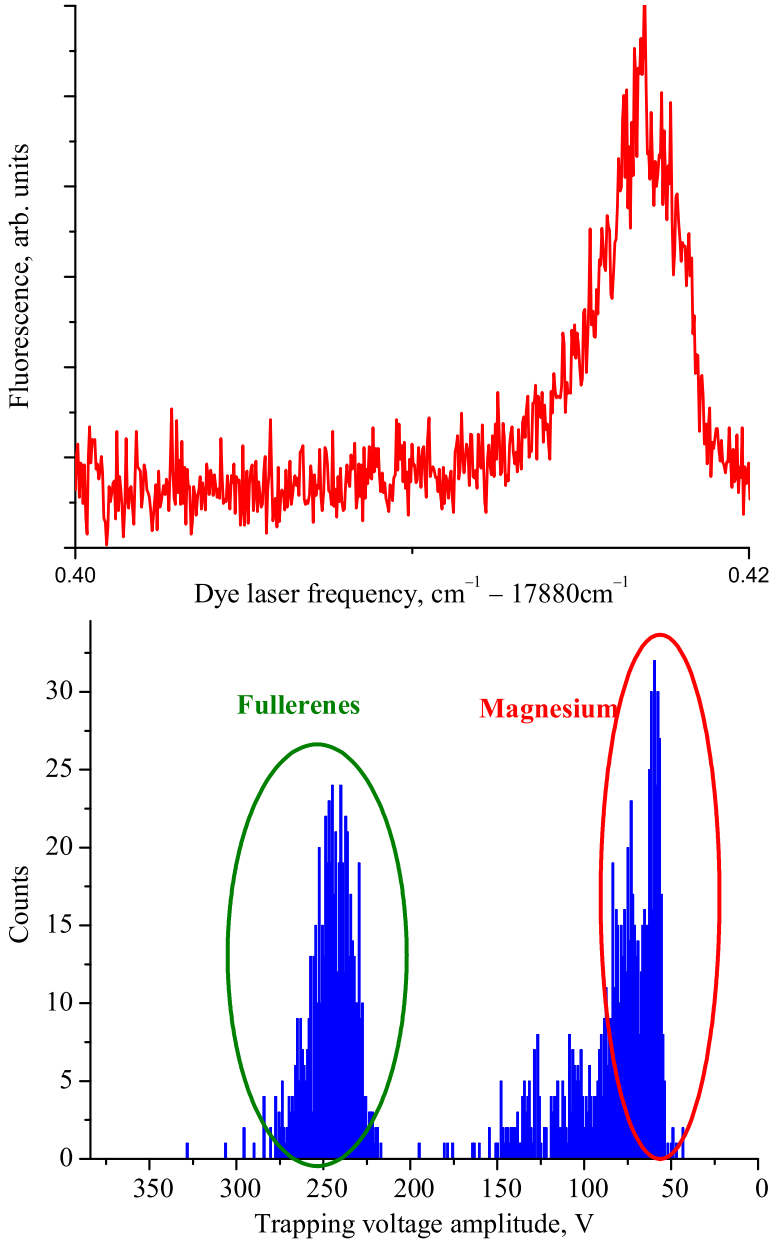

Fig. 43. The sympathetic cooling of Magnesium and fullerene ions. (a) fluorescence of the ^{24}Mg cooling transition; (b) the contents of the trap as collected by ion counting after laser cooling experiment.

CHAPTER VII

IMAGING OF THE TRAPPED IONS

One of the goals of the presented work is the direct observation of the ion clouds and the ion crystalline structures. An MCP camera has been used for that purpose and the image acquisition software has been written to record the images and even the time evolution of the ion cloud.

A. MCP CAMERA PRINCIPLES

A typical MCP camera is schematically shown in Fig. 44. An incoming photon

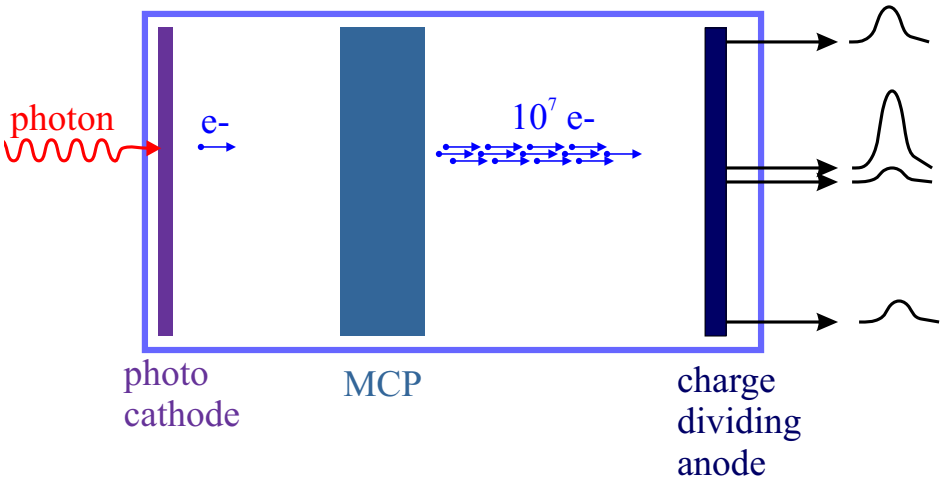

Fig. 44. Schematic diagram of the single photon imager.

hits the photocathode and has a chance to create an electron at the point of the impact. The electron is then guided towards the MCP amplifier array. The MCP amplifier array consists of an insulating plate with multiple channels. Covered with special material, the inside surface of each channel is likely to emit several secondary electrons when hit by an electron. As a result, a single electron at the entrance to an

MCP channel produces several thousand electrons at the exit of that channel (see Fig. 45). MCP amplifier is placed close to the photocathode so that the photon induced

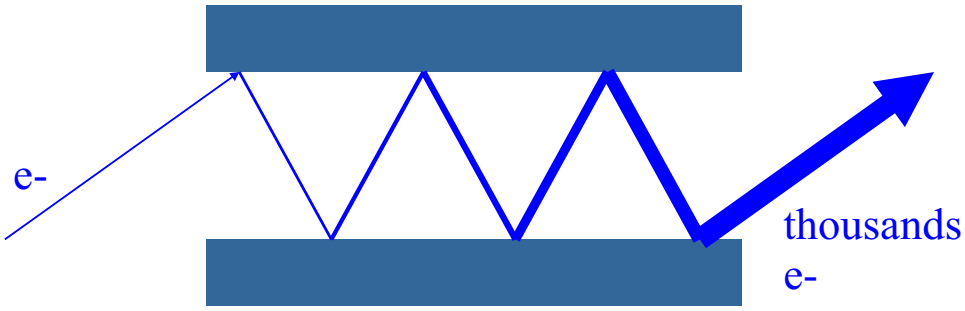

Fig. 45. Single channel of the MCP amplifier.

secondary electron enters the nearest MCP channel (proximity focusing). Sometimes several MCP stages are used is sequence to increase the amplification factor. Thus a burst of secondary electrons is created at the exit of the last MCP plate for each electron created at the photocathode. This burst is then acceletrated towards the charge dividing anode. As the group of ions hits the anode, it produces a wave of charge originating at the point of impact. At the edges of the anode there are 4 electrodes that collect the charge. The closer the point of impact is to the electrode, the larger portion of the charge that electrode will receive. Evaluating the charge collected from each of the electrodes tells the point of impact of the charge burst on the anode, and therefore tells the location on the photocathode where the photon initially hit. Keeping record and accumulating the information about all the photons registered this way reveals the illumination pattern, or the image projected onto the photocathode. Sometimes a secondary electron is generated on the photocathode not due to the incoming photon, but due to the thermal fluctuations. This thermal noise can bury a weak image. In order to reduce the thermal noise the MCP camera

is placed into a cooled housing. There also exists an important limitation on the incoming photon flux. Due to the high electron avalanche currents passing through the MCP channels and the tiny size of those channels an excessive input photon flux overloads the MCP channels and ultimately destroys the sensitive coating on the inner surface of the channel, rendering the channel useless. Therefore it is important to avoid imaging of bright point sources onto the photocathode.

B. THE DETAILS OF THE IMAGE ACQUISITION

The schematic representataion of the MCP imaging system is shown in Fig. 46. Each

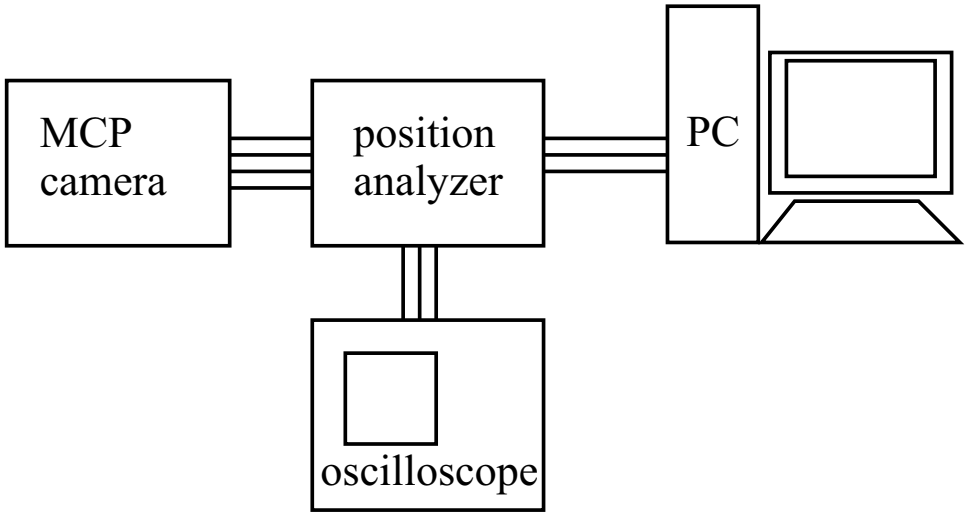

Fig. 46. Block diagram of the computer imaging system.

photon event is being processed by the charge integrating electronics of the position analyzer. The position analyzer generates pulse sequences on its outputs that match the position of the photon. The relevant portion of the pulse timing diagram is shown in Fig. 47. The X and Y channels output pulses which indicate the position of the photon by their amplitudes. The amplitude of the position pulse ranges from -0.5V

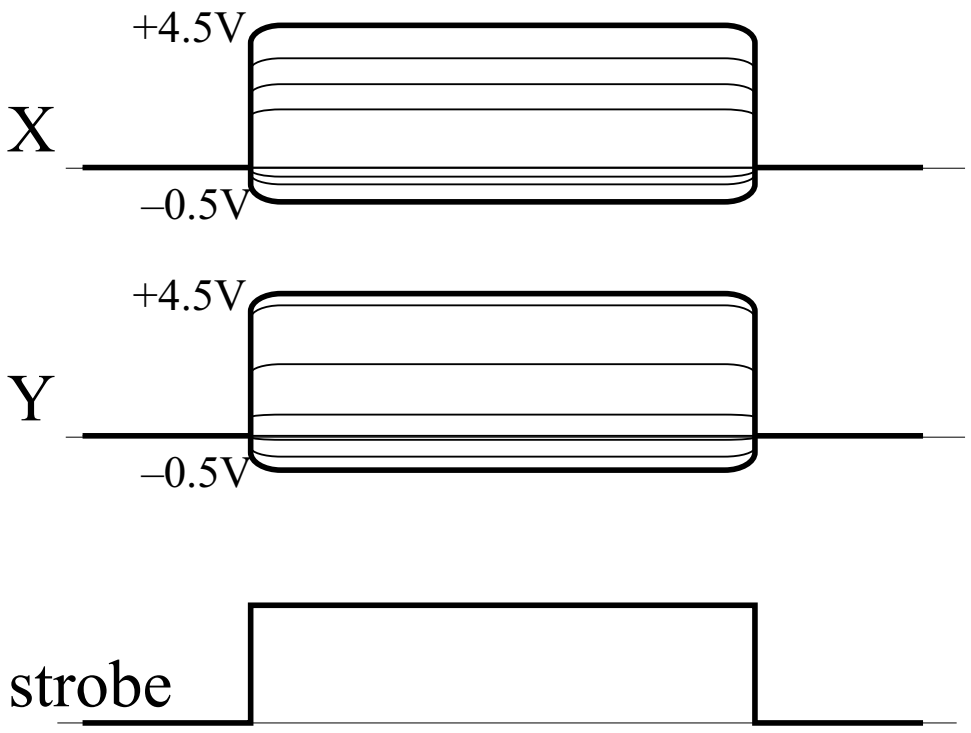

Fig. 47. Timing diagram of the three important signals used for image recording.

to +4.5V and it is linearly proportional to the position along the corresponding axis. The TTL strobe pulse is generated by the position analyzer to indicate the photon arrival event. It is used to trigger the ADC conversion by the data acquisition (DAQ) card in the computer. The strobe pulse is also sent to one of the counter channels of the DAQ card. This channel is operated in the timer mode, i.e. it registers the time at which the strobe signal occurred (the time the photon has arrived). The image acquisition program records the X and Y positions as well as the arrival time of each photon. It displays the image that is accumulated due to all the photons processed up to that point, and writes the information about each registered photon into a file. Therefore the log file contains all accesible information about the incoming photon stream and can be reanalyzed using different statistical approaches at a later time.

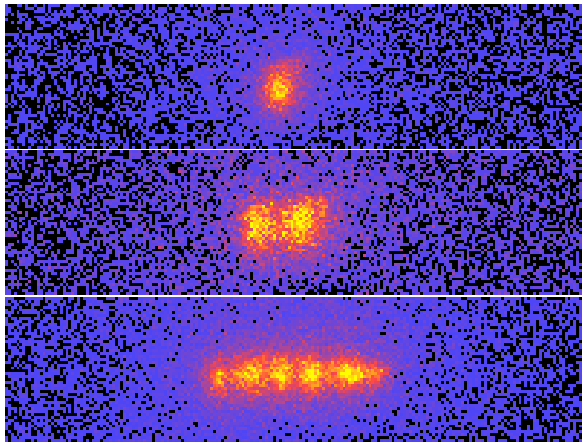

Fig. 48. $^{26}Mg^{+}$ ion crystals. The ion separation is about 100μm.

C. ION IMAGING

The imaging of the ion cloud onto the photocathode of the camera is done with a 35mm UV achromat lens. The imaging lens is placed as close to the trap as the vacuum setup allows, which places the image of the ions approximately 37cm away from the trap center and gives us the magnification factor of 8.5. The laser system was locked to one of the iodine lines so that the laser frequency is 100MHz away from the transition.

Figure 48 shows a few ion crystal pictures of $^{26}Mg^{+}$ ions. In this case, only a small number of ions were loaded into the trap. The ions in the picture appear large because the camera was slightly out of focus. The procedure for taking this picture involved using the side oven[14] for loading the ions, and in that case it was not uncommon that more than half of ions accumulated in the trap were not Mg^{+} ions. Taking into account the natural abundance of the ^{26}Mg isotope, it follows that the cooled ions are only a few percent of the trap contents. So it is quite remarkable that $^{26}Mg^{+}$ ions could be cooled down into small ion crystals. The other Magnesium

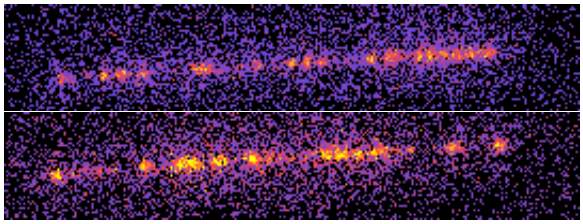

Fig. 49. Larger ion crystals. The separation between the ions is 50μm.

isotopes are not cooled and do not show at this laser frequency.

Larger crystals were also observed. Figure 49 shows a few pictures taken of the ^{24}Mg isotope ion crystals. Still there are quite a few background ions present in the trap. Some of the non-fluorescent ions occupy a slot in the string of the ions and appear as a gap in the string on the picture. One can see that the ions are more "packed" due to the larger number of ions in the trap and it is harder to resolve them. Another factor that affects the ion imaging is that the ion crystals are not always stable on the long time scale. The individual ions "jump" from one place to another in the crystal. That becomes quite noticeable when there are non-fluorescent ions emedded in the crystal. When observed in real time such crystals resemble a string of flickering lights.

Figure 50 shows the ion crystals observed when the trapping potential was relatively high ($V_0 = 360$V). The importance of this observation is that it proves that it is quite possible to cool the Magnesium ions to the mK temperatures necessary for crystallization at the trapping voltages required for successful trapping of the fullerene ions. Therefore it should be possible to cool a small number of fullerene ions to temperatures lower than 8K without having to employ cooled ions heavier than Magnesium.

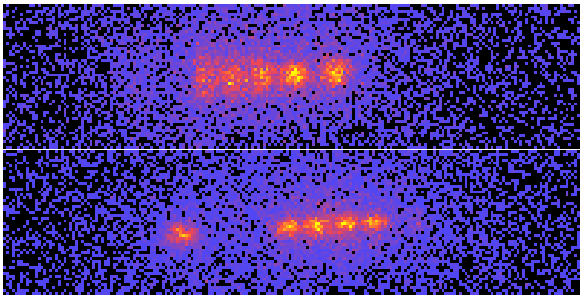

Fig. 50. Ion crystals at high trapping voltage amplitude.

D. DISCUSSION

The advantages and disadvantages of the single photon imaging system, such as the one developed and used in this reasearch, are better understood when compared to the alternative, a cooled CCD camera system.

Advantages:

1. The MCP imager produces images in *real time* with the ability to observe the impact of the photons incident onto the photocathode on the screen of the oscilloscope. This feature is extremely useful when adjusting the optical system, since one can immediately observe the response of the image to the changes in optical alignment or any other parameters. The CCD cameras do not allow for such immediate image observation, since it takes a while to read the image from the CCD. This difference is not crucial to the ultimate image quality, yet it greatly reduces the time necessary to achieve good optical alignment.

2. This feature is related to the previous item, yet it is important in itself. In the MCP imaging system full information is retained about *each registered photon*. This not only includes the coordinates of the photons, but also the arrival time with possible accuracy of 100ps. In addition to the arrival time, recording of

any other parameter can be triggered by the photon arrival event. For example, one of the interesting applications of the developed imaging system would be to produce the image of the ion crystal correlated to the phase of the trapping voltage, and in this way to possibly image the ion micromotion.

3. MCP imaging system has a noise level of 10^{-5} per pixel per second. The CCD imaging systems, while can be comparable to the MCP camera in terms of the thermal noise, also have a fixed readout noise and the fixed noise rate is 1 photon per pixel per readout at best. In order to achieve the net noise level comparable to the MCP camera, the CCD image accumulation time would have to be on the order of 100000s, i.e. more than a day.

Disadvantages:

1. The MCP imager can be easily damaged if not handled carefully. Like any PMT-type device its photocathode can be degraded by excessive light exposure. In addition when the high voltage is applied to the MCP amplifier, it is susceptible to the overload damage. Even very low light levels are capable of destroying the MCP channels. CCD cameras are quite rugged and are not damaged by ambient light levels.

2. The resolution of the MCP imager tube used in the experiments is 100μm. This is much worse than the existing CCD cameras, however recent technological advances resulted in production of the MCP cameras with 10μm resolution. Of course the image can be optically magnified to alleviate this drawback, but that requires quite large optical setups.

3. The photon rate that can be processed by the MCP camera electronics is quite low ($50,000$ photons per second maximum). Exceeding this rate will result in

the loss of photon information. This limitation has proven to be quite important in our case, since the photon rate from large ion crystals can be quite high (in excess of 10^6 photons per second). The CCD cameras do not have this limitation.

CHAPTER VIII

SUMMARY

An investigation of the sympathetic cooling method for the studies of ultra-cold molecular ions in a quadrupole rf ion trap has been conducted.

The target of the research presented in this thesis is to advance the understanding of the laser cooling and the sympathetic cooling in a quadrupole rf ion trap. One of the major factors in the laser cooling and ion dynamics in an rf trap is the rf heating, or the spontaneous increase in the ion energy due to the influence of the rf field. Molecular dynamics simulations are presented that study the rf heating mechanisms in the ion trap in the range of temperatures from few mK to 15K. The dependence of the rf heating rates on the ion temperature, trapping parameters, and the number of ions is obtained. A major result of the MD simulations is the dependence of the rf heating on temperature. The rf heating is shown to have a plateau that starts around 5K and extends beyond 15K. In this plateau region the rf heating remains approximately the same. At temperatures below 5K the rf heating rate falls off very sharply, and it becomes undetectable below 0.1K. A new rf heating mechanism affecting ultra-cold ion clouds exposed to laser radiation is described. The simulations have shown that the "infinite" ion cloud approach to studies of the large ion clouds is very useful in determining the rf heating rates and other phenomena. This method is very promising and should be applied in the future to study various aspects of rf heating and laser cooling, such as the rf heating rates at higher temperatures, more extensive studies on the dependence of the rf heating on the number of ions, and further studies into the new "velocity deflection" rf heating mechanism.

A saturation spectroscopy setup of the hyperfine spectra of the molecular iodine has been built to provide accurate frequency measurements of the laser wavelength.

Different versions of the setup are presented and their properties are discussed. The setup has potential to be used to not only measure the frequency of the dye laser, but also, with some upgrades of the optical and the electronic components, it is capable of controlling the laser frequency in a wide range with high precision.

This iodine reference is used to calibrate the frequency dependence of the fluorescence lineshapes of the laser cooled Mg^+ ions under different trapping conditions. The ion temperatures are deduced from the measurements. Despite the fact that saturation effect has affected the data, the fluorescence lineshapes corresponding to high temperature ion clouds indicate that the plateau in the rf heating, that was discovered in the MD simulations, drops off sharply at high temperatures. Thus the combination of MD simulations and the experimental results suggest that the dependence of the rf heating on the temperature has the form of a "high hat".

Cooling of the heavy ($m = 720$a.u.) fullerene ions to under 10K by the means of the laser cooled Mg^+ ions($m = 24$a.u.) is demonstrated. This sympathetic cooling method should be able to provide researchers with a large number of molecular ions at ultra-cold (sub-Kelvin) conditions. Further improvements in the sympathetic cooling method are suggested.

A single-photon imaging system has been developed. The imaging system has the unique capability of recording the data associated with individual photons. It is used to obtain the images of the Mg^+ ion crystal structures at mK temperatures.

REFERENCES

[1] E. Fischer, Z. Phys. **156**, 1 (1959).

[2] W. Paul, O. Osberghaus, and E. Fischer, *Forschungsberichte des Wirtschaft und Verkehrministeriums Nordrhein Westfalen* (Westdeutscher Verlag, Koln, Germany, 1958), No. 415.

[3] R. F. Wuerker, H. Shelton, and R. V. Langmuir, J. Appl. phys. **30**, 342 (1959).

[4] H. A. Schuessler, in *Progress in Atomic Spectroscopy*, edited by W. Hanle and H. Kleinpoppen (Plenum Publishing Company, New York, 1979), pp. 999–1029.

[5] G. Z. K. Horvath, R. C. Thompson, and P. L. Knight, Contemp. Phys. **38**, 25 (1997).

[6] D. A. Church, J. Appl. Phys. **40**, 3127 (1969).

[7] M. Welling, H. A. Schuessler, R. I. Thompson, and H. Walther, Int. J. Mass Spectrom. Ion Proc. **172**, 95 (1998).

[8] C. A. Schrama, E. Peik, W. W. Smith, and H. Walther, Opt. Commun. **101**, 32 (1993).

[9] E. Wigner, Phys. Rev. **46**, 1002 (1934).

[10] E. Wigner, Proc. Faraday Soc. **34**, 678 (1938).

[11] I. Waki, S. Kassner, G. Birkl, and H. Walther, Phys. Rev. Lett. **68**, 2007 (1992).

[12] L. Hornekaer, N. Kjargaard, A. Thommesen, and M. Drewsen, Phys. Rev. Lett. **86**, 1994 (2001).

[13] K. Molhave and M. Drewsen, Phys. Rev. A **62**, 011401 (2000).

[14] X. Zhao, Ph.D. dissertation, Texas A&M University, 2001.

[15] S. Gerstenkorn and P. Luc, *Atlas du Spectre d'Absorption de la Molecule d'Iode 14800–20000 cm^{-1}* (Editions du Centre National de la Recherche Scientifique, Paris, 1978).

[16] M. Levenson and A. Schawlow, Phys. Rev. A **6**, 10 (1972).

[17] S. Haroche and F. Hartmann, Phys. Rev. A **6**, 1280 (1972).

[18] J. H. Shirley, Phys. Rev. A **8**, 347 (1973).

[19] G. Bjorklund, Opt. Lett. **5**, 15 (1980).

[20] G. Bjorklund and M. Levenson, Phys. Rev. A **24**, 166 (1981).

[21] J. Hall, L. Hollberg, T. Baer, and H. Robinson, Appl. Phys. Lett. **39**, 680 (1981).

[22] H. Kato, M. Baba, S. Kasahara, K. Ishikawa, M. Misono, *et al.*, *Doppler-Free High Resolution Spectral Atlas of Iodine Molecule 15,000 to 19,000 cm^{-1}* (Japan Society for the Promotion of Science, Tokyo, Japan, 2000).

[23] M. Gottlieb, *Electro-optic and acousto-optic scanning and deflection* (Marcel Dekker, New York, 1983).

[24] M. P. Allen and D. J. Tildesley, *Computer Simulation of Liquids* (Oxford Science Publications, Oxford, 1987).

[25] J. M. Haile, *Molecular Dynamics Simulation* (John Wiley & Sons, New York, 1992).

[26] D. Frenkel and B. Smit, *Understanding Molecular Simulation* (Academic Press, San Diego, 1996).

[27] B. J. Alder and T. E. Wainwright, J. Chem. Phys. **27**, 1208 (1957).

[28] A. Rahman, Phys. Rev. **136**, A405 (1964).

[29] L. Verlet, Phys. Rev. **159**, 98 (1967).

[30] R. E. March, A. W. McMahon, F. A. Londry, R. L. Alfred, J. F. Todd, and F. Vedel, Int. J. Mass Spec. and Ion Proc. **95**, 119 (1989).

[31] A. V. Tolmachev, H. R. Udseth, and R. D. Smith, Int. J. Mass. Spectrom. **222**, 155 (2003).

[32] J. Prestage, A. Williams, L. Maleki, M. Djomehri, and E. Harabetian, Phys. Rev. Lett. **66**, 2964 (1991).

[33] D. H. E. Dubin and T. M. O'Neill, Phys. Rev. Lett. **60**, 511 (1988).

[34] J. P. Schiffer, M. Drewsen, J. S. Hangst, and L. Hornekaer, Proc. Nat. Acad. Sci. **97**, 10697 (2000).

[35] R. C. Davidson, *Physics of Nonneutral Plasmas* (Imperial College Press, London, 2001).

[36] C. Gear, *Numerical Initial Value Problems in Ordinary Differential Equations* (Prentice Hall, Inc., Englewood Cliffs, New Jersey, 1971).

[37] N. W. McLachlan, *Theory and Application of Mathieu Functions* (Dover Publication, INC., New York, 1964).

[38] F. M. Arscott, *Periodic Differential Equations; An Introduction to Mathieu, Lame and Allied Functions* (Macmillan, New York, 1964).

[39] D. J. Wineland and W. M. Itano, Phys. Rev. A **20**, 1521 (1979).

[40] D. H. E. Dubin and T. M. O'Neil, Rev. Mod. Phys. **71**, 87 (1999).

[41] T. M. O'Neil and C. F. Driscoll, Phys. Fluids **22**, 166 (1979).

[42] S. R. Seshadri, *Fundamentals of Plasma Physics* (Elsevier, Amsterdam, 1973).

[43] Y. Moriwaki, M. Tachikawa, Y. Maeno, and T. Shimizu, Jpn. J. Appl. Phys. **31**, L1640 (1992).

[44] T. Baba and I. Waki, J. Appl. Phys. **92**, 4109 (2002).

[45] T. W. Hansch and A. L. Schawlow, Opt. Commun. **13**, 68 (1975).

[46] D. J. Wineland and H. G. Dehmelt, Bull. Am. Phys. Soc. **20**, 637 (1975).

[47] D. J. Wineland, R. E. Drullinger, and F. L. Walls, Phys. Rev. Lett. **40**, 1639 (1978).

[48] W. Neuhauser, M. Hohenstatt, P. Toschek, and H. Dehmelt, Phys. Rev. Lett. **41**, 233 (1978).

[49] A. Ashkin, Science **210**, 1081 (1980).

[50] V. S. Letokhov and V. G. Minogin, Phys. Rep. **73**, 1 (1981).

[51] S. Stenholm, Rev. Mod. Phys. **58**, 699 (1986).

[52] C. S. Adams and E. Riis, Prog. Quantum Electron. **21**, 1 (1997).

[53] W. D. Phillips, Rev. Mod. Phys. **70**, 721 (1998).

[54] S. Chu, Rev. Mod. Phys. **70**, 685 (1998).

[55] C. N. Cohen-Tannoudji, Rev. Mod. Phys. **70**, 707 (1998).

[56] P. Lett, R. Watts, C. Westbrook, W. Phillips, P. Gould, and H. Metcalf, Phys. Rev. Lett. **61**, 169 (1988).

[57] D. J. Wineland, J. Bergquist, W. M. Itano, J. Bollinger, and C. Manney, Phys. Rev. Lett. **59**, 2935 (1987).

[58] F. Diedrich, E. Peik, J. M. Chen, W. Quint, and H. Walther, Phys. Rev. Lett. **59**, 2931 (1987).

[59] M. G. Raizen, J. M. Gilligan, J. C. Berquist, W. M. Itano, and D. J. Wineland, Phys. Rev. A **45**, 6493 (1992).

[60] W. Neuhauser, M. Hohenstatt, P. Toschek, and H. Dehmelt, Phys. Rev. A **22**, 1137 (1980).

[61] J. Hoffnagle, R. DeVoe, L. Reyna, and R. Brewer, Phys. Rev. Lett. **61**, 255 (1988).

[62] R. DeVoe, J. Hoffnagle, and R. Brewer, Phys. Rev. A **39**, 4362 (1989).

[63] R. Blumel, C. Kappler, W. Quint, and H. Walther, Phys. Rev. A **40**, 808 (1989).

[64] R. Brewer, J. Hoffnagle, and R. DeVoe, Phys. Rev. Lett. **65**, 2619 (1990).

[65] M. Moore and R. Blumel, Phys. Rev. A **50**, R4453 (1994).

[66] A. W. Vogt, Phys. Rev. A **49**, R657 (1994).

[67] J. Hoffnagle and R. Brewer, Phys. Rev. A **50**, 4157 (1994).

[68] R. Blumel, Phys. Rev. A **51**, 620 (1995).

[69] Y. Maeno, M. Tachikawa, Y. Moriwaki, and T. Shimizu, Jpn. J. Appl. Phys. **34**, L174 (1995).

[70] Y. Oshima, Y. Moriwaki, and T. Shimizu, Prog.Crystal Growth and Charact. **33**, 405 (1996).

[71] T. Hasegawa, D. Tanooka, and T. Shimizu, Phys. Rev. A **58**, 2327 (1998).

[72] J. Hou, Y. Wang, and D. Yang, J. Appl. Phys. **88**, 4334 (2000).

[73] T. Baba and I. Waki, Appl. Phys. B **74**, 375 (2002).

[74] M. Drewsen, C. Brodersen, L. Hornekaer, J. Hangst, and J. Schiffer, Phys. Rev. Lett **81**, 2878 (1998).

[75] L. Hornekaer and M. Drewsen, Phys. Rev. A **66**, 013412 (2002).

[76] T. Hasegawa and T. Shimizu, Phys. Rev. A **66**, 063404 (2002).

[77] B. Blinov, L. Deslauriers, P. Lee, M. Madsen, R. Miller, and C. Monroe, Phys. Rev. A **65**, 040304 (2002).

VITA

Vladimir Leonidovich Ryjkov was born in Moscow, Russia. He received the degree of Physicist with Honors (Red Diploma) from the Physics Department of Moscow State Univerisity, Moscow, Russia. He was admitted to the graduate school of Texas A&M University in 1996, and received his Ph.D. in Physics in 2003. For his address and other current information please contact Dr. Hans A. Schuessler, Department of Physics, Texas A&M University, College Station, TX 77843-4242.

The typist for this thesis was Vladimir L. Ryjkov.